Laser cooling and trapping of Ca^+ ions in a Penning trap

Jenn Liam Kingston Koo

A thesis submitted for the degree of Doctor of Philosophy
Imperial College London
September 8, 2003

Abstract

This thesis describes the efforts undertaken to achieve the goal of trapping and Doppler cooling *single* Ca^+ ions in the Penning trap. This will be used particularly for studying decoherence effects in the Penning trap which represents the long term goal of the Ion Trapping group at Imperial College London.

Trapping and Doppler cooling of Ca^+ ions in the Paul, combined and Penning traps are demonstrated. The operation in the Paul trap was significant as it allowed the laser wavelengths and detection system to be calibrated and the trap to be characterised before operation in the Penning trap was attempted. The operation in the combined trap was used to set the laser wavelengths to their correct values for use in the Penning trap. Doppler cooling of Ca^+ ions in the Penning trap required the use of 2×397nm lasers, 2×866nm lasers with their input currents frequency modulated to produce sidebands and 1×854nm laser.

The trapping of small numbers of Ca^+ ions in the Penning trap is demonstrated. Analysis of the fluorescence trace of ions undergoing quantum jumps allows us to infer that the number of ions present is probably two. Although single Ca^+ ions were not successfully trapped in the Penning trap, the results show that there is no fundamental problem with the laser cooling scheme used. Improvements to the current setup are suggested with the aim of trapping single Ca^+ ions in the Penning trap.

This thesis is dedicated to my parents.

Acknowledgments

First of all, I would like to thank my supervisors Danny Segal and Richard Thompson for their kind support and guidance throughout the course of my PhD. I would also like to thank everyone within the Ion Trapping group. Special thanks goes to Jake Sudbery, Eoin Phillips, Sebastian De Echaniz, Richard Hendricks and Arno de Lange not only for their help but also for providing the laughs especially during the more stressful days at work.

Special thanks to Ing Ing for her unwavering support, kind words of encouragement and for always being ready to lend a listening ear. I am also particularly grateful to Jason, Colin, Yan, Valen and Alex for their friendship and support.

Last but not least, I am greatly indebted to my parents for their constant support and encouragement. Without their support, this PhD would not have been possible.

Contents

List of Figures

List of Tables

Chapter 1

Introduction

The origins of the ion trap can be traced back to the early 1950's with the invention of the two dimensional quadrupole mass filter by Wolfgang Paul [58]. The use of such a device is to select and identify particles by their mass to charge ratio. A three dimensional version of this device was made available not too long after and is known today as an ion trap mass spectrometer. This tool is of great importance in the field of chemistry and biochemistry where it is used to ascertain the composition of complex molecules. The ion trap mass spectrometer is now widely available as a simple-to-use commercial analytical tool.

The advent of laser cooling has allowed the ion trap to be used as a high precision spectroscopic tool. Laser cooling reduces the kinetic energy of the trapped ions to the extent that first order Doppler shifts become zero and second order Doppler shifts are reduced to minimal values. This removes, to a large extent, one of the major sources of uncertainties when making high precision spectroscopic measurements.

Laser cooled trapped ions are also promising candidates as a basis for accurate frequency standards. The current frequency standard is set by the caesium fountain clock which uses a microwave transition as the clock transition. In contrast, trapped ions offer the possibility of using optical transitions as the clock transition, allowing for higher accuracies. Also, in an ion trap, the ions can be stored for very long periods of time in a nearly perturbation free environment. This allows for long interrogation times which is essential if the uncertainty in the measurement is to be made small [10]. Furthermore, the application of laser cooling eliminates the unwanted Doppler shifts thereby improving the accuracy of the absolute frequency measurement. Early evidence has shown the trapped ion clock to be just as stable and accurate as the caesium clock. Currently, the best accuracy achievable on an atomic clock is 1 part in 10^{15}. It is anticipated

that the trapped ion clock will achieve an accuracy of 1 part in 10^{18}.

Another important application of the ion trap can be found in the area of quantum physics. Again, it is the ability to isolate the ions in an unperturbed environment that makes this system an ideal one for investigating quantum phenomena. Examples of this include the experimental demonstration of the violation of Bell's inequality [63], a test of the linearity of quantum mechanics [13] and an investigation of the quantum Zeno effect [42].

A more recent but rapidly expanding field of study in which the ion trap has a prominent role to play is the field of quantum computing. Quantum computing offers the possibility of performing computations many times faster than its classical counterpart. It does so by taking advantage of superposition states that exist only in the quantum domain. The ion trap offers great promise for implementing quantum computing due to several reasons which will be described in more detail in Chapter 3 of this thesis.

The work presented in this thesis is part of a long term research project undertaken by the Ion Trapping group at Imperial College London (ICL). The main goal of this project is to investigate the practicality of the Penning trap as a means to implement quantum information processing (QIP). Currently, most of the research involving ion trap QIP has employed Paul traps. The Paul trap uses a high amplitude radio frequency field to confine the ions. In this field, the ion motion consists of a harmonic motion called the secular motion and a low amplitude, high frequency motion called the micromotion. Using laser cooling techniques the secular motion can be cooled to its zero point energy state. However, it is not possible to entirely eliminate the micromotion which represents a possible source of heating. Heating of the ion limits the fidelity of QIP operations. This is likely to be a source of decoherence. The Penning trap has the advantage that only static fields are used to confine the ions. It is possible therefore, that the heating rates and hence decoherence rates are lower in the Penning trap. The long term research goal of the group at ICL is then to quantify these decoherence rates in a Penning trap system. The first step in realising such a measurement is to be able to routinely trap single Ca^+ ions in the Penning trap. The next step will be to implement sideband cooling to the axial motion. Once cooling to the ground vibrational state is achieved, Rabi oscillations can be induced between the $4^2S_{1/2} \rightarrow 3^2D_{5/2}$ transition and a measurement on the coherence time obtained.

1.1 Thesis Description

Following this introduction, the next two chapters, Chapters 2 and 3 are introductory material which seek to familiarise the reader in the areas that are

relevant to this thesis. The first of these chapters describes the various types of ion trap available and the laser cooling schemes used especially in the context of QIP with trapped ions. The second of these chapters provides an introduction to the subject of quantum computing. It also describes two of the most promising physical schemes available to implement QIP. The first of these involves using techniques from the field of nuclear magnetic resonance and the second uses trapped ions. Greater emphasis is placed on the latter as it bears more relevance to the work done by our group at ICL. As was mentioned earlier, the long term goal of our group is to investigate the feasibility of the Penning trap as a means to implement QIP. Therefore, it is necessary that the current state of play of experiments involving trapped ions for use in QIP be described so that the motivation behind our work can be better understood.

The remainder of the thesis describes the efforts undertaken to trap and cool single Ca^+ ions in a Penning trap. This work was done in three stages with a different trapping mode used for each stage. The Paul trap, combined trap and Penning trap were used in stages one, two and three respectively. Work in the Paul trap and combined trap was jointly done with another PhD. student J. Sudbery. Although the long term experimental goals of this group only involves the operation of the Penning trap, the Paul trap was used as a means to test and characterise the apparatus required to Doppler cool Ca^+ ions before operating in the more demanding Penning trap environment. The combined trap was used as a means to set the laser wavelengths to the correct values for Doppler cooling in the Penning trap. Ideally, the laser wavelengths would be set using a high precision wavemeter, but unfortunately this was not available.

Each of these three trapping modes was achieved using the same ion trap setup, the difference being entirely in the fields applied to the trap. Most of the other apparatus used to operate in the different trapping modes were also the same. Chapter 4 contains a description of the experimental apparatus that is common to each of the three different trapping modes. Following that, Chapters 5, 6 and 7 describe the additional apparatus required for operation in the Paul, combined and Penning traps respectively. These chapters also contain results which show that Doppler cooling has been achieved in each of the trapping modes. The Paul and Penning trap chapters have additional results which show trapping of small numbers of ions. Suggested improvements to the current setup and a brief description of future work are included in the final section of Chapter 7. Finally, Chapter 8 draws conclusions for the thesis as a whole.

Chapter 2

Ion Traps and Laser Cooling

This chapter is divided into two main sections. The first section describes the principle of operation of various types of traps. It also highlights the unique characteristics of each of the trapping modes. The second section details the different laser cooling schemes in use with trapped ions. The laser cooling schemes described are especially useful in experiments involving quantum information processing.

2.1 Ion Traps

An ion trap is a device that is used to confine the ion to a very small region of space. The confinement is provided by the application of suitable electric and magnetic fields. There are two main types of traps, namely the Penning and the Paul or radiofrequency (r.f.) trap. Confinement in the Penning trap is provided by a static magnetic field and a static electric field. The Paul trap does not use a magnetic field but instead uses a high amplitude radiofrequency electric field to provide the trapping potential. Trapping can also be achieved by using both a static magnetic field and a radiofrequency electric field along with a static electric field. This is known as a combined trap. The operation of all three trapping modes will be described in more detail in the following sections. Variations of the Paul trap in the form of the linear Paul trap and miniature Paul trap are also described.

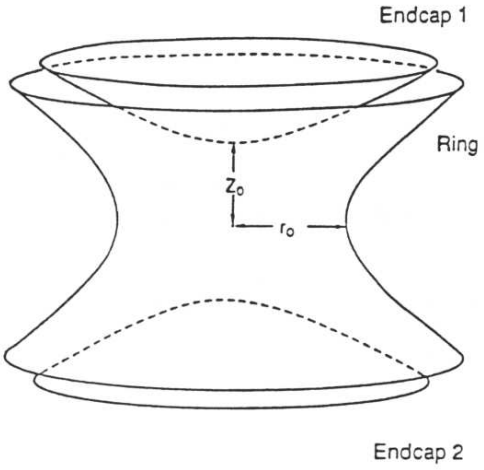

Figure 2.1: Electrode structure for the Penning trap.

2.1.1 The Penning Trap

The electrode configuration of the Penning trap is shown in Fig. 2.1. It consists of three electrodes: two endcaps and a ring electrode, shaped so that their surfaces are infinite hyperboloids of revolution described by

$$\frac{r^2}{r_0^2} - \frac{z^2}{z_0^2} = \pm 1, \tag{2.1}$$

where r_0 is the inner radius of the ring electrode, z_0 is half the distance between the two endcaps and the $+$ and $-$ sign refer to the ring electrode and endcap respectively. Also, by convention $r_0 = \sqrt{2}z_0$.

When a static electric potential U_0 is applied to the ring with respect to the end-caps, a quadratic electric potential of the form

$$U(r, z) = \frac{U_0}{R_0^2}(r^2 - 2z^2), \tag{2.2}$$

is created where $r^2 = x^2 + y^2$ and $R_0^2 = r_0^2 + 2z_0^2$ is a geometrical constant dependent on the size of the trap. To trap positively charged particles, U_0 is made negative. This sets up a minimum potential in the axial direction and a maximum in the radial plane. In the axial direction, the negatively charged particles experience an electric force towards the centre that is proportional to the displacement from the origin. This results in simple harmonic motion in the z-direction. In the radial plane however, any displacement from the trap centre will result in the particle being attracted towards the ring electrode. Trapping

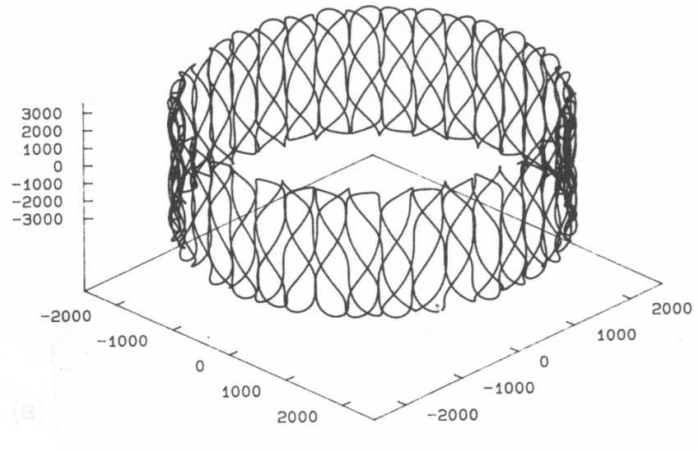

Figure 2.2: Trajectory of a singly charged ion stored in a Penning trap at $B = 1\text{T}$, $U_0 = 1\text{V}$ and $r_0 = 5 \times 10^{-3}\text{m}$. Taken from [35].

in the radial plane is achieved by applying a static homogeneous magnetic field, $\mathbf{B}$, along the z-axis. This causes a particle moving towards the ring electrode to go into a cyclotron-type orbit. Also, because of the combined presence of the electric and magnetic field, the particle experiences a crossed electric and magnetic field, ($\mathbf{E} \times \mathbf{B}$), type drift about the z-axis. This motion is called the magnetron motion. The particle's motion is a superposition of the simple harmonic motion in the z-direction and the cyclotron and magnetron motion in the radial plane. A typical ion trajectory confined in the Penning trap is shown in Fig. 2.2.

The equations of motion for a particle of charge q are solved to give

$$x(t) = r_+ \cos(\omega_+ t + \phi_+) + r_- \cos(\omega_- t + \phi_-), \tag{2.3}$$

$$y(t) = -r_+ \sin(\omega_+ t + \phi_+) - r_- \sin(\omega_- t + \phi_-), \tag{2.4}$$

$$z(t) = r_z \cos(\omega_z t + \phi_z), \tag{2.5}$$

where r_+, r_- and r_z are the amplitudes of the cyclotron, magnetron and axial oscillations respectively and ϕ_+, ϕ_- and ϕ_z are the initial phases of the respective motions. Also, ω_+, ω_- and ω_z are the modified cyclotron, magnetron and axial frequencies which are further defined below:

$$\omega_+ = \frac{1}{2}(\omega_c + \omega_1), \tag{2.6}$$

$$\omega_- = \frac{1}{2}(\omega_c - \omega_1), \tag{2.7}$$

$$\omega_z^2 = \frac{4q|U_0|}{mR_0^2}, \tag{2.8}$$

where we define the true cyclotron frequency, ω_c, as

$$\omega_c = \frac{qB}{m}. \tag{2.9}$$

Also we find that

$$\omega_1^2 = \omega_c^2 - 2\omega_z^2. \tag{2.10}$$

The cyclotron frequency is modified because of the electrostatic potential. However, for typical trap parameters, its value is very close to the true cyclotron frequency, ω_c, which is due to the magnetic field alone. Also, it is always true that $\omega_- < \omega_+$ and for normal trapping parameters $\omega_- \ll \omega_z \ll \omega_+ \approx \omega_c$. Typical values of these quantities in our trap are: $\omega_c/2\pi$ = 383kHz, $\omega_+/2\pi$ = 340kHz, $\omega_z/2\pi$ = 171kHz and $\omega_-/2\pi$ = 44kHz for trapping parameters of $r_0 = 5 \times 10^{-3}$m, $z_0 = 3.5 \times 10^{-3}$m, U_0 = 6V, $\mathbf{B}$ = 1T and $m = 6.64 \times 10^{-26}$kg.

The energy associated with the axial motion oscillates between potential and kinetic energy. This is true since the motion in this direction is simple harmonic. The energy associated with the magnetron motion is mainly in the potential form while the energy in the cyclotron motion is mainly kinetic. We can write down the Hamiltonian for a single trapped particle as [48]

$$H = \frac{1}{2}m\omega_1\omega_+ r_+^2 - \frac{1}{2}m\omega_1\omega_- r_-^2 + \frac{1}{2}m\omega_z^2 r_z^2. \tag{2.11}$$

From Eq. 2.11 we can see that the contribution of the magnetron motion to the overall energy is negative. This means that the magnetron motion is unstable and for it to be laser cooled, energy has to be added to this motion. Thus the cooling condition for this degree of freedom is opposite to that of the other degrees of freedom.

2.1.2 The Paul Trap

The Paul (or radiofrequency) trap has the same electrode configuration as the Penning trap. However, there is no magnetic field present and instead of a static electric potential, the Paul trap uses a time varying potential of the form U_0 - $V_0 \cos \Omega t$ to confine the ions. This results in the ion being stable in the axial direction and unstable in the radial direction for half the cycle and vice versa for the other half of the cycle. By choosing appropriate values for certain

parameters, stability in all three dimensions can be achieved.

The equations of motion for an ion of mass m and charge e are given by

$$\frac{d^2r}{dt^2} + \left(\frac{e}{mr_0^2}\right)(U_0 - V_0\cos\Omega t)r = 0, \tag{2.12}$$

$$\frac{d^2z}{dt^2} - \left(\frac{2e}{mr_0^2}\right)(U_0 - V_0\cos\Omega t)z = 0, \tag{2.13}$$

where r takes the value of either x or y. Eq. 2.12 and 2.13 can be parameterised by making the following substitutions:

$$a_z = -2a_r = -\frac{8eU_0}{mr_0^2\Omega^2}, \quad q_z = -2q_r = -\frac{4eV_0}{mr_0^2\Omega^2}, \quad \phi = \frac{\Omega t}{2}, \tag{2.14}$$

which generates the following set of Mathieu equations:

$$\frac{d^2r}{d\zeta^2} + (a_r - 2q_r\cos 2\zeta)r = 0, \tag{2.15}$$

$$\frac{d^2z}{d\zeta^2} + (a_z - 2q_z\cos 2\zeta)z = 0. \tag{2.16}$$

The solutions to the Mathieu equations are stable only for certain values of a and q [52]. The regions of stability for the z-direction and for both the z-direction and the radial plane are shown in Fig. 2.3(a) and 2.3(b) respectively. Thus in three dimensions, the ion can only be trapped when both the regions of stability overlap in the $a - q$ plane. The usefulness of the Paul trap as a mass selective device can easily be seen by examining the expressions for q and a. From Eq. 2.14, it is possible to trap only certain e/m values by choosing appropriate values of U_0 or V_0 if r_0^2 and Ω are kept constant.

The motion of ions in a Paul trap is a combination of a low frequency motion called the secular motion and a higher frequency motion called the micromotion. The secular motion can be obtained by averaging the effect of the r.f. field over one cycle. This results in the motion of the ions being a simple harmonic motion that is due to a parabolic pseudopotential [23]. The secular frequency, ω_i, can be defined as

$$\omega_i = \frac{\beta_i\Omega}{2}, \tag{2.17}$$

where Ω is the micromotion frequency, $i = z, r$ and the parameter β_i, is aprroximately given as

$$\beta_i \approx \sqrt{a_i + \frac{q_i^2}{2}}. \tag{2.18}$$

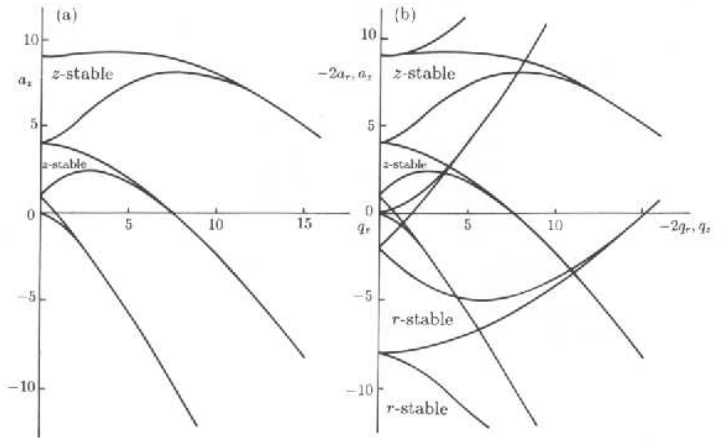

Figure 2.3: (a)The z stability regions. (b)The z and r stability regions. Figure taken from [35].

A typical ion trajectory in the Paul trap showing both the secular and micromotion is shown in Fig. 2.4. The depth of this pseudopotential well is the difference between the potential at the trap centre and the electrodes. For the r-direction this can be expressed as

$$D_r = \frac{eV^2}{4mr_0^2\Omega^2}, \tag{2.19}$$

while the depth in the z-direction is given as

$$D_z = \frac{eV^2}{4mz_0^2\Omega^2}. \tag{2.20}$$

2.1.3 The Linear Paul Trap

The linear Paul trap is a variant of the conventional Paul trap. The electrode configuration has cylindrical geometry and is shown in Fig. 2.5. The radial confinement is provided by applying a time varying r.f. potential across diagonally opposing rods while the other two rods are grounded. Axial confinement is provided by applying a static potential across the two end caps. By choosing appropriate trap parameters, the radial confinement can be made much stronger than the axial confinement, thereby forcing the ions to line up along the axis of the trap. This is desirable in the field of quantum information processing (QIP) as the micromotion which causes heating is vanishingly small along the axis where the E-field is zero. This is in contrast to a conventional Paul trap where only one ion can be free of micromotion since this condition only exists

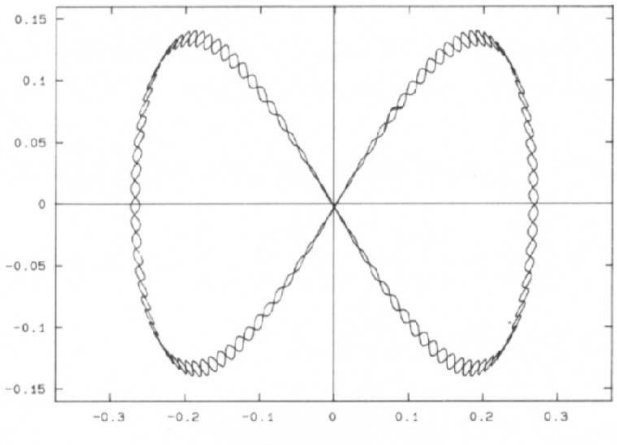

Figure 2.4: Trajectory of a single Al^+ ion in a Paul trap on the $x - z$ plane (scale in cm) with $a_z = -3.5 \times 10^{-6}$ and $q_z = 0.095$. Figure taken from [35].

at the centre of the trap.

2.1.4 The Miniature Paul Trap

It will be shown in Sec. 3.8.2 of Chap. 3 that high trap oscillation frequencies are useful in QIP applications. The highest secular frequency achievable in a Paul trap is given by [45]

$$\omega_z = \frac{2}{R_0^2}\sqrt{\frac{qV_0}{0.908m}}, \tag{2.21}$$

which is achieved without any d.c. potential applied onto the electrodes. It can be seen from Eq. 2.21 that high secular frequencies can be obtained for a specific mass to charge ratio by either making V_0 larger or making R_0 smaller. However, there is a limit to the maximum value of V_0 imposed by the material used for the electrodes. Too high a value of V_0 will cause a potential breakdown and cause arcing across the insulating spacers used to hold the electrodes apart. The obvious limitation in building smaller traps is the difficulty in machining it. Typical miniature trap dimensions are $\sim 200\mu$m. Secular frequencies of the order of tens of MHz have been achieved with Mg^+ and Be^+ ions [45].

2.1.5 The Combined Trap

The combined trap is obtained by having both the magnetic field and the r.f. field present simultaneously. The equations of motion of an ion confined in a combined trap are [6]

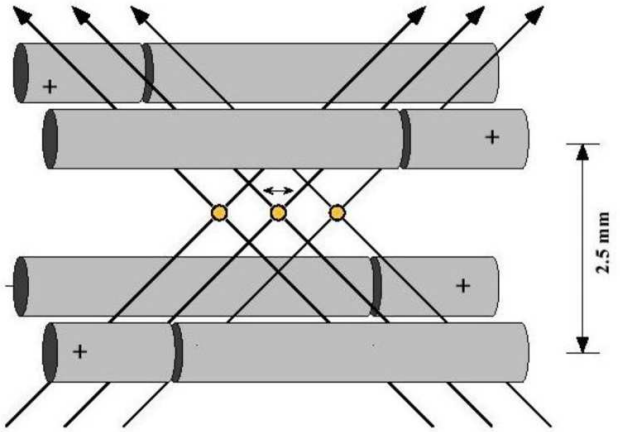

Figure 2.5: Electrode configuration of a linear Paul trap. Figure taken from [73].

$$\frac{d^2x}{d\zeta^2} + (a_r - 2q_r \cos 2\zeta)x = 2\frac{\omega_c}{\Omega}\frac{dy}{d\zeta}, \tag{2.22}$$

$$\frac{d^2y}{d\zeta^2} + (a_r - 2q_r \cos 2\zeta)y = 2\frac{\omega_c}{\Omega}\frac{dx}{d\zeta}, \tag{2.23}$$

where

$$a_r = -\frac{4eU_0}{m\Omega^2 r_0^2}, \quad q_r = -\frac{2eV_0}{m\Omega^2 r_0^2}. \tag{2.24}$$

The motion in the z-direction remains unchanged from that in the Paul trap. The equations can be uncoupled by changing from the laboratory frame to a frame $(\widetilde{x}, \widetilde{y})$ that is rotating at a frequency of $\omega_c/2$. This gives

$$\frac{d^2\widetilde{x}}{d\zeta^2} + (a_r + g^2 - 2q_r \cos 2\zeta)\widetilde{x} = 0, \tag{2.25}$$

$$\frac{d^2\widetilde{y}}{d\zeta^2} + (a_r + g^2 - 2q_r \cos 2\zeta)\widetilde{y} = 0, \tag{2.26}$$

where $g = \omega_c/\Omega$. Eqs. 2.25 and 2.26 look similar to the Matthieu equation, where instead of a_r we now have $a_r + g^2$. Therefore, for the combined trap, effectively we have

$$a_r = \left(\frac{\omega_c^2}{\Omega^2} - \frac{4eU_0}{m\Omega^2 r_0^2}\right), \quad q_r = -\frac{2eV_0}{m\Omega^2 r_0^2}. \tag{2.27}$$

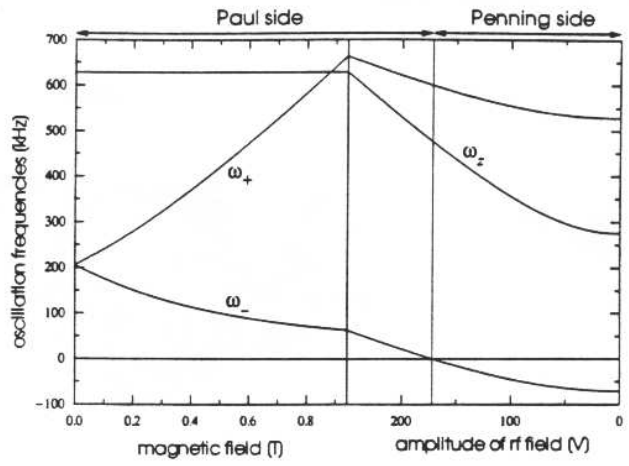

Figure 2.6: Oscillation frequencies in the combined trap as a function of the magnetic field and amplitude of the r.f. drive. Taken from [40].

The q_r parameter is the same as in the Paul trap. Using the relation $\beta_i = \sqrt{a_i + (q_i^2/2)}$ we can write

$$\beta_r \approx \sqrt{\left(\frac{\omega_c^2}{\Omega^2} - \frac{4eU_0}{m\Omega^2 r_0^2}\right) + \frac{1}{2}\left(\frac{-2eV_0}{m\Omega^2 r_0^2}\right)^2}. \tag{2.28}$$

The oscillation frequencies for both the radial and axial directions can be found using the relation $\omega_i = \beta_i \Omega/2$ so that

$$\omega_r = \frac{\beta_r \Omega}{2}, \qquad \omega_z = \frac{\beta_z \Omega}{2}. \tag{2.29}$$

In the laboratory frame, the frequencies are

$$\omega_\pm = \frac{\omega_c}{2} \pm \omega_r, \quad \omega_z. \tag{2.30}$$

The oscillation frequencies of ions in a combined trap are illustrated using Fig. 2.6. The left half of the diagram shows how the frequencies in the combined trap vary as the amplitude of the r.f. is kept constant while the magnetic field is varied. The far left side represents a pure Paul trap. It can be seen that the degeneracy of the radial oscillation frequencies is lifted when a magnetic field is applied. On the right half, the magnetic field is kept constant while the r.f. amplitude is varied. The far right represents a pure Penning trap. The negative energy associated with the magnetron motion is represented by a negative oscillation frequency. As the r.f. amplitude is increased past a certain value, the polarity of the magnetron oscillation frequency is swapped. At this

point, the potential associated with it changes from a potential hill to a potential well. This also causes a change in the sense of rotation. Once $\omega_- > 0$, the energy associated with the magnetron motion is positive which means that the complications involved with cooling this degree of motion are removed.

The advantage of this trap is that a larger stability region can be obtained. Also, it allows for the simultaneous trapping of positively and negatively charged ions. This is possible because of the additional term ω_z^2/Ω^2 in Eq. 2.28. For a strong magnetic field, $\omega_z^2/\Omega^2 \gg |4eU/m\Omega^2 r_0^2|$, which means that β_r will always remain positive. This may be useful in experiments involving the production of antihydrogen [50].

2.2 Laser Cooling of Trapped Ions

Laser cooling of trapped ions was first proposed by Wineland and Dehmelt in 1975 [79]. There are several reasons for cooling stored ions. The first is to increase the ion storage time. When the ions are first loaded into the trap, they are not always created at the centre of the trap, which means that they gain kinetic energy as they fall into the trap centre. Also, the technique of producing ions by crossing an electron beam with an atomic beam means that the ions are hot just after they are generated. Without cooling, they are easily lost as they can collide with other particles (e.g. background gas molecules) and overcome the potential well. Other reasons for cooling are found in applications such as high resolution spectroscopy and quantum information processing. The former is possible because cooling greatly reduces Doppler effects while cooling techniques are used in the latter to prepare the ion in its ground vibrational state before logic operations are performed.

There are several cooling schemes available. These include laser cooling, resistive cooling [24, 39], collisional cooling [2] and sympathetic cooling [49]. Of these, only laser cooling will be described in more detail here.

Laser cooling of trapped ions can be treated in two different limits, the heavy particle limit and the fast particle limit. In the heavy particle limit, the ion oscillation frequency is small compared to the spontaneous transition probability. Laser cooling in this regime resembles that of a free particle. The lowest achievable temperature is known as the Doppler limit. In the fast particle limit, the opposite occurs: the ion oscillation frequencies are greater than the spontaneous transition probability. The consequence of this is that motional sidebands appear in the emission spectrum, which provides us with a different cooling mechanism called sideband cooling. Here, the laser can be tuned to one of the lower sidebands to progressively reduce the energy of the ion. Sideband cooling allows the possibility of cooling to the vibrational ground state of motion.

The sideband cooling scheme can be modified such that it becomes a two photon process. This type of cooling is called Raman sideband cooling. All three laser cooling schemes mentioned above will be described in more detail in this section.

The laser cooling schemes mentioned above are applicable to both ions trapped in the Paul and Penning traps. However, due to the peculiarity of the magnetron motion of the Penning trap, the laser cooling technique needs to be slightly modified to accommodate for this. The laser cooling techniques used in both the Paul and Penning traps are described in the final part of this section.

2.2.1 Laser Cooling to the Doppler Limit

The principle behind Doppler cooling is described here. Consider a two-level ion with the ground and upper state separated by an energy of $\hbar\omega_0$. It is assumed that the upper level decays to the ground level by a one-photon electric-dipole transition at a rate γ. The two-level ion is subjected to laser radiation of frequency ω, where the individual photons of this radiation have an energy of $\hbar\omega$ and carry momentum given by $\hbar k$, with k being the wavevector associated with monochromatic radiation of wavelength λ ($k = 2\pi/\lambda = \omega/c$). The ion travelling with velocity v towards the laser will see a Doppler shifted laser frequency of $\omega + \omega v/c$. If the laser is tuned below the transition frequency ω_0 such that the difference between ω_0 and ω (or the detuning $\Delta = \omega_0 - \omega$) exactly matches the Doppler shift, $\omega v/c = kv_z$, the ion will absorb the photon of energy $\hbar\omega$. As a result of this, the ion's momentum will be reduced by $\hbar k$. The ion is now in its excited state and will decay back to the ground state either by stimulated emission or spontaneous emission. If stimulated emission occurs, the direction of the emitted photon (and thus its momentum) will the same as that of the absorbed photon. This results in the two momentum contributions cancelling out leaving the ion's momentum unchanged. However, if spontaneous emission occurs, the photon will be given off in a random direction such that over many emissions, the average effect of the emission on the ion's momentum is zero. The net effect of an absorbtion-emission will be a reduction in the ion's momentum.

Although the above is true, the mean squared momentum is not equal to zero. This is due to fluctuations associated with both the randomness of the direction and the randomness of the time distribution of the re-emitted photon. The change in the ion's momentum is a random walk process with each step representing an emission process. The ion is heated by this effect which is known as recoil heating. The minimum temperature is obtained when the Doppler cooling rate exactly matches the recoil heating rate. The lowest achievable temperature using Doppler cooling is given as [81],

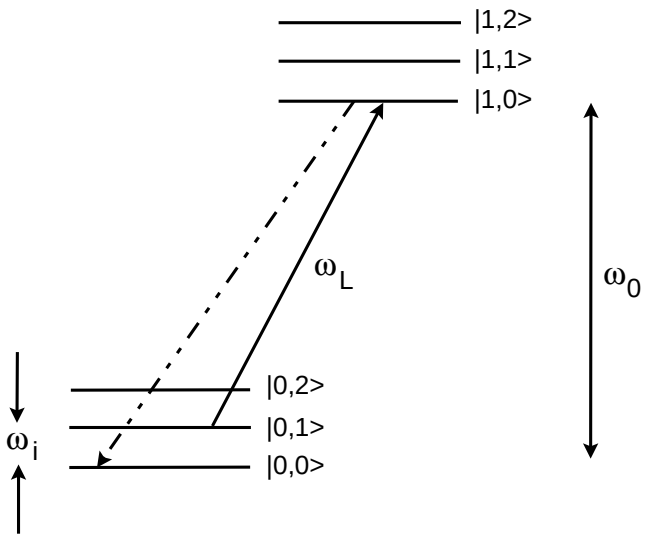

Figure 2.7: Modified energy levels in the resolved sideband limit.

$$T_{limit} = \frac{\hbar\Gamma}{2k_B}, \tag{2.31}$$

where Γ is the natural linewidth of the cooling transition and the other symbols have their usual meaning. To achieve this temperature, the cooling laser must be detuned by half the linewidth below resonance ($\Delta\omega = -\Gamma/2$).

2.2.2 Resolved Sideband Cooling

Laser cooling of trapped ions in the fast particle limit allows for a different kind of cooling mechanism called resolved sideband cooling. This can be best described by treating the energy of the ion quantum mechanically which results in the trapped ion having discrete energy levels. Furthermore, if the ion is bound by a *harmonic* potential, it will have energies which are described by

$$E = \hbar\omega_i \left(\frac{1}{2} + n\right), \tag{2.32}$$

where n is the vibrational quantum number and ω_i is the vibrational oscillation frequency of the trapped ion. Also, if $\omega_i \gg \gamma$, where γ is the spontaneous decay rate, the energy levels will be resolved. The ion energy level structure will then be modified to look like Fig. 2.7 where each electronic level will have a discrete ladder of energies corresponding to different vibrational quantum numbers.

If ω_0 is the difference in energy between the ground and the first electronic excited state (both with the same vibrational number), then sideband cooling

can be effected by tuning a laser to the first red sideband such that

$$\omega_L = \omega_0 - \omega_i, \tag{2.33}$$

where ω_L is the laser frequency. The ion will be raised to the first electronic excited state but lowered by one vibrational number. When the ion decays back into the ground electronic state, on average, the vibrational quantum number will be conserved thereby reducing the overall vibrational quantum number by one. The zero change in the vibrational number is similar to the Franck-Condon overlap in molecular transitions where the strongest transition occurs when the overlap in wavefunctions is greatest. If this process of tuning the laser to the red sideband is repeated, the ion's energy will be optically pumped down to its ground vibrational state.

Laser cooling using this technique was first demonstrated on a single Hg^+ ion [27] confined in a Paul trap. Here, the trap oscillation frequency of $\omega_i/2\pi =$ 2.96MHz was obtained. The sideband cooling step was preceded by Doppler cooling. The Doppler cooling was performed by tuning a laser at 194nm onto the $^2S_{1/2} \rightarrow {}^2P_{1/2}$ transition. Once the Doppler limit of $\langle n \rangle \approx 12$ was obtained, the 194nm radiation was turned off and the narrow $^2S_{1/2} \rightarrow {}^2D_{5/2}$ transition was driven using a laser at 281.5nm. Since the natural linewidth of the $^2D_{5/2}$ transition is of the order of 1Hz, the criterion that $\omega_i \gg \gamma$ is satisfied. However, this also means that the sideband scattering rate is only of the order of six photons a second. To increase this rate, a laser at 398nm was used to couple the $^2D_{5/2}$ level to the $^2P_{3/2}$. Only the y- and z- degrees of freedom were cooled where the values of $\langle n_y \rangle$, $\langle n_z \rangle = 0.051$ were achieved. When $\langle n \rangle \ll 1$, the value of $\langle n \rangle$ can be determined easily by measuring the asymmetry in the absorption spectrum. As $\langle n \rangle$ approaches zero, the amplitude of the lower sideband becomes very small since there is no vibrational energy level that it can couple to. The ratio of the amplitudes of the lower to upper sidebands gives the value of $\langle n \rangle$.

A similar experiment was recently performed using a single Ca^+ ion in a Paul trap [61]. The scheme is similar to that described above for cooling of the Hg^+ ion. Doppler cooling is facilitated by the $4^2S_{1/2} \rightarrow 4^2P_{1/2}$ transition using laser radiation at 397nm. Sideband cooling is performed on the $4^2S_{1/2} \rightarrow 3^2D_{5/2}$ transition where again the $3^2D_{5/2}$ level is coupled to the $4^2P_{3/2}$ level using an 854nm laser to increase the sideband cooling rate. Only the y- and z- degrees of freedom were cooled where the vibrational ground state population was achieved with up to 99.9% probability.

2.2.3 Raman Sideband Cooling

Sideband cooling requires a "weak" (i.e. the linewidth of the metastable level is narrower than the separation of the vibrational levels) transition that is accessible via optical radiation. This criterion is only satisfied in very few ions. A different technique called Raman sideband cooling allows this criterion to be lifted [55]. It does so by making use of a stimulated Raman transition between two ground state sublevels to serve as a "weak" transition. The general principle of stimulated Raman sideband cooling can be described as follows. Consider a four-level system as shown in Fig. 2.8. The levels are labelled as $|J, n\rangle$, where J represents the internal energy levels and n represents the vibrational energy levels. Let us assume that the ion is initially in the $|1, n\rangle$ level. The ion is then addressed with two laser beams whose frequencies are

$$\omega_1 = \omega_{01} - \Delta - \omega_i, \tag{2.34}$$

$$\omega_2 = \omega_{02} - \Delta, \tag{2.35}$$

where ω_{01} and ω_{02} are the transition frequencies between the levels $|0, n\rangle$ and $|1, n\rangle$ and $|0, n\rangle$ and $|2, n\rangle$ respectively and ω_i is the vibrational oscillation frequency. The difference frequency $\omega_1 - \omega_2$ is set such that the ion loses one vibrational quantum of energy each time a stimulated Raman transition takes place. This transition sends the ion into the $|2, n-1\rangle$ level. To complete the cooling process, a laser which addresses the $|2, n-1\rangle \rightarrow |aux\rangle$ transition is applied. This induces spontaneous Raman transitions which send the ion into the $|1, n-1\rangle$ level. The nature of the spontaneous Raman transitions is such that on average, over many transitions, the vibrational quantum number is conserved. By repeating this process several times, the ion is optically pumped into the ground vibrational state.

The two laser beams used are derived from the same laser using an acoustic optical modulator to offset the frequencies. This allows for a much narrower effective laser linewidth. Also, the induced natural linewidth can be made very narrow by increasing the detuning, Δ.

Raman sideband cooling has been demonstrated by Monroe in 1995 [55]. The experiment was performed with a single Be^+ ion confined in a Paul trap. Raman sideband cooling was performed in all three dimensions where the values of $\langle n_x \rangle, \langle n_y \rangle, \langle n_z \rangle = 0.033, 0.022, 0.029$ were achieved.

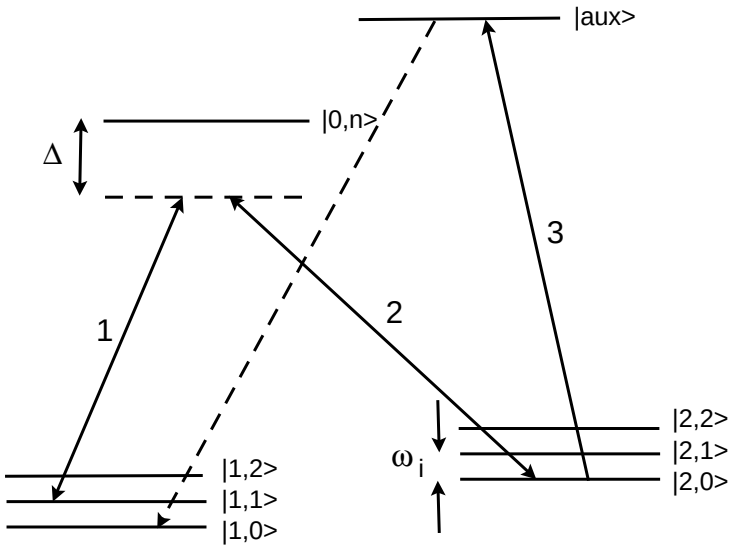

Figure 2.8: Energy level scheme for Raman sideband cooling.

2.3 Laser Cooling in the Paul Trap

Laser cooling in the Paul trap was first demonstrated by Neuhauser in 1978 [57]. The ion motion in the Paul trap in the three dimensions can be treated as simple harmomic. Laser cooling in all three dimensions can be achieved using just a single laser if the beam direction is offset from the $y-z$, $x-z$ and $x-y$ plane such that there are momentum components in the x-, y- and z- directions. For a large cloud of ions the minimum achievable temperature for Doppler cooling is limited by r.f. heating.

2.4 Laser Cooling in the Penning Trap

Laser cooling in the Penning trap, first demonstrated by Wineland in 1978 [80], needs to be treated differently from cooling in the Paul trap. This difference is due to the motion of the ion in the Penning trap which is comprised of three superimposed motions - the harmonic oscillation in the z-direction, the modified cyclotron motion and the magnetron motion. The axial motion is cooled in the same way as in the Paul trap. To laser cool the cyclotron motion, the laser beam direction needs to be set such that the laser interaction is maximised when the ion is moving towards the laser. The opposite is true for the magnetron motion, where it needs to be addressed such that the laser is interacting with the ion only when it is moving away from the laser. The optimum beam position for cooling all degrees of motion is then to offset the beam diagonally from the $x-y$

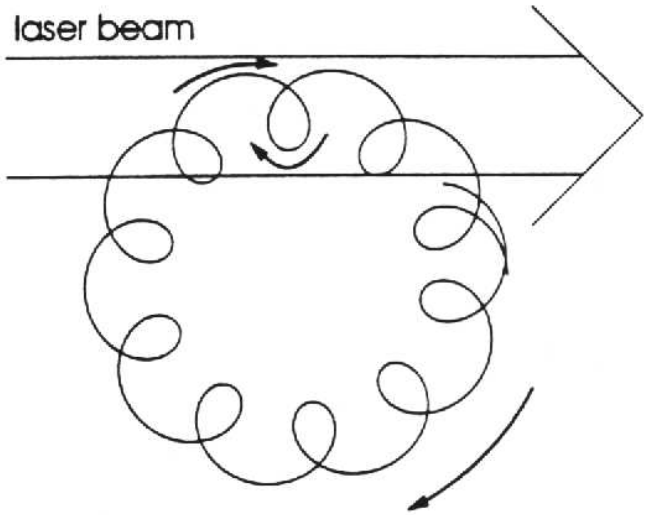

Figure 2.9: Beam offset position in the radial plane for cooling both the radial motions in the Penning trap.

plane(to cool the axial motion) and to translate the beam so that it is offset from the centre of the ion orbit such that there is an intensity gradient across the ion orbit [43]. The optimum beam position for the radial plane is shown in Fig. 2.9.

Another important consideration when laser cooling in the Penning trap is the polarisation of the laser radiation. As the magnetic field applied for the operation of the Penning trap Zeeman splits the energy levels, care must be taken over the choice of polarisation so as to avoid optical pumping into dark states.

2.5 Review of ion trapping experiments with Ca^+ ions

2.5.1 University of Innsbruck

The ion trapping group at Innsbruck are trapping and laser cooling Ca^+ ions for use in quantum information processing (QIP) studies (for more on QIP see Chapter 3). A linear r.f. trap is used to store the ions in a string along the trap axis. Their main experimental aim is to implement a quantum information processor following the Cirac and Zoller [19] scheme. Several important

steps toward this goal have been achieved which include sideband cooling to the ground motional state, coherent driving of the qubit state [61] and the individual addressing of ions [56]. More recently, two very important milestones were achieved. The first was the realisation of the Deutsch-Jozsa algorithm [38] and the second was the realisation of the Cirac-Zoller controlled-NOT (CNOT) quantum gate [66]. Although the CNOT gate has already been implemented by Monroe in 1995 [55] (where this was done by using a single Be^+ ion with the internal and external states representing the two qubits), the CNOT gate implemented by the Innsbruck group involves the use of two individual Ca^+ ions as the two qubits. The fidelity of this two ion CNOT gate is limited mainly by laser frequency noise, the ability to address the qubits individually and unwanted off-resonant excitations. However, this demonstration has provided a strong basis from which more complex gate operations can be investigated towards the realisation of a many qubit QIP.

2.5.2 University of Oxford

The experiments performed at Oxford are aimed at understanding fundamental issues in quantum mechanics, in particular the area of quantum information theory. To achieve this, they have built a linear r.f. ion trap for storing and laser cooling Ca^+ ions such that it can be used as a quantum system for exploring the physics of quantum information. Recent developments indicate that they are moving towards the use of ^{43}Ca from the more abundant $^{40}Ca^+$ isotope for use in quantum information studies. The advantage of the $^{43}Ca^+$ ion is the presence of the ground hyperfine levels which, when used for encoding the qubit, can in principle provide a much longer coherence time. Since the natural isotopic abundance of ^{43}Ca is low at 0.14%, a loading mechanism that was isotope-selective has been developed. Here, they have successfully implemented the photoionisation technique to selectively load only $^{43}Ca^+$ ions. The other recent development involves experiments on the state read out (state detection) for a qubit spanned by the ground states of the $^{40}Ca^+$ ion.

2.5.3 Johannes-Gutenburg University

Ca^+ ions are trapped and laser cooled in the linear Paul trap for use in several types of studies. The first investigates the dynamics of laser cooled trapped ions. Here, they have managed to observe different crystalline structures which depend on the symmetry and strength of the applied trapping potential [11]. The group have also measured the lifetime of the $3^2D_{5/2}$ level of Ca^+ using the quantum jump technique on a single Ca^+ ion [12]. The lifetime was measured to be 1100(18)ms. In another experiment, isotopic shifts present in sample of

Ca^+ containing the masses 40, 42, 43 and 44 were measured [1]. These shifts provide useful information about the structure of the atomic nuclei through the hyperfine effect in the atomic structure.

Chapter 3

Introduction to Quantum Computing

This chapter consists of two main sections. The first provides an introduction to the area of quantum computing. It seeks to outline the concepts and basic ideas behind the operation of a quantum computer. The necessary components required for the realisation of a quantum computer are also described. The second section describes two of the most promising candidates for physically realising a quantum computer - the nuclear magnetic resonance system and the ion trap system. A more thorough description is given for latter approach as it bears more relevance to the work presented in this thesis.

3.1 Brief History of Quantum Computing

The idea of using the laws of quantum mechanics to perform computations was first explored in the early 1970's. This was prompted by the realisation that the amount of information stored on a unit area of a silicon chip doubles every 18 months. Interpreted in a different way, this also means that computing speeds double every 18 months (Moore's Law). This implies that the components that make up the chip are getting smaller and smaller. Soon the components will be so small that they literally consist of only a few atoms. On this scale, different laws of physics, namely quantum mechanics begin to dominate. Once this stage is reached, if computers are to get any faster, different methods of processing information must be invented. At this point scientists began to look into the possibility of harnessing quantum effects for use in information processing.

Early attempts at using quantum mechanics for computation were made by Charles Bennett of the IBM Thomas J. Watson Research Center and Paul A.

Benioff of the Argonne National Laboratory. Bennett showed that a universal computing machine (Turing machine) could be made entirely out of reversible gates [9]. A reversible gate is one in which the input can be deduced from the output. Bennett's insight was an important one since quantum evolution is also a reversible process and for a computer based on a quantum system to exist, it must first be possible to construct a reversible classical Turing machine. This led Benioff to propose the idea of using quantum systems which could be made to behave like a reversible Turing machine by the application of suitable Hamiltonians [7, 8]. This theoretical construct showed that a quantum mechanical Turing machine could in principle be as efficient at performing computational tasks as a classical Turing machine.

The next insight came in 1982 when Richard Feynman of the California Institute of Technology proposed a quantum simulator, a device that would be able to simulate any physical system [32, 33]. According to Feynman, a quantum simulator would be able to compute certain computational tasks far more efficiently than a classical computer due to the following argument.

The simulation of the evolution of a quantum system on a classical computer cannot be done efficiently. A slow-down occurs because of the exponentially increasing amount of information required to describe the quantum evolution. On the other hand, if a quantum evolution can be harnessed to simulate a computational task, then an exponential speed up in the processing time could be gained. Unfortunately, Feyman's proposal did not succeed in fully describing a quantum computer, but did however, serve to demonstrate the potential computing power available using quantum effects.

The breakthrough finally came in 1985 when David Deutsch of the University of Oxford published a crucial theoretical paper which is widely considered as the blue print for a quantum computer [25]. In his paper, he described a string of two-state systems which are made to evolve using a specific set of operations such that it is able to simulate the evolution of any physical system. The crucial discovery here was the set of operations used to evolve the quantum system which we know today as quantum gates.

3.2 Basic Principle

In 1801, Thomas Young performed the famous double-slit experiment which served to demonstrate the wave nature of light. In more modern times, the experiment has also been used to demonstrate quantum interference effects. This can be achieved by performing the double-slit experiment with a slight modification. Before describing this, it is worth reminding ourselves of the original experiment performed by Young. The experiment involves shining a

single light source onto two slits and observing the resulting light pattern formed at a screen behind the slits. If either one of the slits is closed, then the pattern would be a single bright line directly behind the remaining open slit. However, if both slits are open, then a series of light and dark fringes will appear on the screen. This is due to interference of the light waves emitted from the two slits. To demonstrate quantum interference effects, the intensity of the light source is reduced to the point that only one photon is emitted at a time. What happens to the photon? Intuitively, we would expect the photon to only pass through either one of the two slits, randomly choosing between the two. If this is true, then repeating the experiment many times will result in the formation of two bright lines of equal intensities, one directly behind each slit. However, experiments have shown that an interference pattern forms on the screen behind the two slits. The inconceivable conclusion favoured by Deutsch is that the photon actually travels through the two slits simultaneously and interferes with itself. In Deutsch's interpretation, the photon is said to exist in parallel universes, where in one universe, it travels through one of the slits while in the other universe, it travels through the other. This many universes theory can be applied to quantum computing which has vast implications as will be explained below.

The basic unit of information stored on a quantum computer is called a qubit, the quantum analogue to the bit. Physically, the qubit can be any two-state quantum mechanical system with one state signifying a 0 and the other state signifying a 1. However, instead of existing in just one of the two states at a time, a qubit state can be a superposition of a 0 and a 1. This superposition state is similar to the one evident in the double-slit experiment where just as the photon can be in two places at a time, the qubit can be in more than one state at a time. The quantum state of the qubit can be represented by

$$|\psi\rangle = c_0|0\rangle + c_1|1\rangle, \tag{3.1}$$

where c_0 and c_1 are complex coefficients which represent the probability amplitude that the qubit in the state $|0\rangle$ and $|1\rangle$ respectively such that $|c_0|^2+|c_1|^2 = 1$. The states $|0\rangle$ and $|1\rangle$ are said to be mutually orthogonal.

The superposition of states can be extended to more than just a single qubit. For example, in a quantum system consisting of two qubits, the quantum state of this ensemble can be represented by

$$|\psi\rangle = c_0|00\rangle + c_1|01\rangle + c_2|10\rangle + c_3|11\rangle, \tag{3.2}$$

where again the coefficients, $c_i (i = 0, 1, 2, 3)$, represent the probability amplitudes of each of the four orthogonal qubit states. A quantum system with n

number of qubits prepared in a superposition (in what is called a quantum register) will contain 2^n orthogonal states. To perform a computation, each of the 2^n orthogonal states can be used to physically represent a number. Then performing a physical operation on this quantum register will result in the operation being carried out simultaneously on all the 2^n inputs to produce a result which is a superposition of all the possible outputs. Thus quantum effects have allowed a form of highly efficient parallel computing. For a classical computer to achieve the same result, it would have to perform this operation 2^n times or have 2^n computers running in parallel. However, the rules of quantum mechanics only allow one number to be retrieved when a measurement is made on such a quantum register. In spite of this, it is still possible to take advantage of massive parallel computing power by the use of clever algorithms as will be shown in the next section.

3.3 Quantum Algorithms

A quantum computer will not be quicker than a classical one at every computing task. The quantum computer has the advantage only when it is able to make use of quantum interference effects to produce a single outcome that is dependent on all the inputs. In order to exploit its potential power, useful algorithms need to be invented first. The action of two of the most useful algorithms, namely Shor's factorising algorithm and Grover's search algorithm will be described in the following sections.

3.3.1 Shor's Algorithm

This algorithm was invented by Peter Shor of AT&T's Bell Laboratories in 1994 and is designed for factorising large integers efficiently [67]. This algorithm, if successfully executed on a quantum computer will compromise the security of modern day encryption systems particularly the RSA [60] (Rivest, Shamir and Aldeman) system which is widely used by financial institutions to protect their electronic accounts. This is because the security of such a system depends on the intractability of factorising large integers. Currently, the largest number that has ever been factorised by a classical computer has 129 digits. In contrast, a quantum computer would be able to store all the N digits in a superposition and perform a computation on all of them simultaneously. This quantum parallism could in principle, allow the task of factorising a 129 digit number to be performed in a matter of seconds. Increasing the number of digits does add to the time it takes to complete the task on a quantum computer but this only grows as N^3 [28, 30]. On a classical computer, the time it takes to factorise a

number with N digits grows exponentially with N.

3.3.2 Grover's Algorithm

In 1997, Lov Grover of AT&T's Bell Laboratories discovered an algorithm that allows a quantum computer to search an unsorted list of N items much quicker than a classical computer would [37]. An application of this, for example, would be to find a specific number in a telephone directory containing millions of entries. A classical computer would attempt to solve this by searching through the list one by one until the specific entry is found. This would take of order $N/2$ steps. Using Grover's algorithm, a quantum computer would be able to accomplish this search in approximately $\sqrt{N}$ steps. This represents a speed up by a factor of about $\sqrt{N}/2$. It was also later proven that Grover's algorithm is optimal, i.e. no algorithm can do better than of order $\sqrt{N}$ steps [15].

This algorithm also has implications in issues related to security. The Data Encryption Standard (DES) uses a 56-bit key to encrypt data. The task of breaking this code essentially requires finding a specific key out of a possible 2^{56} keys. It is estimated that the fastest of today's supercomputers would take years to accomplish this task while a quantum computer running Grover's algorithm would take only a matter of minutes.

3.4 Quantum Gates

Quantum gates are simple unitary operations that act on the qubits. These operations are carried out by applying Hamiltonians that cause the quantum system to undergo the desired transformations. Examples of this are the NOT and IDENTITY operators which have the same effect as their classical counterpart. Other operations, for example, the Square Root of NOT (SRN) gate have no classical counterpart. This gate has the effect of flipping the qubit only half way. To illustrate this, we take the example of qubits in the form of trapped ions where the ground state represents a $|0\rangle$ and the upper state represents a $|1\rangle$. Lets say the ion is initially in the $|0\rangle$ state. The SRN gate is implemented by applying a laser pulse of well defined frequency and intensity for a period of time such that it is just sufficient to flip the qubit halfway between the $|0\rangle$ and $|1\rangle$ state. The result of this is a qubit in the state shown in Eq. 3.3, which is a superposition of both the $|0\rangle$ and $|1\rangle$ states.

$$U|0\rangle = \frac{1}{\sqrt{2}}(|0\rangle + |1\rangle). \tag{3.3}$$

Applying the (SRN) gate again causes the superposition state to flip to a $|1\rangle$ thus effecting a NOT gate.

Another class of gates that are of interest in quantum computing is the controlled U gate, where U is a single-qubit operation. The action of this gate is to affect the state of the second qubit if and only if the state of the first qubit is in the $|1\rangle$ state. For this reason, the first qubit is called the control qubit and the second is called the target qubit. An example of this is the controlled-NOT (CNOT) gate where the second qubit undergoes a NOT if and only if the first qubit is in the $|1\rangle$ state. The truth table for the CNOT gate is shown in Eq. 3.4.

$$\begin{aligned} |00\rangle &\rightarrow |00\rangle \\ |01\rangle &\rightarrow |01\rangle \\ |10\rangle &\rightarrow |11\rangle \\ |11\rangle &\rightarrow |10\rangle. \end{aligned} \tag{3.4}$$

The SRN gate described earlier belongs to a group of operations known as single-qubit rotations. It can be shown that repeated use of operations in this group along with the CNOT operation are sufficient to produce any unitary transformation and therefore form a universal quantum gate [25]. This is analogous to the classical universal gate - the NAND which is able to produce the action of any other gate by its repeated use on different bits.

3.5 Decoherence

The potential power behind a quantum computer lies in the quantum superposition of states and interference effects that occur between them. Unfortunately, the fragility of such quantum superpositions is well known. When disturbed, the superposition is lost and the state ends up in either the $|1\rangle$ or the $|0\rangle$ state. The destruction of this coherent superposition is known as decoherence. It would appear that this problem is unavoidable. QIP requires the qubits to couple to each other. When they do, it is likely that they will couple to the environment too. Although there exist systems that are well isolated from the environment and therefore are decoherence free (e.g. the fullerene qubit where the nuclear spin of a single dopant atom inside a cage of carbon atoms represents the qubit), the qubits are not so easily manipulated for use in QIP.

The issue of decoherence is being addressed in two main ways. The first is by finding physical quantum information processing (QIP) schemes which are less susceptible to decoherence effects. An example of this is the scheme proposed

by Mølmer and Sørensen in the trapped ion approach [70]. The second method is to use quantum error correcting codes to improve the fidelity of quantum operations. The discovery of error correcting codes represents a crucial step in the path to realising a quantum computer as even the best controlled physical systems used to implement QIP schemes will be confronted with the problem of noise. Quantum error correction allows the possibility for real physical systems to approach the noise free ideal models that allow for exact realisations of quantum computing.

The first quantum error correcting codes were presented by P.W. Shor [68] and A.M. Steane [72]. The basic ideas behind these schemes are derived from classical error correcting schemes. The essential principle behind it involves the use of surplus numbers of qubits to encode the information. For example, a single bit of information, 0 or 1 can be encoded using three qubits such that a $|000\rangle$ represents a 0 and a $|111\rangle$ represents a 1. If one of the three qubits undergoes a random flip, the information held by the group of qubits can still be deduced by way of majority logic where if the majority of three qubits is 1 then the output is 1, otherwise it is 0. In this way, the quantum information is made more tolerant against decoherence effects. Also, it can be seen intuitively that the above method can be improved by increasing the redundancy in the number of qubits. Indeed it has been proven that increasing the redundancy causes the failure probability of the quantum error correction to fall off exponentially; provided certain conditions are met which are: i) quantum error correction is performed in the limit of large redundancy and ii) the error rate is below a certain level [72, 17].

3.6 Physical Realisations of a Quantum Computer

A general prescription for a quantum computer was set out by Deutsch [25, 26]. According to this prescription, a quantum computer is a set of n qubits in which the following operations are experimentally feasible:

1. Each qubit can be prepared in some known state $|0\rangle$.
2. Each qubit can be measured in the basis $|0\rangle, |1\rangle$.
3. A universal quantum gate can be applied at will to any fixed-sized subset of the qubits.
4. The qubits do not evolve other than via the above transformations.

To date, only a handful of physical systems have been shown to satisfy the above criteria. Among the various possibilities explored are systems which stem from fields such as ion trapping, nuclear magnetic resonance (NMR), cavity quantum-electrodynamics (cavity QED) [29, 36, 85], trapped atoms in optical lattices [16] and solid state physics [4, 46]. Of these, the NMR technique has been used to demonstrate the most advanced degree of computation. However, difficulties associated with the state preparation step mean that the number of qubits is limited to about 10.

The ion trap method has also succeeded in demonstrating quantum logic operations. A CNOT gate was successfully demonstrated in 1995 using a single ion [54]. With respect to scalability, it seems to show more promise over the NMR method. For these reasons, only these two schemes will be described in more detail. A short description of the NMR scheme is given in the next section with the ion trap approach described in greater detail in the section following that. Greater emphasis is given to the ion trap approach as it bears more relevance to the work done by our group at ICL. As was mentioned earlier, the long term goal of our group is to investigate the feasibility of the Penning trap as a means to implement QIP. Therefore, it is necessary that the current state of play of experiments involving trapped ions for use in QIP be described before the motivation behind our work can be better understood.

3.7 Quantum Computing Using NMR

The qubits in the NMR method consists of the spin states of a spin-1/2 nucleus which provide a two-level system. The single qubit gate corresponds to single qubit rotations of a spin-1/2 nucleus. This can be effected by applying RF fields as the difference in energy in units of frequency is typically 500MHz. A two-qubit gate requires the interaction between the two qubits. This is readily available in the form of the scalar coupling (J-coupling) between two nuclei in a molecule. It should be noted that the NMR system is a macroscopic sample made out of a liquid. This liquid contains molecules, which in turn contain the nuclei used as qubits. The signal obtained from such a system will therefore be an ensemble average of all the nuclei detected.

One of the criteria for a quantum computer is the ability to prepare the system in the state $|0\rangle$. The most obvious way to obtain a $|0\rangle$ state is to cool the system down to its energetic ground state and choose that as the $|0\rangle$ state. This is possible if the energy separation between the two states is greater than the Boltzmann energy, kT. This unfortunately, does not hold in an NMR system which results in the states being equally populated and thus no signal will be detected as the average signal will be zero. However, deviations from

the ensemble average produce a non zero signal (around 1 part in 10^4). These deviations are most obvious in a molecule containing a single isolated nucleus (which represents a single qubit). This means that it is possible to prepare a single qubit in the $|0\rangle$ state. However, it is not possible to apply this method to more than one qubit or a molecule containing more than one nucleus as the population deviations become even smaller.

This problem in scaling was successfully addressed using two independent methods. The first method involves the application of complex NMR pulses to modify the population of the spin states such that the population pattern corresponding to the desired $|0\rangle$ state is achieved [20, 21]. The second approach involves dividing the macroscopic spin system into a number of different smaller subsystems [34, 77]. As population deviations are more pronounced in smaller subsystems, they can be prepared in the desired starting state. Hence, the collection of spin states can also be prepared in the desired starting state. These two approaches have allowed great progress to be made within NMR quantum computing where the NMR quantum computer has successfully demonstrated the generalised Grover's algorithm [84] and successfully factorised the number 15 using 7 qubits [76] in a demonstration of Shor's algorithm. However, there are still practical difficulties involved in the state preparation step using the two approaches mentioned above. These need to be addressed before more complex computations which require a greater number of qubits can be performed.

Groups currently pursuing NMR quantum computing include: D.G. Cory and T.F. Havel - MIT Nuclear Engineering, N.A. Gershenfeld and I.L. Chuang - MIT Media Lab, E. Knill - Los Alamos National Laboratory (LANL) and Laflamme - Waterloo.

3.8 Quantum Computing Using Trapped Ions

In the trapped ion approach, the qubits are ions confined in an externally applied potential. So far, all the experiments with trapped ions leading towards quantum computing involve the use of Paul traps. A variation of the Paul trap, the linear Paul trap, is widely used as it offers the possibility of storing more than one ion in a string along the trap axis where the time varying electric field is zero. The Coulomb interaction between the ions can then provide a means for entanglement required for QIP. The ions are laser cooled to the ground motional state using Doppler cooling and sideband cooling techniques described in Chap. 2. To increase storage times and to reduce the heating rate, the ions are confined in an ultra-high-vacuum environment. The quantum gates are effected by applying laser pulses of well defined frequency and intensity which are turned on for a specific length of time. As the ions are confined in a well under-

stood potential and manipulated using laser beams which are well controlled, decoherence effects are relatively low compared to other systems.

Other advantages of this system include the ability to prepare the ion in a known quantum state. The most obvious route would be to laser cool the ion to the ground state of motion to obtain the state $|0\rangle$. Since the ion starts off in a known state, the evolution of the quantum state can be performed with a high degree of certainty. Another advantage of the trapped ion approach is the high state detection efficiency through the use of the quantum jump technique (see Sec. 5.5 of Chap. 5 for an explanation of quantum jumps) which can be as high as 99%. This is in contrast to the experiments using photons as qubits where efficiencies of only $\approx 10\%$ are obtained [14].

Experimental groups that are currently exploring the possibility of quantum computing with trapped ions include: IBM-Almaden, MPQ-Garching, NIST-Boulder, Innsbruck, LANL-New Mexico, Oxford, NPL-Teddington and Hamburg.

3.8.1 Choice of Ions

The choice of ions is mainly determined by two factors. The first involves the internal state of the ion. It should have a two level system (for the logic states $|0\rangle$ and $|1\rangle$) that is free from decoherence due to spontaneous decay and a strong transition for optical cooling and detection. The second factor to be considered is the laser wavelengths required to address the above mentioned transitions. These two factors combined limit the choice of ions to the single positively charged alkaline earths. Examples of ions used are Sr^+, Mg^+, Ca^+, Ba^+ and Be^+.

The two-level system can be provided by either a long-lived metastable state or two hyperfine levels of the ground state. An example of the former is found in $^{40}Ca^+$ while the latter can be found in $^9Be^+$.

The two hyperfine levels in $^9Be^+$ are separated by a microwave frequency and can be coupled either by the direct application of microwave radiation or by using a stimulated Raman transition. The Raman approach provides an avenue for entanglement operations to be carried out as it allows the coupling between the ion motion and the qubit states. The disadvantage of this scheme is that the decoherence effects are greater in the form of spontaneous Raman decay from the upper hyperfine state during the application of the Raman pulses.

The qubit transition in $^{40}Ca^+$ is the $4S_{1/2} \rightarrow 3D_{5/2}$ transition with the $3D_{5/2}$ having a lifetime of $\sim$ 1s. The two levels can be coupled by direct application of a laser at 729nm. Since this coupling is a single photon transition, the absolute frequency stability of the 729nm laser has to be very good in order to be able to

address the motional states of the ion. Frequency stabilities better than 1kHz are achievable using frequency stabilising techniques such as the Pound-Drever-Hall method [83]. This involves frequency locking to a high finesse optical cavity which is thermally and acoustically isolated from the environment.

3.8.2 Ion Confinement and Motion

As mentioned earlier, QIP with trapped ions has so far only been investigated in the Paul trap. A detailed description of the Paul trap was given in Sec 2.1.2 of Chap. 2. It was shown that the pseudo-potential is harmonic and the secular motion is quantized into a ladder of energies described by a quantum harmonic oscillator. The ladder of energies is resolved if $\gamma \ll \omega_i$ where γ is the natural linewidth and ω_i is the vibrational frequency of the trapped ion. This allows for the ion to be cooled to the vibrational ground state via sideband cooling.

The vibrational frequency of the trapped ion, ω_i, is determined by the stiffness of the trap. The stiffer the trap, the greater ω_i is. A stiffer trap results in a lower mean vibrational quantum number $\langle n \rangle$ after laser cooling to the Doppler limit is achieved. This means that less sideband cooling cycles are required to reach the vibrational ground state. For example, the Ca^+ experiment at Innsbruck uses a trap with $\omega/2\pi \approx 100 - 180$kHz which gives $\langle n \rangle \approx 50$ after Doppler cooling to about 1mK. In contrast, the Be^+ experiment performed at NIST uses a trap with $\omega/2\pi = 11.2$MHz which gives $\langle n \rangle \approx 1.3$ after Doppler cooling to the same temperature. However, the drawback in using a stiffer trap is that the inter-ion spacing is smaller. This makes the individual addressing of each ion using laser beams (which is required in some of the QIP schemes using trapped ions) more difficult. Also, stiffer traps use smaller electrodes. This exacerbates the problem of patch potentials which can shift the ions away from the position of least micromotion.

Another important parameter to be considered is the dimensionless Lamb-Dicke parameter, η. For a single trapped ion, this is given by

$$\eta = \sqrt{\frac{E_R}{\hbar\omega_i}}, \tag{3.5}$$

where E_R is the recoil energy of an ion after emission of a single photon. The Lamb-Dicke regime is reached when $\eta \ll 1$. A consequence of being within this regime is that a change in vibrational quantum number is unlikely in the event of a spontaneous emission. Physically, this regime can be realised by using a very stiff trap.

For sideband cooling, it is desirable to be in the Lamb-Dicke regime since upon spontaneous emission, the vibrational quantum number is conserved. However, this is not ideal for quantum gate operations for the following reason. The

prescription for ion trap QIP was given by Cirac and Zoller [19]. In their description of ion trap QIP, the two-qubit quantum gate is effected by transferring information between the ion and the "bus" qubit. The "bus" qubit is the quantized COM motion of the collection of ions. This transfer of information requires vibrational-state-changing operations between the ion and the "bus" qubit. The rate at which these operations are performed is called the switching rate and is given as [73]

$$R = \frac{\eta\Omega}{2\pi\sqrt{N}}, \tag{3.6}$$

where η is again the Lamb-Dicke parameter, Ω is the Rabi oscillation frequency for the two levels involved and N is the number of ions. It can be seen that being too far into the Lamb-Dicke regime reduces R. This tradeoff results in the optimum setting being $\eta \approx 1$. In other words, the optimum setting is found with the ion confined on the border of the Lamb-Dicke regime.

3.8.3 The Cirac-Zoller Scheme

The principle of operation behind ion trap QIP was first envisaged by Cirac and Zoller (CZ) in 1995 [19]. Their scheme was based on the fact that any quantum logic operation can be decomposed into two separate operations namely the CNOT operation and the single qubit rotation [69]. Single qubit rotations are effected by a $\pi/2$ Rabi pulse and are relatively simple to implement since much study has gone into the process of Rabi oscillations. However, the CNOT operation, which is a two-qubit quantum gate is more difficult to realise and required the insight of CZ before a method of physically implementing this gate was discovered.

In the CZ scheme, ions are confined in a linear Paul trap. The wavefunction of the ensemble of ions is given as

$$|\psi\rangle = \sum_{x=0}^{2^N-1} c_x|x\rangle, \tag{3.7}$$

where the binary decomposition of $x = \sum_{n=0}^{N-1} x_n 2^n$. Here, N is the total number of ions and n denotes a particular ion. Parallel computation is made possible by applying a $(controlled)^n$ NOT gate onto the ensemble of ions. However, no physical implementation which directly applies the $(controlled)^n$ NOT operation has yet been discovered. This operation can be achieved by implementing a finite number of CNOT operations between pairs of individual ions.

Confinement in the linear Paul trap provides an additional qubit through the centre of mass (COM) vibrational mode. This quantised vibration is an oscilla-

tion of all the ions in phase along the trap axis. Since information stored in the COM mode is accessible by each ion, this vibrational mode acts as a "bus" qubit. Before the COM can be used, it must first be cooled to its vibrational ground state. The two-qubit gate between two ions is achieved by firstly mapping the information of the first ion qubit onto the "bus" qubit. Then, by performing a two-qubit operation between the second ion qubit and the "bus" qubit, we have in effect implemented a two-qubit gate between the two ion qubits. This scheme requires the individual addressing of the ions as well as an auxiliary electronic level to facilitate some of the operations. The two-qubit gate described by CZ is essentially a phase gate where the phase of the wavefunction of the system acquires a change of sign only if the two ions are initially in the $|1\rangle$ state. This is also known as a controlled-rotation gate or CROT. The truth table for this gate is shown in Eq. 3.8. Physically, this can be realised by applying a 2π pulse onto the ions. The CNOT gate can then be obtained by combining the CROT gate with single qubit rotations. The final output can in principle be read out with unit efficiency by observing the fluorescence from a strong transition coupled to only one of the qubit states. Fluorescence will be observed only if this coupled qubit state is occupied. The absence of fluorescence indicates that the qubit state is in the other basis state.

$$\begin{aligned} |0\downarrow\rangle &\rightarrow |0\downarrow\rangle \\ |0\uparrow\rangle &\rightarrow |0\uparrow\rangle \\ |1\downarrow\rangle &\rightarrow |1\downarrow\rangle \\ |1\uparrow\rangle &\rightarrow -|1\uparrow\rangle. \end{aligned} \tag{3.8}$$

Following the publication of the CZ scheme, the CNOT gate was experimentally demonstrated by [54]. Here, the two qubits are in the form of the internal and vibrational state of the a single trapped ion. The target qubit is formed by the two $S_{1/2}$ hyperfine ground states of a single Be^+ ion, which we can denote as $|\downarrow\rangle$ and $|\uparrow\rangle$. They are separated in frequency by ω_0. The control qubit is formed by the ground and first excited vibrational states denoted by $|0\rangle$ and $|1\rangle$ respectively and have a frequency separation of ω_i. The auxiliary state, $|\text{aux}\rangle$ required in this scheme is provided by another $S_{1/2}$ hyperfine ground state. The frequency difference between the auxiliary level and the upper hyperfine state $|\uparrow\rangle$ is ω_{aux}. The relevant energy levels are shown in Fig 3.1. The four basis states are then given as $|0\downarrow\rangle$, $|1\downarrow\rangle$, $|0\uparrow\rangle$ and $|1\uparrow\rangle$.

To realise a CNOT gate, a sequence of three laser pulses of the following form are applied:

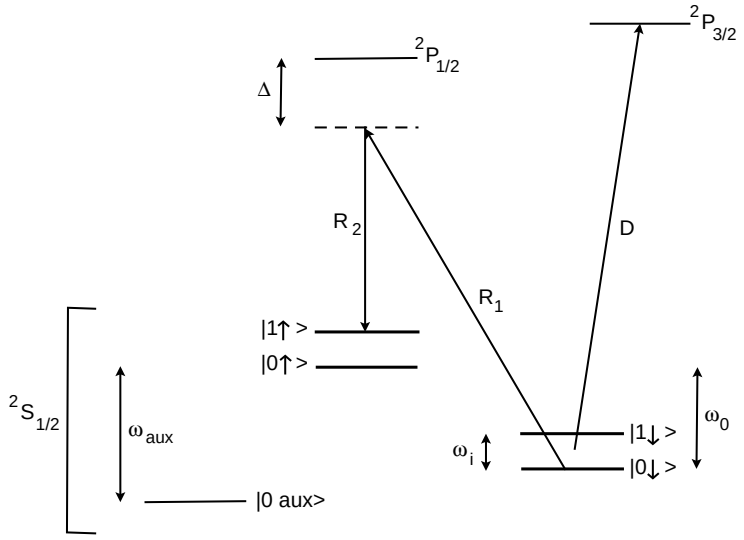

Figure 3.1: Energy level scheme of Be^+ used for implementing the CNOT gate.

(i) A $\pi/2$ pulse is applied at the carrier transition ω_0.

(ii) A 2π pulse is applied at frequency $\omega_{aux}+\omega_i$ which drives the blue sideband transition between the $|1\uparrow\rangle$ and the $|0\ \text{aux}\rangle$ level.

(iii) A $\pi/2$ pulse is applied at the carrier transition with a π phase shift relative to i).

Step (ii) only has an effect if there is population in the $|1\uparrow\rangle$ state. If this is the case, the corresponding evolution will take place: $|1\uparrow\rangle \rightarrow |0\ \text{aux}\rangle \rightarrow -|1\uparrow\rangle$. In other words, the state $|1\uparrow\rangle$ acquires a sign change. Steps (i) and (iii) cause the internal state to undergo +1/4 and -1/4 of a complete Rabi oscillation while conserving the vibrational quantum number. It can be seen that if there is no population in the $|1\uparrow\rangle$ state, or if step ii) has no effect, then the two $\pi/2$ pulses in steps (i) and (iii) will cancel out leaving the ion back in its original state. However, if the state $|1\uparrow\rangle$ is occupied, then the two $\pi/2$ pulses will add constructively (since step (ii) causes the state $|1\uparrow\rangle$ to acquire a sign change) causing the internal state of the target qubit to "flip". The truth table for the CNOT gate is then obtained as follows:

$$\begin{aligned} |0\downarrow\rangle &\rightarrow |0\downarrow\rangle \\ |0\uparrow\rangle &\rightarrow |0\uparrow\rangle \end{aligned}$$

$$
\begin{aligned}
|1\downarrow\rangle &\rightarrow |1\uparrow\rangle \\
|1\uparrow\rangle &\rightarrow |1\downarrow\rangle.
\end{aligned} \tag{3.9}
$$

The state detection is performed by driving the transition $|\downarrow\rangle \rightarrow {}^2P_{3/2}$ $|F = 3, m_F = 3\rangle$ and observing the fluorescence from the ion.

The QIP scheme above requires certain conditions to be fulfilled before it can be carried out. The conditions required are i) the ions are cooled to their vibrational ground state, ii) individual addressing of the ions with laser beams and iii) the presence of an auxiliary state. As these conditions are non-trivial, different QIP schemes have been proposed which have less constraints. The most promising scheme is that proposed by Molmer and Sorensen [53, 70, 71] in 1999 and will be described in more detail in the following section.

3.8.4 The Mølmer and Sørensen (MS) Scheme

The MS entanglement scheme has several advantages over the CZ scheme. The method of confinement of the ions is the same as that used in the CZ scheme. The aim of the scheme is to produce a state of the form

$$
|\psi\rangle = \frac{1}{\sqrt{2}}(|\uparrow\uparrow ... \uparrow\rangle + \ i^{N+1}|\downarrow\downarrow ... \downarrow\rangle), \tag{3.10}
$$

where $\uparrow$ is the excited internal state and $\downarrow$ is the ground internal state. If N is the number of ions, then there will be N terms in $|\uparrow\uparrow ... \uparrow\rangle$ and N terms in $|\downarrow\downarrow ... \downarrow\rangle$.

It was shown that this can be achieved without laser cooling to the ground vibrational state. This is possible because the entanglement scheme used here does not rely on coupling directly onto the vibrational modes which also makes this system less susceptible to motional heating. The requirement of having to be able to individually address each ion is also relaxed. Using this scheme, the ions that are intended for entanglement are illuminated with laser beams at two different frequencies. This removes the need of having to discriminate the ions spatially if all the ions present are to be entangled. However, if only a fraction of the total number of ions are to be entangled, then the laser beams must be able address only those ions. Another advantange of this scheme is that it is not necessary to have an auxiliary state. It does however, require the ions to be cooled well into the Lamb-Dicke regime.

To illustrate the MS scheme, the method for entangling two ions is described. Since the ions are confined in a linear Paul trap, the energy levels consists of a ladder of equidistant motional levels separated by ω_i. See Fig. 3.2. The levels are labelled $|Jn\rangle$ and $|JJn\rangle$ where J is the internal energy level and n is the vibrational quantum number. The ions are illuminated with $\pi/2$ laser pulses at

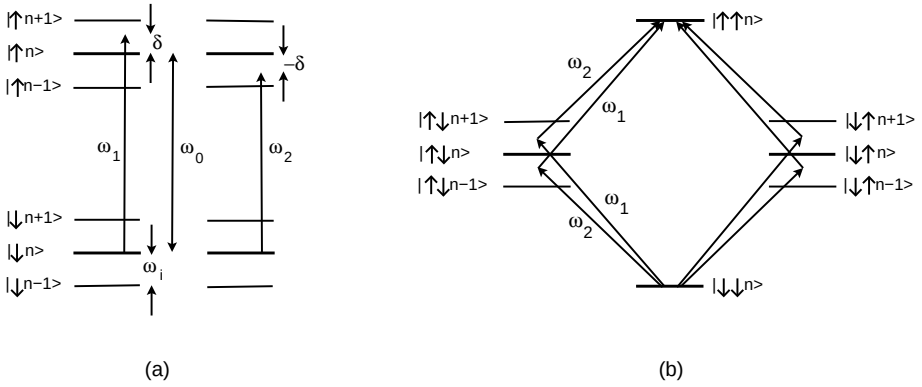

Figure 3.2: (a)Energy levels of two ions and laser detunings used to address the ions. Taken from [70]. (b)The collective vibrational modes of the ions and the four transition paths between $|\downarrow\downarrow n\rangle$ and $|\uparrow\uparrow n\rangle$ are shown. Taken from [53].

frequencies of ω_1 and ω_2 where $\omega_1 = \omega_0 + \delta$ and $\omega_2 = \omega_0 - \delta$. ω_0 is the carrier transition frequency. δ is chosen so that it is slightly detuned away from the motional frequency. This results in the motional states being only negligibly populated. The different transition paths from the $|\uparrow\uparrow\rangle$ level to the $|\downarrow\downarrow\rangle$ level are shown in Fig. 3.2(b). Interference between the different paths results in the effective Rabi frequency of the two photon transition having no dependence on the vibrational quantum number, n [53].

The MS scheme has been experimentally demonstrated by [64] using Be^+ ions confined in a miniature linear Paul trap. Here, two and four ions have been successfully entangled using the stretch mode to mediate between the two levels. If P_j is the probability that j ions are in state $|0\rangle$ then for the two ion case, $P_0 + P_2 \approx 0.95$ and for the four ion case, $P_0 + P_4 \approx 0.70$.

3.8.5 Decoherence

The problem of decoherence was briefly and generally described earlier in this chapter in Sec. 3.5. Decoherence can be loosely defined as any effect that limits the fidelity of a logic operation. The fidelity is given by the probability for a logic operation to succeed. Decoherence in an ion trap QIP can be divided into three categories i) decoherence of the ion internal levels, ii) decoherence of the ion motion and iii) decoherence caused by the imperfect application of fields required for quantum computation.

Internal State Decoherence

The coherence of the internal state is fundamentally limited by the lifetime of the state. The lifetime can be made extremely long by choosing to use two hyperfine ground states as the two internal levels (e.g. Be^+). Ions with metastable levels are also appropriate where lifetimes of greater than 1s are available (e.g. Ca^+, which has a lifetime of $\sim$ 1s) [18].

Other sources of internal state decoherence are fluctuations in the magnetic and electric field with the former being the more pronounced of the two. The strength of the magnetic field defines the energy separation between the two internal levels (Zeeman splitting). Hence, decoherence arises when the magnetic field strength is not constant. Electric field fluctuations are less important because the electric field strength is relatively small at the position of the ions. The Stark shift induced by this weak electric field is many orders of magnitude smaller than the Zeeman shifts caused by fluctuations in the magnetic field.

Motional State Decoherence

One source of motional decoherence is from fluctuating trap parameters. Changes in these parameters cause the vibrational frequency of the trap to change and can lead to phase fluctuations during a series of logic operations. The relationship between the frequency fluctuations and the phase fluctuations is given in [82].

In the CZ scheme, the COM mode is initially required to be cooled to the ground vibrational state. If the other normal vibrational modes of the trap are not cooled to the ground state, energy can be transferred from these modes to the COM mode causing heating. Even if the other modes are cooled to the ground state, energy can still be transferred between the COM mode and the other normal modes which leads to decoherence.

Another source of motional decoherence is collisions with residual background gas in the vacuum system. This can take two forms. The first is inelastic collisions, which change the internal state of the ion or even change the species of the ion. The second is elastic collisions, which only change the motional state of the ion. Both cases are a source of decoherence although the latter causes the greater concern.

Induced Decoherence

The QIP schemes with trapped ions require the application of laser fields to effect quantum logic operations. Decoherence effects that arise from the imperfect application of these fields are catagorised as induced decoherence. For example, a coherent superposition of two basis states is achieved by applying a $\pi/2$ Rabi

pulse. In order to effect this transformation accurately, the laser detuning, intensity and pulse duration must be well controlled. Also, since the CZ scheme requires the individual addressing of the ions, laser beam positioning becomes important. Imprecise control of these parameters will lead to decoherence.

3.8.6 Experimental Studies of Decoherence

Experimental studies of decoherence of Ca^+ ions in a Paul trap have been performed by the group at Innsbruck [61]. Here, a measure of the coherence time is obtained by inducing Rabi oscillations between the $4S_{1/2}(m = +1/2)$ and the $3D_{5/2}(m = +5/2)$ states. It was found that a fringe contrast above 0.5 was observed for more than 20 oscillations. This implies that several gate operations could be performed before decoherence effects become too severe. This group also measured the motional heating rate to be ~ 1 phonon in 190ms.

Studies of decoherence have also been performed by the group at NIST [75]. The heating rates were investigated for different varieties of traps. Although the results were not conclusive, they have identified a possible source of heating to be fluctuating patch potentials on the electrodes. They have found that the heating rate is dependent on the trap size where the heating rate scales as d^{-4}, with d representing the trap dimension.

3.8.7 Scalability

So far the linear Paul trap appears to be the most promising candidate for large scale QIP. This is due to its ability to store large numbers of ions along the trap axis while still maintaining the possibility of entanglement between the ion qubits through coupling provided by the COM motion. However, it has been shown that performing large scale QIP in a single trap presents severe technical difficulties [82, 41, 31]. This has led to the development of a different ion trap design by the group at NIST which could potentially present less technical and theoretical obstacles [47].

The trap proposed by the group at NIST consists of a series of interconnected ion traps (see Fig. 3.3). Ions storing quantum information are held in the memory region. To implement a quantum operation, the relevant ions from the memory regions are brought together into the interaction region. Here, they are placed close enough to one another such that entanglement can take place through the Coulomb coupling. Once the operation is complete, the ions are separated and moved back into the memory region before the next set of ions are manipulated.

Initial tests by the group at NIST have shown that it is possible to transport a single ion between two interconnected traps while maintaining internal state

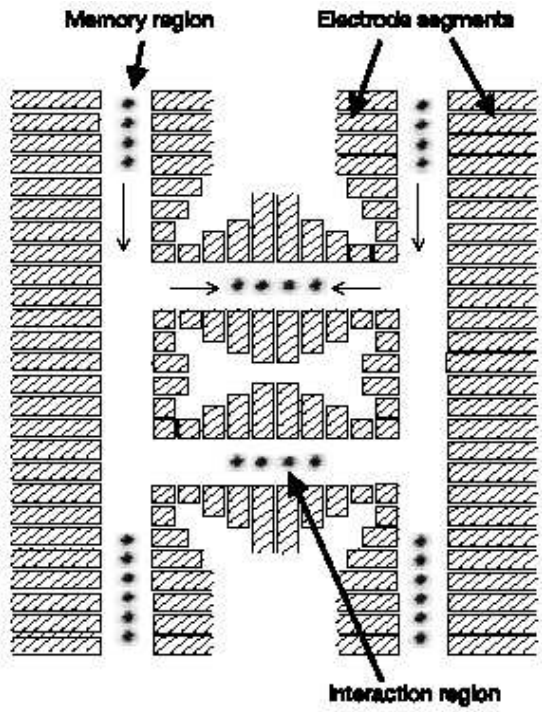

Figure 3.3: Diagram of interconnected ion traps proposed for large scale ion trap QIP. The arrows show how the ions are to be moved around to the different trapping regions. Taken from [47].

coherence [62]. It has also been demonstrated that the transfer of the ion resulted in negligible motional heating. The separation of two ions in a common trap into two distinct traps has also been performed. Here, the motional heating rate was more significant at ~ 150 quanta in 10ms.

3.9 The Penning trap QIP

Using a Penning trap for QIP may have several advantages over the more usual choice of the linear Paul trap. Firstly, as the Penning trap only uses static fields for trapping, the potential problems associated with r.f. heating are non existent. Also, Penning traps can be made larger whilst still maintaining high trap frequencies. This is advantageous since it has been shown that heating rates scale as d^{-4} where d is the characteristic trap size [75]. However, before the Penning trap can become a serious candidate for implementing QIP several obstacles need to be overcome.

One of the most apparent problems is due to the large magnetic field used to confine the ions which causes the energy levels to Zeeman split. This complicates laser cooling where additional lasers are required to prevent optical pumping into dark states. The magnetic field also causes the ions to rotate around the centre of the trap at the magnetron frequency. As was mentioned in Sec 2.4, cooling this degree of motion requires the laser cooling beam to be spatially offset from the centre of the ion orbit such that there is an intensity gradient across the ion orbit. This means that the size of the ion orbit is limited to a size similar to the laser beam waist. This is a significant problem for QIP applications as one of the requirements of the QIP with trapped ions scheme is that the ions need to be cooled so that they are on the border of the Lamb-Dicke regime. However, recently, a technique called axialisation has been demonstrated which overcomes this problem by greatly improving the radial localisation of single laser cooled ions in the Penning trap [59].

Another significant obstacle in the way of realising Penning trap QIP is the problem of scaling. It is possible to store a string of ions along the magnetic field in a Penning trap. Here, one of the common axial vibrational modes can be used as the "bus" qubit which provides a means for entanglement. To trap the ions in a line along the magnetic field, the radial confinement needs to be made stronger than the axial. This can be done by reducing the static potential and increasing the magnitude of the magnetic field. Since there is a practical limit to the strength of the magnetic field achievable, there is also a limit to the number of ions that can be stored along the magnetic field. This turns out to be around two or three ions depending of the ion species and trap size. Although it is easier to store a longer string of ions in a linear r.f. trap, this cannot

be easily used for QIP since the proliferation of modes makes them difficult to discriminate. Despite the obvious limitation in the Penning trap scheme, it is still a useful system for QIP applications to be studied.

For larger scale QIP, a different approach is required. One possibility would be to have an array of individual traps aligned along the magnetic field. The idea would then be to shuttle the ions from one trap to the adjacent one by the application of suitable potentials. The two ions within a common trap can interact with each other before being separated again. The operating principle here is similar to that described by the group at NIST for implementing large-scale r.f. trap QIP (see Sec. 3.8.7). For this to be possible, a different trap design from the conventional hyperbolic electrode design is required. One possibility would be the cylindrical Penning trap where the endcap electrodes are "open" which should allow for ions to be transported along the trap axis. The drawback here is that only ions which are adjacent to each other can easily interact. If we desire the two ions which are farthest apart to interact with each other, we would have to move the relevant ions across several traps before they are held together in a common trap. This is not only time consuming but makes the system more susceptible to decoherence since a process that involves a greater number of experimental steps is more prone to errors. The ideal situation would be to freely select any pair of ions and shuttle them to a common trap where they can interact. However, this would require the ability to transport the ion in a direction perpendicular to the magnetic field which at the moment represents a significantly difficult experimental task. A completely different approach may be required to circumvent this problem if larger scale QIP with Penning traps is to be realised.

Although several non-trivial experimental obstacles have been identified, there are no fundamental issues that would make the idea of a Penning trap QIP an impossibility. This combined with the fact that the Penning trap system may have several potential advantages over other systems means that it is an option that is still worth pursuing.

Chapter 4

Experimental Setup (General Features)

Although the experiments described in this thesis employ three distinct modes of trap operation - the Paul trap, combined trap and the Penning trap - there are many features common to all modes. The common experimental features, which are the trap design, vacuum housing, detection system, laser systems and the wavelength determining setup are described in this chapter. The method of electronic detection and its results are included in this chapter. Although this is not part of the setup used with the three different modes of trap operation, it was initially used as a means of determining the presence of ions in the Paul and Penning traps before Doppler cooling was attempted. The setup specific to each mode of trap operation is described in the relevant chapters.

4.1 The Ion Trap Design

4.1.1 The Electrode Structure

The ion trap used in the experiments described in this thesis consists of three electrodes; a ring electrode and two endcap electrodes. As was shown in Sec. 2.1.1 of Chap. 2, the quadrupole trapping field of the form given in Eq. 2.2 requires the surfaces of the electrodes to be hyperboloids of revolution. Constructing such electrodes is expensive as it requires sophisticated machinery. However, it has been shown [5] that electrodes with circular geometry will produce a trapping field that is very near to that given by Eq. 2.2 with only a deviation of the resulting potential from the ideal potential of $\sim 1\%$ within 0.5mm around the trap centre.

The electrodes are machined from oxygen-free-high-conductivity (OFHC)

grade copper. The relative position of the ring and two endcaps is shown in Fig. 4.1(a). The ring has an inner radius, $r_0 = 5$mm and the endcaps are separated from each other by $2z_0 = 7$mm, where z_0 is the distance from one endcap to the centre of the trap. The ring and the endcaps are held together at the appropriate distance apart by ceramic spacers. The ring is then mounted onto the central pin of an eleven pin feedthrough which, apart from supporting the whole trap, also provides the electrical connection to the ring. The two endcaps are also electrically connected to two separate pins on the feedthrough.

To facilitate laser access into the trap as well as the detection of fluorescence from the centre of the trap, holes are drilled into the ring electrode as shown in Fig. 4.1(b). Fluorescence from the centre of the trap is collected using a lens that is held at a fixed distance from the centre of the trap by a cylindrical holder which is screwed onto the ring. A blind hole is made on the opposite side of the ring electrode so that the detector looks into a void. This reduces the amount of back reflected light entering the detector. Apertures are placed at the front and back of the input and output holes respectively to block stray light from entering the trap (see Fig. 4.1(b)). Holes are also drilled into the endcap electrodes to make room for an electron source. The electron source needs to be placed there because the electrons can only move along the magnetic field lines which run parallel to the trap axis. The magnetic field guides the electrons into the centre of the trap and is present during the loading procedure of the Paul, combined and Penning trap modes. The atomic source is placed at the space between the ring and the endcap electrode as shown in Fig. 4.1(a).

4.1.2 The Ion Source

The calcium ions are created by crossing an atomic beam with an electron beam. The atomic beam is produced by heating a calcium "oven". The oven consists of a tantalum tube (0.08mm wall thickness) stuffed with pieces of crushed calcium. One end of the tube is crimped shut while the other is crimped around a pin to leave a hole for the atomic beam to go through (see Fig. 4.2). The tube has an inner diameter of 1mm and a length of 10mm. An appropriate length of tantalum wire with a diameter of 0.25mm is then spot welded onto the tube. This provides a means to heat the tube by passing current through the wire.

The electron beam is created by heating a filament to the point at which it produces thermionic electrons. The filament is made by wrapping a 0.25mm diameter tungsten wire around a 1-2mm diameter cylinder. The cylinder is then removed leaving approximately eight turns stretched out to a length of $\sim$ 1cm. Two filaments were placed around the trap, behind the holes in the endcap electrodes so that the electrons are emitted along the trap axis.

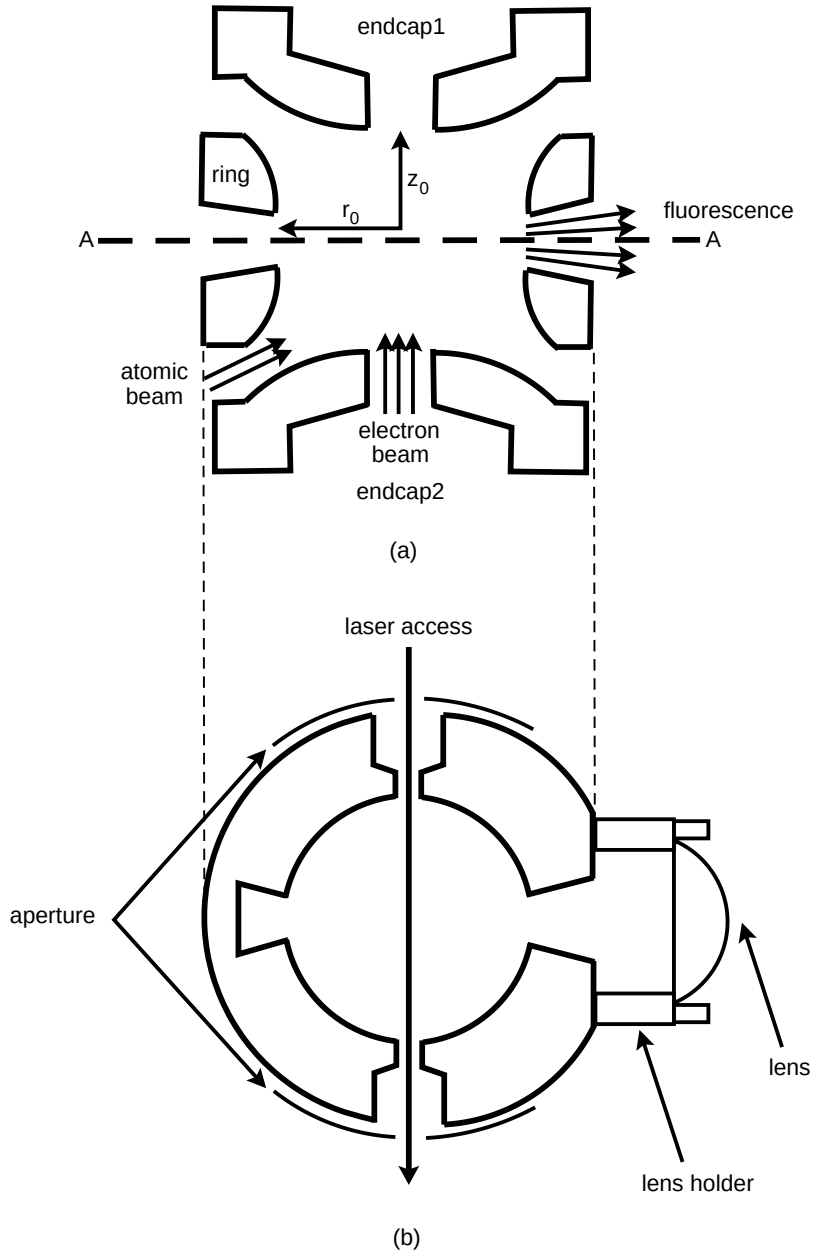

Figure 4.1: (a)Relative position of the ring electrode with respect to the endcap electrodes. (b)Cross section AA of the ring electrode showing position of access holes.

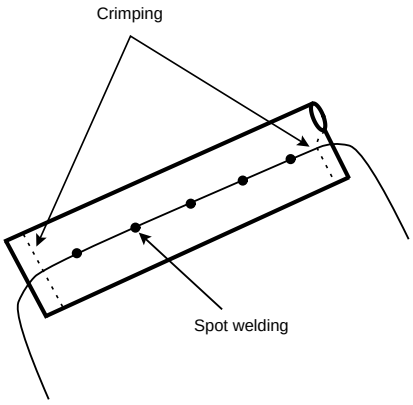

Figure 4.2: Schematic showing the oven design.

The filaments and oven are mounted onto the pins of the electrical feedthrough with barrel connectors. Ceramic tubes are used as sheaths around the legs of the oven and filament to avoid excess material being emitted when they are heated as well as providing them with more rigidity and electrically insulating them from contact with other metal parts. The oven and filament are heated by passing a current through them. Typical operating parameters for the oven and filament are shown in Table 4.1.

4.2 The Vacuum System

The operation of the ion trap requires it to be under ultra-high-vacuum (UHV) conditions. The trap is placed in 38mm diameter stainless steel tubing that has three quartz windows attached to it. The entrance and observation windows are 90° windows while the exit window is Brewster angled. A schematic diagram of the vacuum housing is shown in Fig. 4.3. The base pressure of $\approx 2\times10^{-10}$ mbar is achieved by baking the entire system (see next paragraph for procedure) and is maintained by an ion pump (Meca 2000). The pressure is monitored using an ionisation gauge. There are also two valves present in the vacuum housing, one is a leak valve which allows for the possibility of buffer gas cooling and the other is used to connect to the pumping station.

	Current/A	Time/s
Oven	2.00	32
Filament	5.00	12

Table 4.1: Typical operating parameters for the oven and filament.

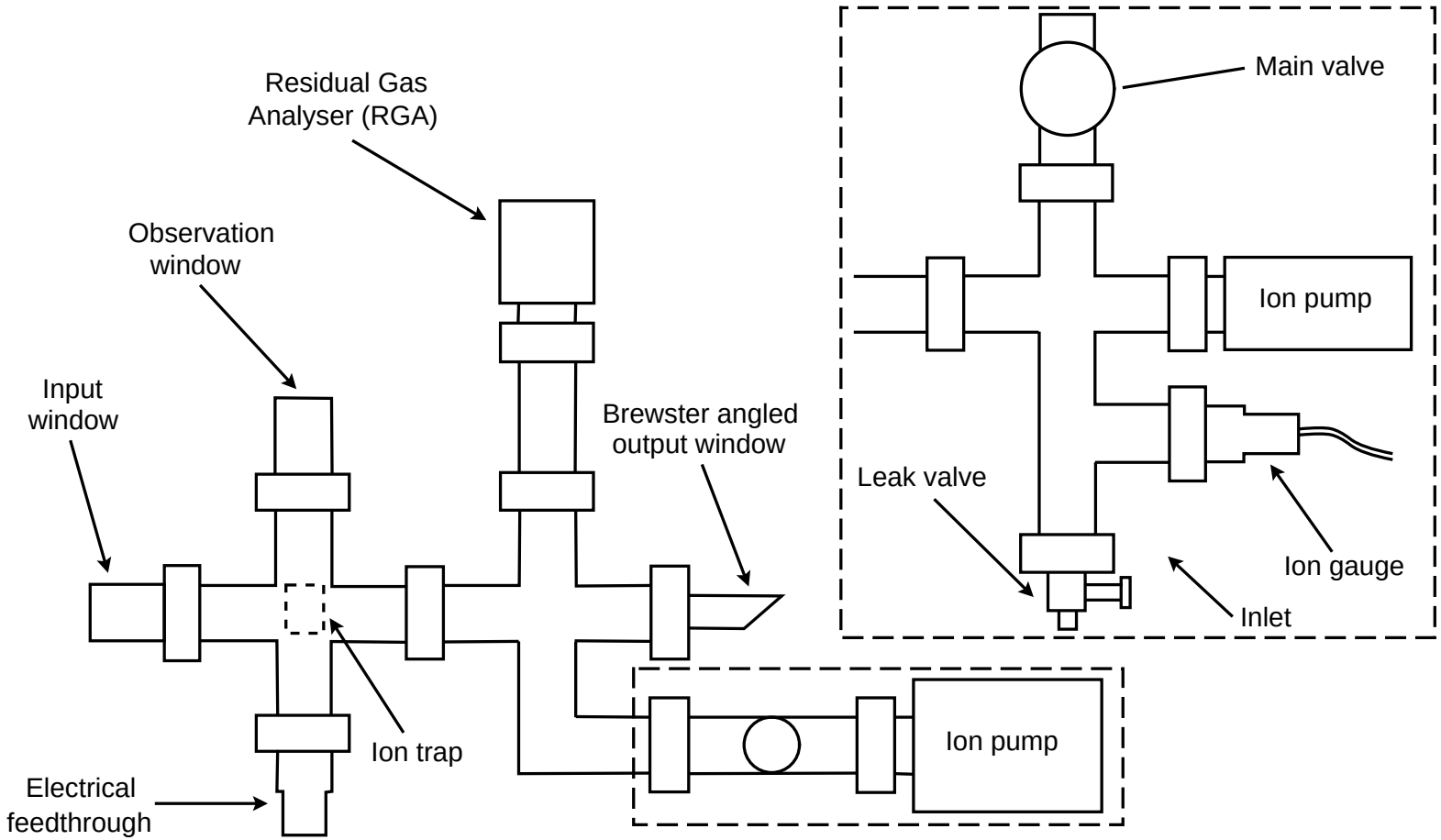

Figure 4.3: Diagram showing vacuum tubing used to enclose the trap. The main diagram is as seen from the side. The parts within the dotted section are re-drawn as seen from the top.

To achieve the background pressure mentioned above, the trap is evacuated using a pump system consisting of a turbomolecular pump whose backing line is connected to a rotary vane pump. The vacuum chamber housing the trap is connected directly to the turbomolecular pump. The turbomolecular pump takes several minutes to reach its maximum rotational frequency. During this time the rotary vane pump lowers the background pressure to $\approx 10^{-3}$mbar. This pressure is monitored using a Pirani gauge situated in the backing line of the rotary vane pump.

After running the pumps for two hours, the ion gauge is turned on and should read a pressure of $\approx 10^{-5}$ mbar. The pumps are left on for a further twenty four hours which should reduce the pressure to $\approx 10^{-7}$mbar before the bakeout stage begins. For the bakeout, an aluminium box is used to enclose the vacuum housing. Two fin heaters and several thermocouples are placed inside this box. The windows are wrapped with aluminium foil to produce a more even heating around them. The trap's ovens and filaments are connected to power supplies so that they can be turned on near the end of the bakeout procedure. It was found that wrapping the outer surface of the aluminium box with aluminium foil increases the final bakeout temperature by $\approx 10\%$. The output from the ionisation gauge and thermocouples are monitored on a chart recorder.

The heaters are connected to variable power supplies. This allows for control over the final temperature as well as its rate of increase. The heaters are also connected to the ionisation gauge controller via a relay which shuts down the heaters when the pressure exceeds 10^{-5}mbar.

For the first twenty four hours the temperature is set to $\approx 100°$C. The heaters are gradually turned up over the next twenty four hours until the final temperature of $\approx 200°$C is reached. During that period, the pressure oscillates around 10^{-5}mbar as the heaters are turned off and on by the relay whenever the pressure overshoots the set point. Eventually the final temperature is reached and the pressure drops. After about five days, the pressure should be of the order of $\approx 10^{-7}$mbar and should stay almost constant. At this point, the heaters are turned off and the oven and filaments are fired for several minutes at currents below their typical operating parameters to allow for degassing. For the same reason, the ionisation pump is fired for a short period of time.

The system is allowed to cool with the turbomolecular pump still left running. Once the pressure reaches 5×10^{-8}mbar or lower the ionisation pump is turned on. As the pressure continues to drop below 5×10^{-9} mbar, the turbomolecular pump is valved off. If there are no leaks in the vacuum housing, the pressure should continue to drop below 10^{-9} mbar over the next one or two days.

4.3 Detection System

A by-product of Doppler cooling is the radiation emitted by the ions as they cycle through the cooling transition. The amount of fluorescence produced is an indication of the efficiency of the laser cooling as well as the number of ions present. It is therefore sensible to detect the ions by the laser induced fluorescence. The detection system consists of a lens system, photomultiplier tube (PMT) and data acquisition electronics and software. They are discussed in more detail in the following section.

4.3.1 Lens System

The lens system consists of two plano-convex quartz lenses; the first collects the fluorescence from the centre of the trap and collimates it and the second focuses it onto the photocathode of the PMT (see Fig. 4.4). The first lens (diameter = 28mm, f = 35.1mm for light of wavelength 280nm) is held at a distance of 28.5mm from the trap centre by a cylindrical holder inside the vacuum housing as described before in Section 4.1.1. This distance, instead of the focal length, is used because it was found from computer simulations to give the least spherical abberations when used with a second lens placed at a specific distance from the trap centre [5]. Reducing the spherical abberations increases the sharpness of the image and consequently the amount of fluorescence collected.

The setup described above is optimal for detecting fluorescence from Mg^+ ions at 280nm but not for the fluorescence of Ca^+ ions at 397nm because of chromatic abberations. The difference in the refractive index due to the different wavelengths leads to a difference of $\approx 14\%$ in the focal length with the latter increasing with wavelength. This results in the image-lens distance being shorter than the focal length of the lens when imaging Ca^+ ions which leads to the fluorescence no longer being as well collimated after the first lens. However, it was found that there was no change in the amount of fluorescence detected when the second lens was placed either closer or farther away from the first lens, indicating that the collimation was not a problem and hence no changes have been made to the lens system.

The second lens (diameter = 38mm, f = 46.8mm) is placed outside the vacuum housing on a mount built onto an x-y-z translation stage. The initial position of the second lens is found as follows. The trap is illuminated using a desk lamp pointing in from the entrance window. By looking into the trap through the two lenses, an image of the top of the ring can be seen on a plane above the second lens. The position of the second lens is then adjusted such that an image is formed at the position of the PMT cathode and on the same plane. Although this is the correct position for imaging the top of the ring and

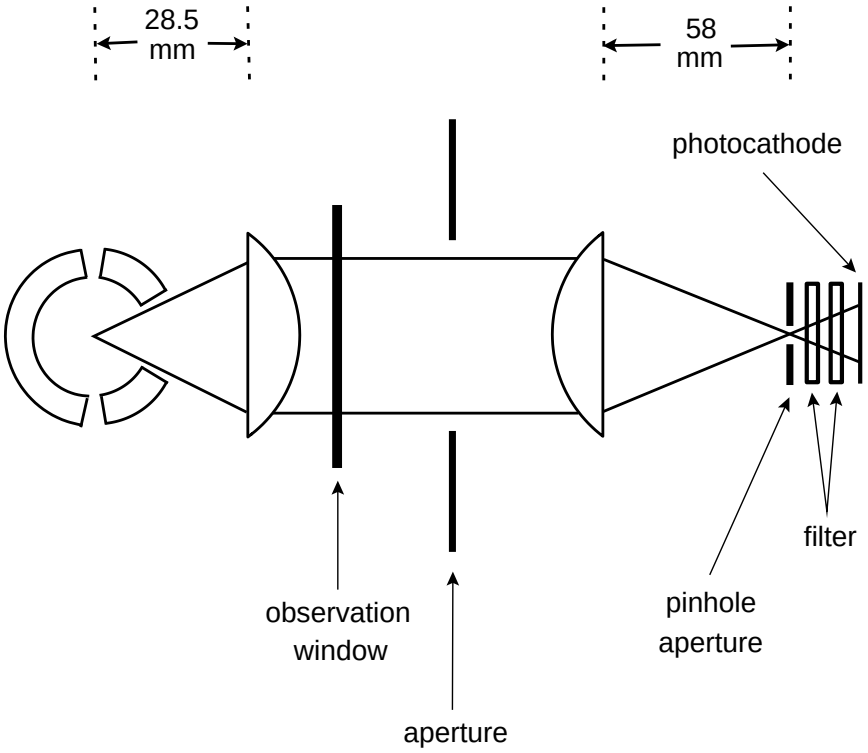

Figure 4.4: The lens system used for the detection of ion fluorescence.

not the centre of the trap and light of visible wavelength is observed instead of light at 397nm, it is still close enough for some fluorescence from the ions to be detected using the PMT. The initial signal can then be optimised by moving the second lens along its three degrees of freedom until a maximum signal is obtained.

The number of photons expected to be observed from a single Ca^+ ion is of the order of 10,000 counts per second (a calculation to obtain this value is given in the next section). In order to observe such low signal levels, steps have been taken to reduce the background level. Two filters have been placed just before the input window of the PMT. One of them is a band-pass filter (395GB25, Comar) which has a transmission of $\approx 80\%$ at 397nm. The second is a low-pass filter (435IK25, Comar) which has a transmission of $\approx 70\%$ at 397nm. A pinhole aperture of ≈ 0.5mm diameter is placed before the filters and at the focus of the second lens. A second aperture is placed in the collimated arm of the fluorescence path which serves to block out scattered light. The fluorescence path from the observation window to the PMT is enclosed with black cardboard and a black cloth is draped over the whole setup to further reduce stray light

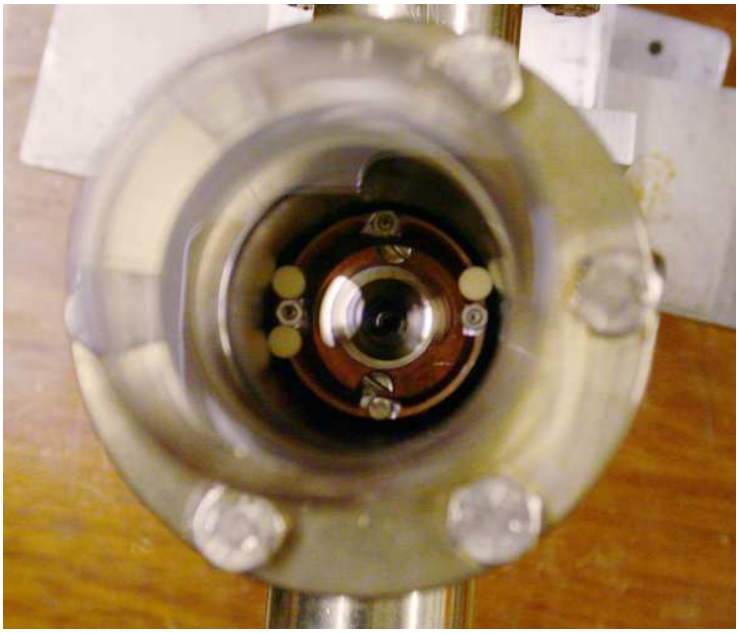

Figure 4.5: Picture of the trap showing magnesium coating formed on the lens above the trap. There are two patches of coatings, with the one on the left being a thicker coating that the one on the right.

from entering the PMT. The PMT is placed inside a mu-metal shield which protects it from stray magnetic fields and radiofrequency noise. With all these steps taken, the background count rate is of the order of 100-200 counts per second with no laser light present which is in agreement with the quoted dark count rate of the PMT.

4.3.2 Detection Efficiency

The detection efficiency of the detection system is dependent on (i) the solid angle of the lens, (ii) the losses due to reflections off the surfaces of the two lenses and observation window (iii) the losses at the pin hole aperture, (iv) the transmission of the filters and (v) the quantum efficiency of the PMT for light at 397nm.

The solid angle subtended by the lens inside the trap depends on the useful area of the lens and the distance of this lens from the ions. Since the useful area of the lens has a radius of 9mm and the distance from the ions is 28mm, the solid angle subtended is given by

$$\Omega = \frac{\pi \times 9^2}{28.5^2} = 0.313\text{sterad.} \tag{4.1}$$

If we assume that the amount of scattered light from the ions is equal in all directions, then the fraction of light collected by this lens is given by

$$\alpha = \frac{0.313}{4\pi} \approx 0.025. \tag{4.2}$$

The losses due to reflections off the surfaces of the observation window and the two lenses can be calculated as follows. It is expected that up to 4% of light is lost at each quartz/air interface except the last lens which is anti-reflection coated for light 280nm. This results in losses at each surface to be $\approx 50\%$ for light at 397nm. This gives a transmission coefficient at the surfaces, $T_{surfaces} = 0.96^4 \times 0.50^2$. It is estimated that the pin hole aperture reduces the amount of light entering the cathode by $\approx 50\%$ due to spherical aberrations that cause the fluorescence to not be completely focused at the aperture. Hence $T_{aperture} = 0.5$. The filters have a combined transmission coefficient, $T_{filters} = 0.8 \times 0.7 = 0.56$. It was also discovered that a magnesium coating was formed on one of the surfaces of the first lens. A picture of this coating taken using a digital camera is shown in Fig. 4.5. It can be estimated that $\approx 50\%$ of the light is lost due to this coating, making $T_{coating} \approx 50\%$. The quantum efficiency of the PMT at 397nm is $\epsilon \approx 0.23$. The the overall efficiency of the detection system is given by

$$\begin{aligned} \xi &= \alpha \times T_{surfaces} \times T_{aperture} \times T_{filters} \times T_{coating} \times \epsilon \\ &= 0.025 \times (0.96^4 \times 0.5^2) \times 0.5 \times 0.56 \times 0.5 \times 0.23 \\ &= 1.7 \times 10^{-4}. \end{aligned} \tag{4.3}$$

4.3.3 Data Acquisition

The PMT is a Thorn EMI phototube Model 9893 QB 350. It operates at a voltage of 2.3kV and produces a dark count of $\approx 100 - 200$ per second. The output signal of the PMT is connected to a discriminator/amplifier and to an ECL to TTL converter before being fed into an EG & G Ortec Multi Channel Scaler (MCS) which is housed inside a Pentium 100 computer. When a photon is detected by the PMT, a single TTL pulse (pulse width = 4ns(FWHM)) is generated. The MCS then counts the number of pulses it receives in each of its 4096 channels. The length of each channel can be set to be between 2μs and 1800s with 2ms being the typical setting. The MCS software then displays this information visually, showing the number of counts at each channel. This data can be saved but only as a .mcs format file. To do anything useful to the .mcs file, it must be first converted into a .dat file. This is done using a program written by a previous PhD. student in the group [40].

4.4 The Lasers

The relevant energy level scheme for Ca^+ in the presence of zero magnetic field is shown in Fig. 4.6(a). It has a strongly allowed dipole transition which is the $4^2S_{1/2} \rightarrow 4^2P_{1/2}$ transition, at a wavelength of 397nm and is used as the Doppler cooling transition. The lifetime of the $4^2P_{1/2}$ level is 7.7ns [44] and it is the decay from this level that is detected as fluorescence. If the ion only decays into the $4^2S_{1/2}$ level, then the scattering rate would be $\approx$ 21MHz. However, the ion can decay into the $3^2D_{3/2}$ level which has a lifetime of 1.08s. This happens once every sixteen cycles which reduces the scattering rate to $\approx$ 16Hz. When this occurs it halts the laser cooling. To avoid this, a repumper laser at 866nm is used to address the $3^2D_{3/2} \rightarrow 4^2P_{1/2}$ transition.

The 397nm laser used for Doppler cooling produces a significant amount of amplified stimulated emission (ASE), enough to affect the amount of fluorescence observed. ASE radiation at 394nm pumps the ion into the $4^2P_{3/2}$ level which decays into the $3^2D_{5/2}$ level and reduces the time spent in the cooling transition. To solve this, a third laser at 854nm is used to couple the $3^2D_{5/2}$ level to the $4^2P_{3/2}$ level.

In the presence of a magnetic field, laser cooling becomes more complicated due to the Zeeman splitting of the levels as shown in Fig. 4.6(b). Two 397nm lasers, four 866nm repumper lasers and a single 854nm laser are now required to perform Doppler cooling. Although the $4^2P_{3/2}$ and $3^2D_{5/2}$ levels are Zeeman split, only a single 854nm laser is required as the rate at which those levels are populated is very low such that the power and the spectral impurity of a single 854nm laser is sufficient to depopulate those states.

4.4.1 The 397nm Laser

The two 397nm laser systems are tunable extended cavity diode lasers (ECDL) (DL 100 from TuiOptics). They are identical in every respect except the actual diode itself, where one of them is a (NLHV500A, maximum output power 5mW) and the other is a (NLHV3000E, maximum output power 30mW). The system consists of a laser head and electronics to drive the laser. The output of the diode is collimated by a multi-element short focal length lens. The collimated beam is then sent onto a reflection grating which returns the first order diffracted beam back into the diode (Littrow setup). The extended cavity formed by the back facet of the diode and the surface of the grating has a higher finesse than the cavity of the bare diode laser due to the higher reflectivity of the grating surface compared to the surfaces of the diode cavity. This narrows the linewidth of the laser. A measurement of the linewidth of the 397nm laser was performed to give a result of $\approx$ 3MHz. This measurement is described in more detail in the next

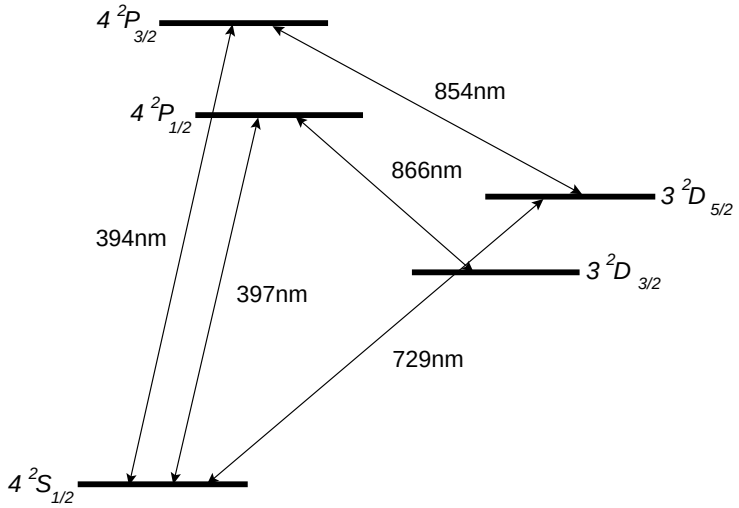

(a)

D

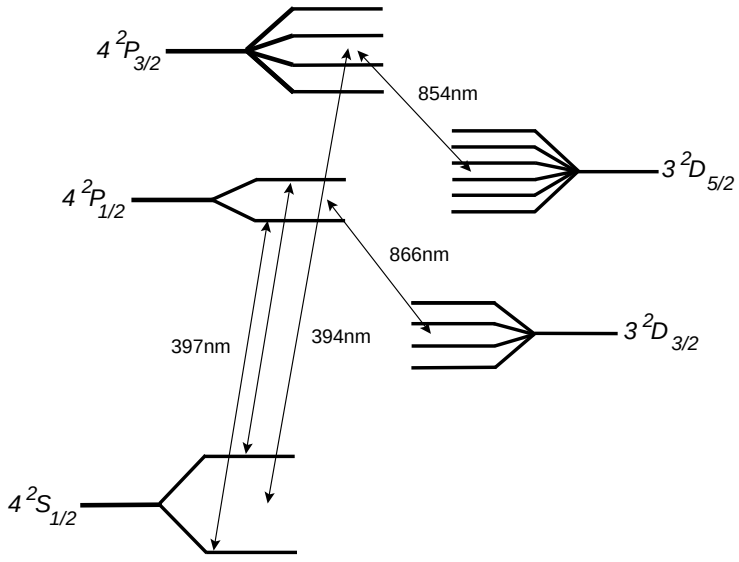

(b)

Figure 4.6: (a)Energy level scheme for Ca^+ without any magnetic field. (b)Energy level scheme for Ca^+ in the presence of a magnetic field showing the Zeeman split levels.

paragraph. The grating is attached to a low voltage piezo stack which allows for fine tuning of the output wavelength. The diode, collimator and grating holder are mounted onto a base plate which sits on top of a thermo-electric element(TEC). The TEC then sits on top of the base block which has an AD590 temperature sensor cemented onto it. The TEC and the AD590 are connected to the temperature controller which, along with the current controller, scan controller and Proportional-Integral-Differential (PID) controller are housed in a supply rack.

The linewidth measurement of the 397nm laser was done by making use of the following principle. When two lasers that are tuned to within a few MHz of each other and the beams are overlapped on top of one another on a fast photodiode, the intensity observed is a beat signal with the beat note at the difference frequency of the two lasers. The Fourier transform of such a beat signal will yield a lineshape whose centre frequency is the difference frequency. The FWHM of the lineshape will be twice the linewidth of each laser.

The measurement was done using two identical 397nm laser systems which were mixed at a beam splitter and aligned such that they were co-linear and overlapped on a fast photodiode approximately 2m away. A portion of the beat signal observed using a fast oscilloscope on a.c. coupling is shown in Fig. 4.7(a). The Fourier transform of this signal is shown in Fig. 4.7(b). The linewidth of the 397nm laser inferred from this measurement is approximately 3MHz (with a sampling time of 60μs).

It was important for the scan of the piezo to be calibrated before it was used in any of the experiments. This was done by using the method of central spot scanning with a low finesse Fabry-Perot etalon. The calibration of the piezo voltage with respect to frequency is 0.60$\pm$0.05GHz/V.

The inherent frequency drift of the 397nm laser is measured to be $\approx 300-400$ MHz/hour. This result was obtained by measuring the fluorescence signal from the ions as a function of time. During this measurement, the amount of fluorescence was made to depend solely on the detuning of the 397nm laser by constantly optimising the frequency of the 866nm and 854nm lasers for maximum signal.

4.4.2 The 866nm/854nm Laser

The 866nm/854nm lasers are home built ECDL systems. The design of the laser head is similar to that described earlier for the 397nm laser system with the positions of the grating and diode in the Littrow configuration [3]. The diodes used were of two varieties, the SDL 5411 and the LD1377 with the latter obtained from Laser 2000. Their maximum output powers are 100mW and

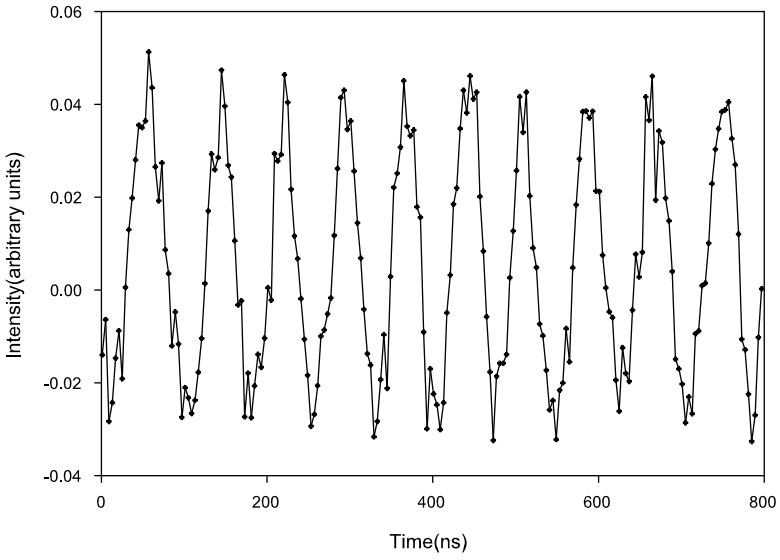

(a)

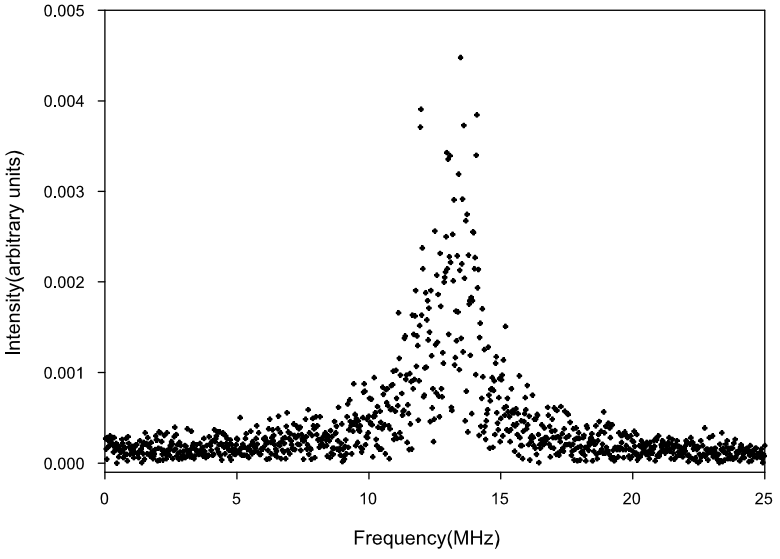

(b)

Figure 4.7: (a) A portion of the beat signal obtained by tuning the wavelengths of two identical 397nm lasers close to each other. (b) Fourier transform of the beat signal.

120mW respectively. The free running wavelength quoted for the SDL 5411 diode is 852 ± 4nm at 25°C while the LD1377 has a free running wavelength of 860 ± 4nm at 25^{0}°C. The grating is gold coated, blazed for 750nm and has 1200lines/mm.

The diodes are placed inside a collimating tube containing a single collimating lens. This sits inside a holder which is screwed onto a metal base plate. A heating resistor is glued onto this base plate and a TEC is placed below it. The heating resistors are used to heat the diodes so that their free running output wavelengths are shifted towards either 854nm or 866nm. A thermistor is placed in a hole drilled into one of the surfaces of the diode holder and thermal contact is improved by the application of heat sink compound. On some of the designs, the thermistor is placed such that it is in thermal contact with the base plate instead of the diode holder. This variation provides just as good a temperature lock as the initially described setup.

4.5 Laser Wavelength Determination

In order to be able to laser cool and detect fluorescence from Ca^{+} ions, the laser wavelengths need to be tuned to within a few linewidths of their respective transitions. To get the laser to the correct wavelength, a Burleigh WA50 wavemeter is used. Modifications to the photodetection circuit were required before the wavemeter could read at wavelengths around the region of 397nm. These modifications were performed by J. Sudbery and the details can be found in [74]. The wavemeter has a resolution of ≈ 2GHz at 397nm and ≈ 0.4GHz at 866nm. Comparing this with the Doppler broadened linewidths of the cooling and repumping transitions which are of the order of hundreds of MHz, we find that the wavemeter is just able to get the 866nm laser to the correct wavelength but does not have the resolution required to set the 397nm laser wavelength with sufficient accuracy. To fine tune the 397nm laser, absorption spectroscopy is performed using a Ca^{+} hollow cathode lamp.

The hollow cathode lamp is home built and consists of a cathode made out of a nickel tube (11.92mm outer diameter) which sits inside a larger tube made out of dural (50mm outer diameter) that acts as the anode. Crushed calcium is placed inside the nickel tube such that when the hollow cathode lamp is turned on, the calcium atoms created will coat the inside of the tube. This nickel tube is suspended inside the larger tube by cradling it using a strip of tantulum foil which is clamped onto the electrical feedthrough as shown in Fig. 4.8. The tube has glass windows at the front and back end to allow laser access. They, together with the electrical feedthrough, are attached to the main body of the hollow cathode lamp using KF flanges. The tube is evacuated using a rotary

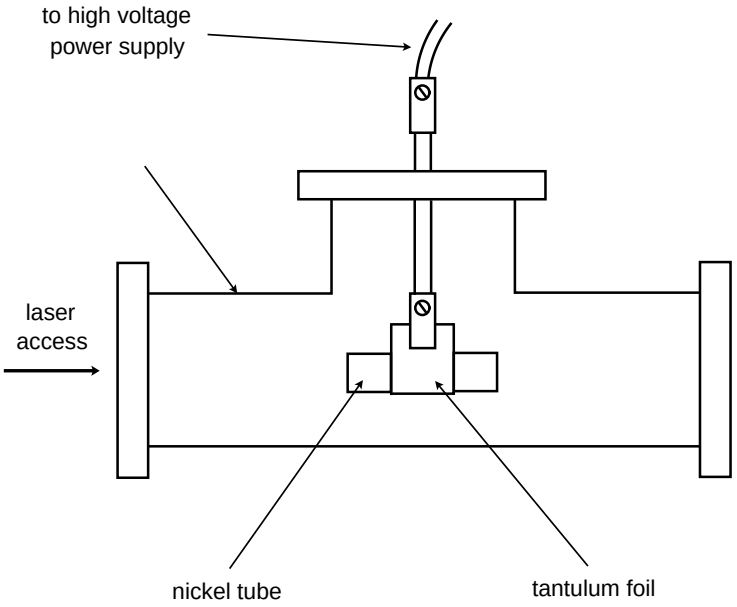

Figure 4.8: Schematic diagram of hollow cathode lamp.

pump and whilst doing so, Argon gas is leaked in at a steady rate so that the pressure inside the tube remains at $\approx 10^{-2}$ mbar. Argon gas is used for several reasons. The first is to act as a buffer gas which prevents the Ca^+ ions from accelerating too quickly towards the anode. This maintains a high concentration of Ca^+ ions at the cathode. The buffer gas also stops the windows from getting coated too quickly. A third reason for using Argon is to preferentially excite the Ca^+ ions to the $4^2P_{1/2}$ state so that the feature at 397nm is the strongest.

The operation of the hollow cathode lamp requires a high voltage, high current source. This was provided by an ionisation pump power supply which at full capacity only just manages to produce the required power. This causes the power supply to operate in a quasi pulsed mode with the maximum output power only being produced every 20ms coinciding with the mains frequency. The hollow cathode emission signal (which is the signal without the laser present) in the pulsed mode taken using a digital oscilloscope is shown in Fig. 4.9(a). This signal is obtained by placing a photodiode approximately 0.5m away from the hollow cathode lamp. Fig. 4.9(b) shows the absorption signal produced when a laser tuned onto resonance is passed through the hollow cathode and onto the photodiode. The signal shown here was taken using an a.c. coupled oscilloscope which allows the weaker absorption signal superimposed on top of the large d.c. offset to be seen more clearly. Fig. 4.9(c) shows the absorption feature at 397nm produced by manually scanning the laser in steps from below the resonance and

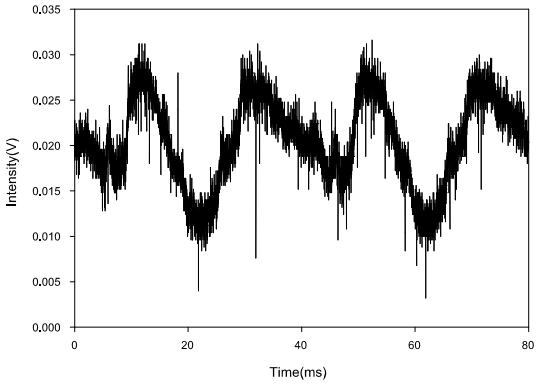

(a)

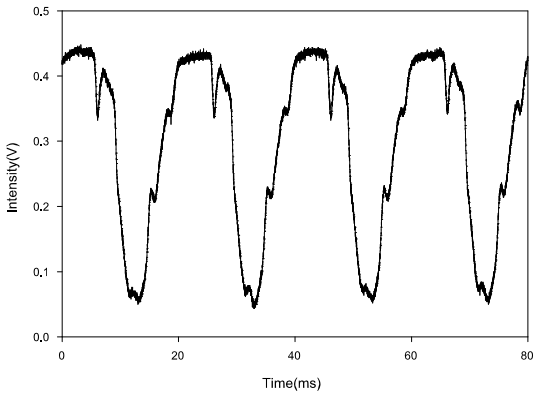

(b)

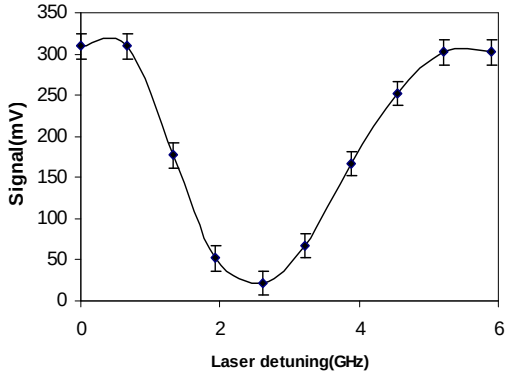

(c)

Figure 4.9: (a)Hollow cathode emission spectrum and (b)absorption spectrum at 397nm operating in pulsed mode. (c) Hollow cathode absorption spectrum obtained by manually tuning 397nm laser.

across the feature whilst measuring the amount of light transmitted through the hollow cathode lamp onto the photodiode. It can be seen that the width of the feature allows for the central peak to be located to a higher precision than the resolution of the wavemeter. The presence of a hollow cathode lamp also allows the wavemeter to be calibrated for wavelengths in the region of 397nm. This is useful as the wavemeter calibration might change unexpectedly.

4.6 Electronic Detection

Once the laser wavelengths were correctly determined, the next priority was to detect the presence of Ca^+ ions in the trap. As was described in Section 4.1.2 the ions are produced by crossing a beam of calcium atoms with an electron beam, whose intensities in turn depend on the amount of current passed through the oven and filament. To ensure that there were Ca^+ ions formed and trapped in both the Paul and Penning trap, electronic detection of the ions was used.

The setup for electronic detection is shown schematically in Fig. 4.10. It consists of three electronics boxes. Box 1 is a tuned circuit made resonant at the axial trap frequency and is connected to the end caps, thereby coupling the trap to this tuned circuit. Also contained in Box 1 are two filter circuits which serve to filter out the r.f. trap drive when in use with the Paul trap. Box 2 is a pre-amplifier and is also weakly coupled to the tuned circuit. Box 3 contains a selective amplifier and an r.m.s. to d.c. converter. When a small r.f. drive voltage is applied to Box 1 at its resonant frequency, the output of Box 3 shows a d.c. output which is proportional to the amplitude of oscillation generated in Box 1. This d.c. output together with the trap d.c. voltage can be monitored on x-y plotter. It can be seen from Eq. 2.8 and Eq. 2.14, 2.17 and 2.28 that the axial frequencies of the Penning and Paul traps are functions of the trap d.c. voltage. When the d.c. voltage is scanned such that the axial frequency coincides with the resonant frequency of the tuned circuit, the ions absorb energy from the tuned circuit causing a sudden decrease in the d.c. output which is seen as a dip on the x-y plotter.

An example of this is shown in Fig. 4.11. This trace was taken for a Penning trap with the tuned circuit resonant at 340kHz. The presence of three distinct dips whose positions are displaced from one another can be seen. A possible explanation for the displacement in the position of the dips could be due to space charge effects. The detection process requires the continuous operation of the oven and filament, so that ions are continuously generated. This is necessary because the lack of any cooling mechanism means that the storage lifetime of the ions is too short for the detection process to work if the trap is only loaded once. A consequence of this is the build up of space charge which alters the

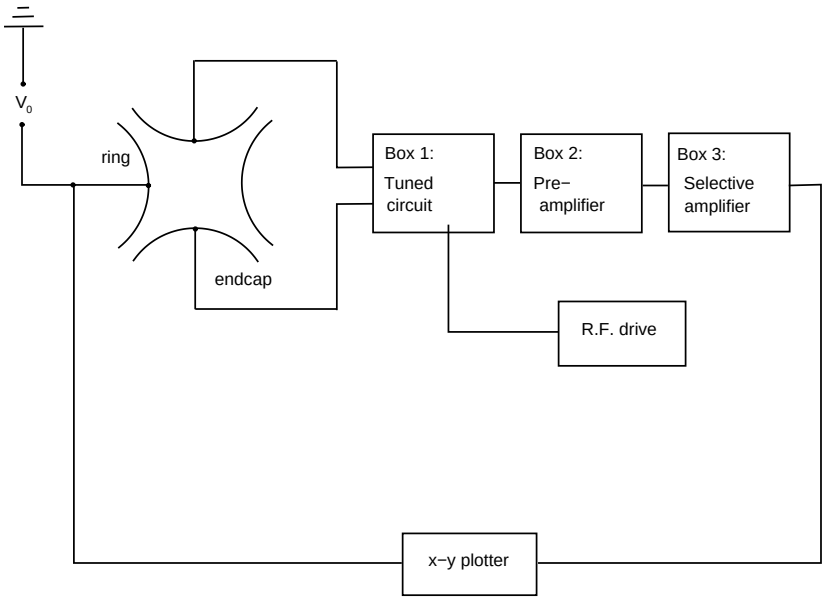

Figure 4.10: Schematic diagram for electronic detection.

trap frequencies and hence the position of the dips in the electronic detection trace. The sharpness of the dip depends on the amplitude of the drive voltage applied to the tuned circuit. This was set typically to 30-40mV which gave the best result. Too high a value, will cause the ions to be driven out without registering a dip on the trace while too low a drive amplitude will have no effect on the ions. During the steady-state operation of the oven and filament, their operating currents were lowered. We were also careful not to operate the oven continuously for more than two minutes for fear of completely depleting it.

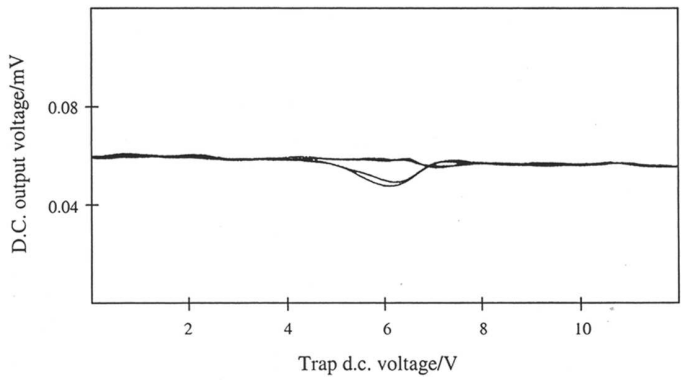

Figure 4.11: Electronic detection trace of Ca^+ ions in a Penning trap.

Chapter 5

The Paul Trap

Operating in the Paul mode allows the trap and detection optics to be tested and characterised and the laser wavelengths to be calibrated before operating in the Penning mode. The testing, characterising and calibration are done by trapping, cooling and observing single Ca^+ ions in the Paul trap. The experimental setup, operation of the Paul trap and quantum jump results for a single and a few ions are described in this chapter.

5.1 Electrical Connections

The electrical connections for the Paul trap are shown schematically in Fig. 5.1. The trap is driven by a 360V (peak to peak) sinusoidal potential oscillating at 1.83MHz. This potential is produced by sending an 80mV output from a function generator (HP 3325B) to an r.f. amplifier (ENI 325LA) The output of the amplifier is fed into Box A which is connected to the ring electrode. Box A contains an air core transformer which allows a d.c. offset to be added on top of the r.f. potential. This is done by placing an inductor directly after the d.c. supply and a capacitor directly after the second coil of the transformer as shown in Fig. 5.2. The d.c. will see a high impedance across the capacitor which prevents it from affecting the r.f. supply and similarly the r.f. will see a high impedance across the inductor which protects the d.c. power supply. The whole circuit is also coupled to the trap electrodes and together they behave as a tuned circuit resonant at the trap drive frequency of 1.83MHz. A d.c. offset of 6V is applied to the ring with respect to the endcaps which are grounded. This produces trap oscillation frequencies of $\omega_r \approx 1.3$MHz and $\omega_z \approx 2.0$MHz.

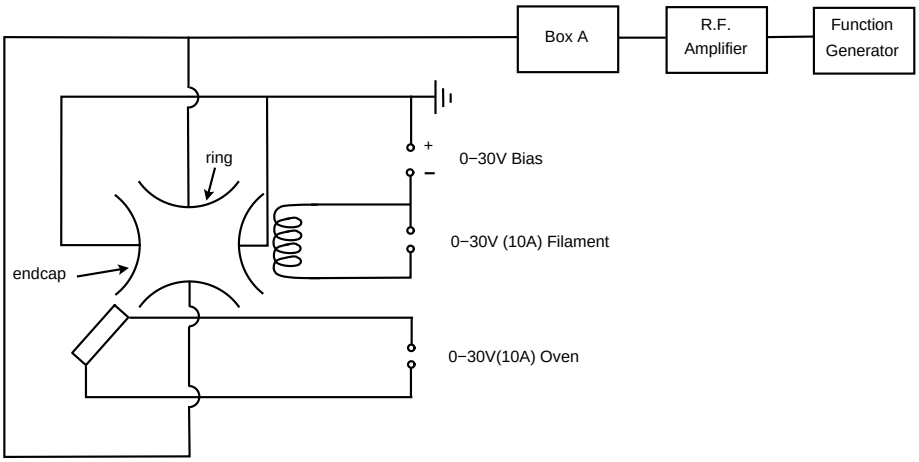

Figure 5.1: The Paul trap wiring diagram.

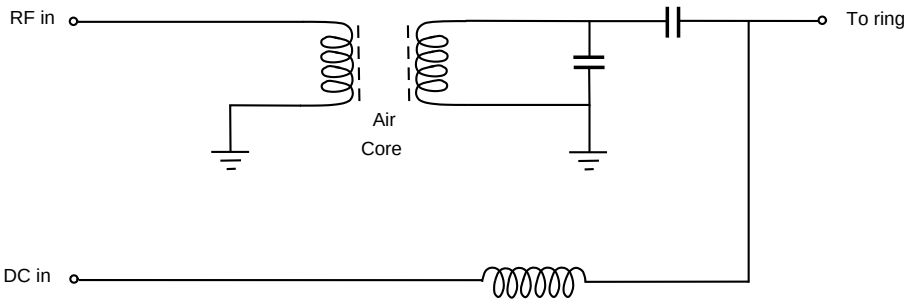

Figure 5.2: Circuit diagram of Box A.

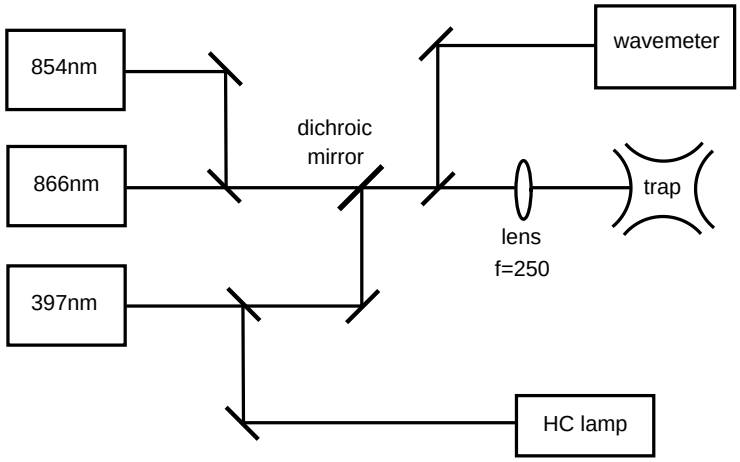

Figure 5.3: Schematic of experimental setup used for Doppler cooling in the Paul trap.

5.2 The Optical Setup

The optical layout for the Doppler cooling of Ca^+ ions in a Paul trap is shown in Fig. 5.3. The wavelengths of the diode lasers are set to 397.959nm, 866.451nm and 854.443nm using the wavemeter. The 397nm laser is sent into the hollow cathode for further fine tuning. It is then set to scan at a rate of $\approx$ 1Hz and at an amplitude of $\approx$ 3.6GHz starting from the red side of the absorption feature up to the peak of this feature.

The three lasers are combined using a dichroic beam splitter before passing through a lens ($f = 250$mm) which focusses the 397nm beam at the centre of the trap and the infrared beams slightly farther away due to chromatic abberations. Consequently, the infrared beam waists at the centre of the trap are larger than the minimum beam waist of the 397nm laser and so their intensities are not at a maximum. However, the chromatic abberations have not been corrected for because there is more than sufficient power to saturate the corresponding infrared transitions. This was verified when the observed fluorescence signal decreased by only 10-15% when the 866nm laser power was reduced by $\approx$ 50% (this was done with the 854nm laser at full power). The 854nm laser was also tested in the same way (with the 866nm laser at full power) and was found to be over saturating the respective transition as the fluorescence signal was not affected until the laser power was reduced to 1×10^{-5} of its initial value. The laser beam waist sizes (measured using the knife edge test), measured intensities and saturation intensities of the respective transitions are given in Table 5.1. The power of the lasers were measured at the position of the lens before the

Transition	λ/nm	Saturation intensity/mWmm^{-2}	Measured intensity/mWmm^{-2}
$4^2S_{1/2} \rightarrow 4^2P_{1/2}$	397	0.87	1.7×10^{3}
$3^2D_{3/2} \rightarrow 4^2P_{1/2}$	866	6.5×10^{-3}	1.5×10^{2}
$3^2D_{5/2} \rightarrow 4^2P_{3/2}$	854	6.4×10^{-3}	1.1×10^{3}

Table 5.1: Laser parameters used for trapping and cooling in the Paul trap.

trap. The saturation intensity is given by the equation

$$I_s = \frac{\hbar\gamma\omega^3}{\pi c^2}, \tag{5.1}$$

where γ is the natural linewidth of the transition and ω is the line centre frequency.

It is advantageous to have the infrared beam waists larger than the 397nm beam waist so that the beam steering controls are less critical when overlapping the infrared beams on top of the 397nm beam at the centre of the trap. The dichroic beam splitter is mounted onto a mount with micrometer adjustments. This allows for the 397nm laser to be accurately positioned at the position of the ions. As the beam positioning of the infrared lasers are less critical, they are steered into the trap by a standard mirror mount. To make sure that the three beams overlap at the centre of the trap, they are overlapped at the dichroic beam splitter and at a point $\approx$ 2m away after the trap.

Once the wavelengths of the 397nm and the infrared lasers are set and the beams sent into the trap, it is necessary to place them as close as possible to the centre of the trap. This is done by moving the 397nm beam position horizontally and vertically in turn across the aperture of the ring electrode and observing the intensity of the light detected by the PMT. As soon as part of the beam hits the electrode and does not go through the trap cleanly, the PMT registers an increase in the count rate. The centre of the trap in the horizontal and vertical plane is found between the two maximum count rates. The infrared beams are then aligned on top of the 397nm beam.

5.3 Trap Operation

The ions are loaded into the trap by heating an oven and a filament. The oven is turned on for 32s and the filament is turned on 20s later for 12s such that they are both simultaneously running for the last 12s. To generate a large cloud of ions, the oven current is set to 2.00A and the filament current to 5.00A. A weak magnetic field ($\sim$ 0.1T) is applied along the axis of the trap during the loading procedure to guide the electrons towards the centre of the trap. The

magnetic field is provided by an Oxford Instruments Electromagnet N100 fitted with tapered poled pieces with 58mm faces. The trap in its vacuum housing sits in between the pole pieces of the magnet which are then screwed in such that they are touching the vacuum housing. The electromagnet is capable of producing a magnetic field of ≈ 0.97T (measured between the pole pieces) at the full operating current of 15A. This electromagnet also provides the magnetic field needed to operate the Penning trap.

The oven operating parameters were found by "testing" it. This test was done by placing the oven in a vacuum of $\approx 10^{-5}$mbar and heating it until it produced a thin coating of calcium on a polished copper plate. The amount of current and time it took to produce a coating was then used as a lower limit for the oven operating parameters during the initial stages of setting up the trap. Once the laser wavelengths, beam positions and detection optics were optimised, it was possible to reduce the oven current and still obtain a high fluorescence signal level. The filament operating parameters were chosen such that it was just above the threshold of electron emission with the electrons only generated for the last 2s of the filament "on" time. This parameter was found by firstly measuring the electron flow rate along the axis of the trap across to the other endcap. We have found that the current required is of the order of tens of nanoamps. This gives an estimate for the filament operating parameters. It was further optimised by setting the paramaters such that increasing the current or "on" time produces no further increase in the number of ions trapped.

The size of the ion cloud can be varied by either changing the period of the "on" time of the oven or its operating current. As soon as the loading procedure is completed, the fluorescence from the ions is immediately detected if the laser wavelengths are close enough to resonance. The wavelengths of the 397nm and 866nm lasers are then finely adjusted to obtain the maximum signal. The beam positions of both these lasers are also adjusted for the same reason.

5.3.1 Results

A typical Doppler cooling trace of Ca^+ ions in a Paul trap is shown in Fig. 5.4. This is a trace of fluorescence signal from the ions plotted as a function of frequency. The peak is produced by scanning the 397nm laser from below resonance up to line centre and back to the starting point of the scan. The asymmetry is due to the laser having a sharp fly-back when going from line centre back to the starting point. The infrared lasers are constant in frequency. This trace is obtained by accumulating the fluorescence signal a total of 25 times to improve the signal to noise ratio. The width of the peak is a measure of the ion cloud temperature. For Fig. 5.4, the FWHM is ≈ 330MHz which corresponds to an

upper temperature limit of $\approx$ 15K. The method by which the temperature is calculated from the cooling trace is described in more detail in Appendix A.

The effects of the amplified spontaneous emission (ASE) from the 397nm laser can be seen from the cooling trace shown in Fig. 5.5. Here a sequence of two scans of the 397nm laser is shown with the width of the scan set at 3.6GHz. The first cooling peak was obtained with all three laser beams present in the trap. Following that, the 854nm laser beam was completely blocked resulting in the fluorescence signal level dropping to half of its initial value. This suggests that the ion decays into the metastable $3^2D_{5/2}$ level at a rate roughly equal to the reciprocal of the lifetime of the $3^2D_{5/2}$ level which is about once every second. Therefore, only a very small amount of 854nm laser power is needed to depopulate that metastable state. This is evident from the laser power saturation tests done and as well as from the insensitivity of the fluorescence signal to the wavelength of the 854nm laser. We know that the population transfer into the $3^2D_{5/2}$ level is due to ASE from the 397nm laser from quantum jump tests (see Sec. 5.5). We have found that the rate of quantum jumps and hence population transfer into the $3^2D_{5/2}$ level is proportional to the intensity of the 397nm laser with the population transfer becoming negligible at low 397nm laser intensity.

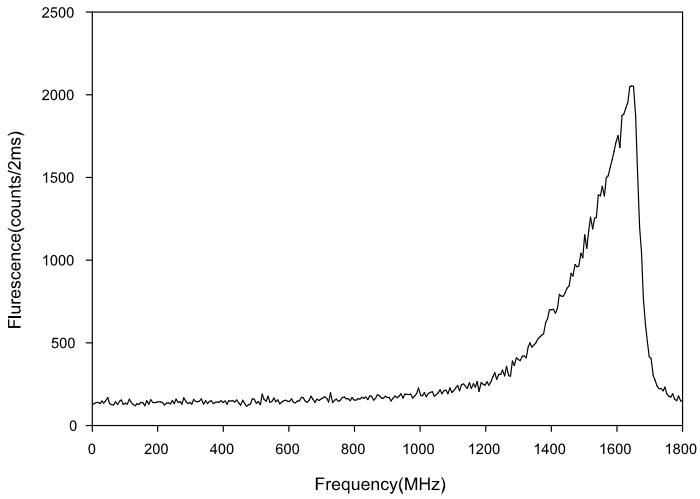

Figure 5.4: Laser cooling trace of ions stored in a Paul trap.

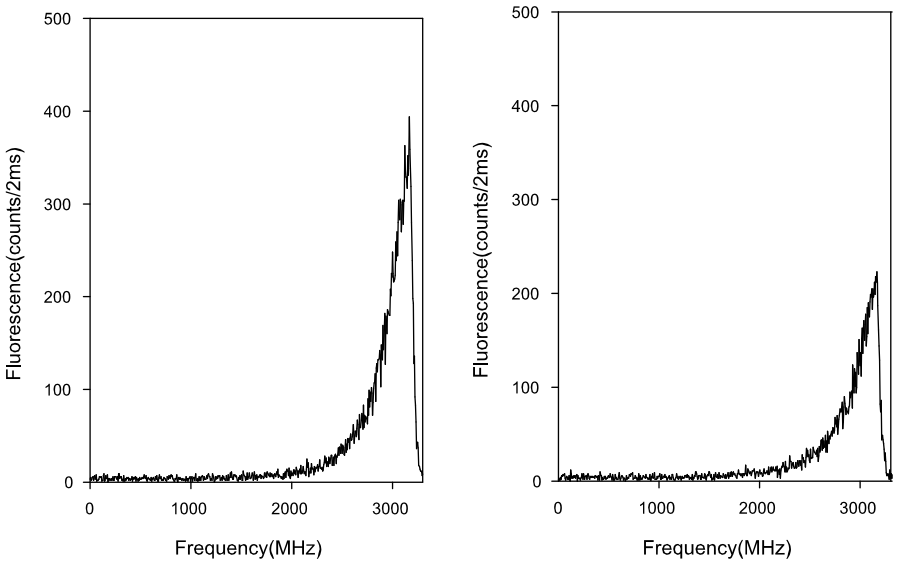

Figure 5.5: Laser cooling trace of ions stored in the Paul trap. The trace on the right was taken without the presence of the 854nm laser. The drop off in signal by a factor of two suggests that the ions decay into the $3^2D_{5/2}$ about once every second.

5.4 Nulling the B-Field

Although there is no current running through the coils of the electromagnet when operating in the Paul trap mode, there is still a small residual B-field present. This is a result of the pole pieces of the magnet becoming permanently magnetised from their constant use. To null the B-field, a reverse current is applied through the coils of the electromagnet. This is provided by a low current external power supply which provides a finer adjustment of the current than the original power supply. The amount of current required is found using the fluorescence from the ions as a diagnostic. This is done by tuning the wavelength of the 397nm laser onto the line centre of the $4^2S_{1/2} \rightarrow 4^2P_{3/2}$ transition to obtain a constant level of fluorescence. The current can then be tuned to find the maximum level of fluorescence which is the point where the residual B-field is nulled. This happens because the Zeeman splitting is eliminated and the cooling and repumping lasers are able to address their respective transitions more efficiently. The signal level at this point is $\approx 20\%$ higher than the non-nulled fluorescence level. Approximately 60mA of current is used to produce this effect which suggests a residual B-field of about 6mT.

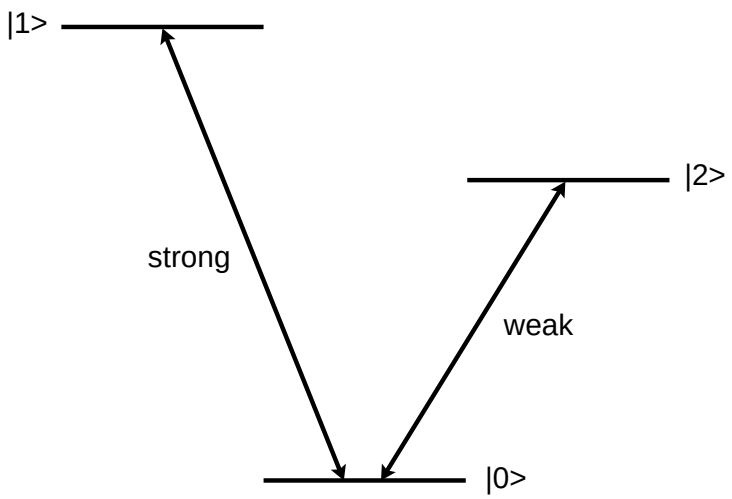

Figure 5.6: Typical energy level scheme of a quantum jump system.

5.5 Quantum Jumps in the Paul Trap

The procedure for trapping a single Ca^+ ion is as follows. Once a large cloud is successfully loaded and the beam positions and laser wavelengths optimised, the trap is emptied by switching off the r.f. field. The oven current is then lowered by a small amount and the trap reloaded. The beam positions and laser wavelengths are then re-optimised for maximum signal. The change in the beam positions should not be necessary if the beams were already positioned at the centre of the large ion cloud. However, in practice it is difficult to do so hence the requirement for re-optimising the beam positions. The laser wavelengths need to be adjusted because Doppler broadening is reduced. This happens because there is less micromotion which causes r.f. heating closer to the centre of the trap. The trap is then emptied and reloaded at an even lower oven current. This procedure is repeated until no fluorescence is observed. The lowest discernable fluorescence signal is then tested for quantum jumps. The observation of quantum jumps is a reliable way of determining the presence of a single ion. A quantum jump is a process whereby an atomic system makes an instantaneous transition between one quantum state to another. These jumps are not observed when large numbers of ions are present as the measured quantity, which in this case is the fluorescence level, will be the ensemble average of all the ions present. However, in cases where only a single ion or small numbers of ions are present, the observed jumps appear as a discrete step (in the former case) or a few discrete steps (in the latter case) in the fluorescence level.

To describe this phenomenon in more detail consider an ion with the energy

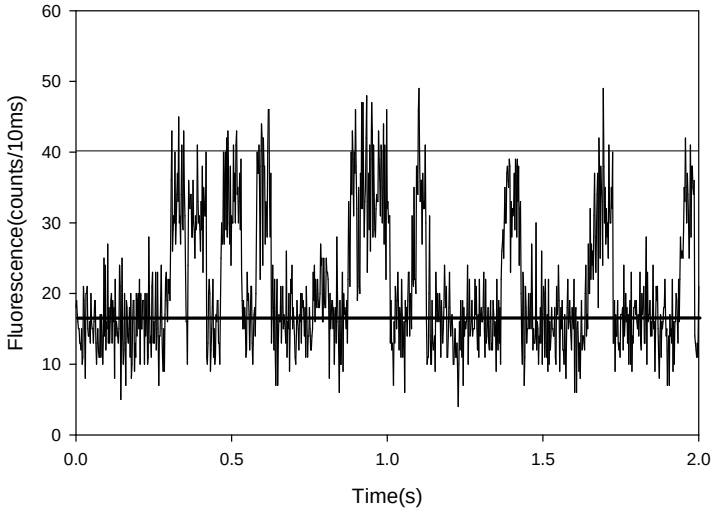

Figure 5.7: Trace of a single Ca^+ ion undergoing quantum jumps.

level scheme shown in Fig. 5.6 where the transition from level $|0\rangle$ to $|1\rangle$ is a strongly allowed dipole transition and level $|2\rangle$ is a long-lived metastable state. If the ion is illuminated with radiation that is resonant with the $|0\rangle$ to $|1\rangle$ transition, it absorbs and re-emits photons and fluorescence is detected. If radiation resonant with the $|0\rangle$ to $|2\rangle$ transition is absorbed instead, the ion will be pumped into the long-lived metastable state and remain there for the lifetime of that state. During that time, no fluorescence will be detected. When the ion decays back into the $|0\rangle$ state, it can cycle through the $|0\rangle$ to $|1\rangle$ transition and fluorescence can be detected once again. This leads to discrete steps in the fluorescence signal as described earlier.

5.5.1 Results

For the Ca^+ ion, quantum jumps occur when the ion is excited off-resonantly into the $4^2P_{3/2}$ level and decays into the $3^2D_{5/2}$ level. In the current setup, the ASE from the 397nm laser provides the off-resonant excitation but the quantum jumps are inhibited due to the presence of the 854nm laser. To allow for quantum jumps, the 854nm laser is blocked off. Fig. 5.7 shows quantum jumps of a single Ca^+ while Fig. 5.8 shows quantum jumps of two Ca^+ ions. Lines are drawn to make the steps in the fluorescence signal more obvious.

From Fig. 5.7, the fluorescence signal from a single Ca^+ is ~ 2000 counts per second. Theoretically, the maximum number of photons scattered per second

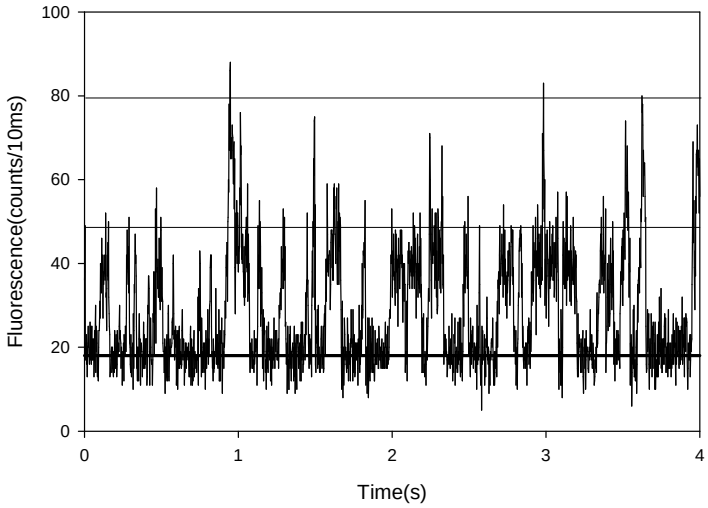

Figure 5.8: Trace of two Ca^+ ions undergoing quantum jumps.

from a single Ca^+ ion in the Paul trap is $A/4 \approx 4.9 \times 10^7$, where A is the Einstein A coefficient for the $4^2S_{1/2} \rightarrow 4^2P_{1/2}$ transition. The factor of $1/4$ is present because of the laser cooling scheme for Ca^+. From Fig. 4.6(b) of Chap. 4, it can be seen that on average, the population of the ions is shared between three levels, the $4^2S_{1/2}, 4^2P_{1/2}$ and $3^2D_{3/2}$ levels. If we take into account the degenerate energy levels, the population is then shared between eight levels giving a scattering rate of $A/8$. However, because a single laser is sufficient to address the degenerate $4^2S_{1/2} \rightarrow 4^2P_{1/2}$ levels, the scattering rate is effectively $2 \times A/8 = A/4$. The maximum signal that can be observed from a single ion in the Paul trap is given by

$$\begin{aligned} S_{Paulmax} &= \xi \times A/4 \\ &= 1.7 \times 10^{-4} \times 3.7 \times 10^7 \\ &\approx 6,300 \text{counts/s}, \end{aligned} \tag{5.2}$$

where $S_{Paulmax}$ is the maximum signal from a single ion in the Paul trap, ξ is the detection efficiency and A is the Einstein A coefficient.

From this comparison, the actual observed signal is roughly three times lower than the calculated one. One possible reason for this discrepancy could be due to r.f. heating. This is possible even for the case of only a single ion present in the trap as the ion might not be sitting in the middle of the potential well due

to patch potentials. Another reason could be due to an underestimation in the values used to quantify the detection efficiency.

Chapter 6

The Combined Trap

In the last chapter, it was shown that single Ca^+ ions have been successfully trapped and cooled in the Paul trap. This has allowed the laser frequencies and detection efficiency to be calibrated for use in the Penning trap. Operation in the Paul trap has also allowed the characterisation of the loading procedure. The next logical step would be to trap and cool directly in the Penning trap. However, this was not possible as there was no means of determining the laser frequencies to accuracies of the order of hundreds of MHz. A high precision wavemeter would suffice and is currently being built at the time of writing. The alternative method used to set the laser wavelengths for use in the Penning trap involved the use of the combined trap. This method will be described in more detail below.

6.1 The Experimental Method

The combined trap is obtained by adding a magnetic field on top of the existing r.f field of the Paul trap. As was mentioned earlier, the transition from the Paul trap to the combined trap can be done without affecting the ions catastrophically; the ions remain trapped after the magnetic field is turned on. The presence of a magnetic field however, increases the number of $4^2S_{1/2} \rightarrow 4^2P_{1/2}$ and $3^2D_{3/2} \rightarrow 4^2P_{1/2}$ transitions due to the Zeeman splitting. The transitions in frequency space when a magnetic field is applied are shown in Fig. 6.1. For the ions to be laser cooled, the $4^2S_{1/2} \rightarrow 4^2P_{1/2}$ and the $3^2D_{3/2} \rightarrow 4^2P_{1/2}$ transitions need to be closed. Although there are four $4^2S_{1/2} \rightarrow 4^2P_{1/2}$ transitions (two π and two σ), only two of them need to be addressed at any one time for the cycle to be closed. Similarly, only four out of the six $3^2D_{3/2} \rightarrow 4^2P_{1/2}$ transitions need to be addressed at any one time for that cycle to be closed. The two $4^2S_{1/2} \rightarrow 4^2P_{1/2}$ transitions are addressed using two 397nm lasers.

The π transitions are chosen because they are have the smaller detunings from the zero magnetic field frequency. The four $3^2D_{3/2} \rightarrow 4^2P_{1/2}$ π transitions are addressed using four 866nm lasers. The $4^2P_{3/2} \rightarrow 3^2D_{5/2}$ transitions are split into 12. However, only one 854nm laser is required to close that cooling cycle as the pumping rate into those levels is very low. This was confirmed when an additional laser tuned to the furthest detuned of the $4^2P_{3/2} \rightarrow 3^2D_{5/2}$ transitions did not produce any increase in the amount of fluorescence signal.

The procedure for setting the laser wavelengths for the Penning trap via the Paul and Combined trap is as follows. The first step in this technique is to trap and cool a large cloud of ions in the Paul trap. Once the laser wavelengths are optimised for maximum fluorescence, a small magnetic field ≈ 0.3T is applied creating a Combined trap. The fluorescence level immediately drops to the background level as the lasers are no longer in resonance with the transitions. At this stage, more lasers are added to the setup to address the increased number of transitions making it a total of two 397nm, four 866nm, and one 854nm laser. All the laser wavelengths apart from the 854nm laser need to be detuned to their relevant transitions. The amount of detuning that is required is known since the strength of the magnetic field is known. For the 397nm lasers, the detuning can be set by adjusting the piezo voltage since it has been calibrated against frequency while the 866nm lasers are set using the wavemeter. As there is a level of uncertainty in the calibration of the 397nm laser piezos as well as the limited precision of the wavemeter, the wavelengths of the lasers will not be exactly on resonance. However, it is sufficiently close for fluorescence to be observed and maximum fluorescence can be obtained by optimising the laser wavelengths. The magnetic field is then increased by a further 0.3T and the process of iterating the laser wavelengths is repeated to obtain maximum fluorescence. In this way the magnetic field is increased until the point at which the trap can be operated as a Penning trap.

Operation of a Penning trap can only be achieved in the presence of a magnetic field that is strong enough to provide radial confinement of the ions. We have found that it is possible to operate the Penning trap with a magnetic field as low as 0.75T. However, for convenience, we have typically operated at 0.78T as it corresponds to 9A of current through the coils of the electromagnet. Once a Combined trap of 0.78T is established and the fluorescence signal maximised, the trap parameters are re-set for operation as a Penning trap. To do this, the r.f. drive is turned off and the polarity of the d.c. offset applied to the ring with respect to the endcaps is reversed. Switching off the r.f. drive causes the ions to be lost and the trap then needs to be reloaded. This happens because the ion cloud has to change its sense of rotation which cannot be done instantaneously when going to the pure Penning trap from the combined trap. Once the loading

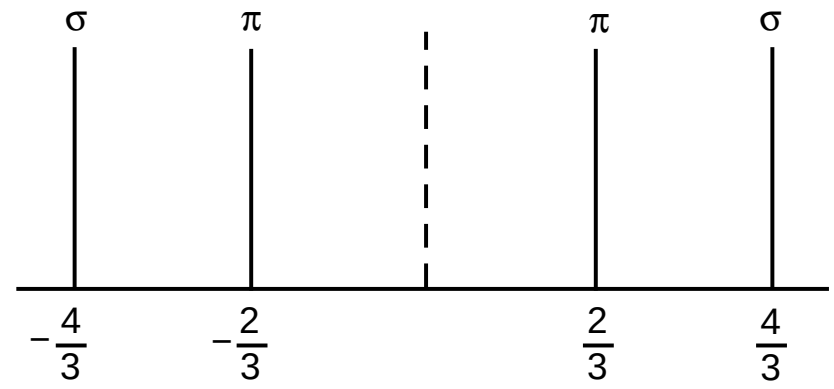

(a)

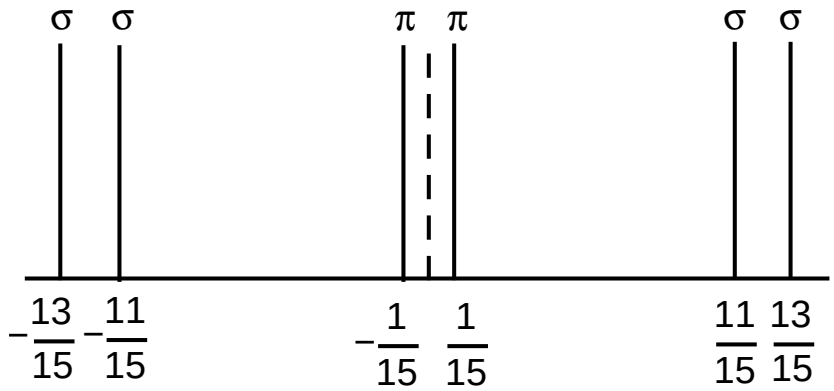

(b)

Figure 6.1: (a) $4^2S_{1/2} \rightarrow 4^2P_{1/2}$ and (b) $3^2D_{3/2} \rightarrow 4^2P_{1/2}$ transitions shown in frequency space in the presence of a magnetic field. The broken lines indicate the frequency positions in zero field. The fractions are in units of $(\mu_B B)/h$ where $\mu_B = e\hbar/2m$.

procedure is completed and a small fluorescence signal obtained, the laser wavelengths and the beam position of the lasers are adjusted to obtain maximum signal. Although the magnetic field remains the same going to the Penning trap from the Combined trap, adjustment of the laser wavelengths is still necessary because the ion cloud has a Doppler width which is much narrower without the presence of r.f. heating, hence the lasers are no longer in resonance with the transitions. The beam positions adjustment is necessary as the position of the potential well minimum has moved with the changing of the trapping fields due to trap imperfections such as patch potentials.

6.2 Results

A typical Doppler cooling trace of ions in a Combined trap is shown in Fig. 6.2. The fluorescence signal is a summed over 25 individual scans. The magnetic field is at 0.78T which corresponds to a current of 9A through the coils of the electromagnet. This is also the typical magnetic field used to operate as a Penning trap. The FWHM of the peak is calculated to be $\approx$ 680MHz which corresponds to a upper temperature limit of $\approx$ 60K. This is about four times higher than the temperature obtained for a cloud of ions in the Paul trap. One would expect the temperatures to be comparable since the dominant source of heating, r.f. heating is present to the same extent in both traps. The difference could be due to the fact that two cooling lasers are used in the combined trap instead of just one in the Paul trap. This makes it more difficult to set the laser frequencies for optimal Doppler cooling. For optimal Doppler cooling, the laser frequencies need to be red detuned by half the linewidth of the cooling transition. This is particularly difficult to do in the combined trap because of the presence of severe Doppler broadening from the r.f. heating.

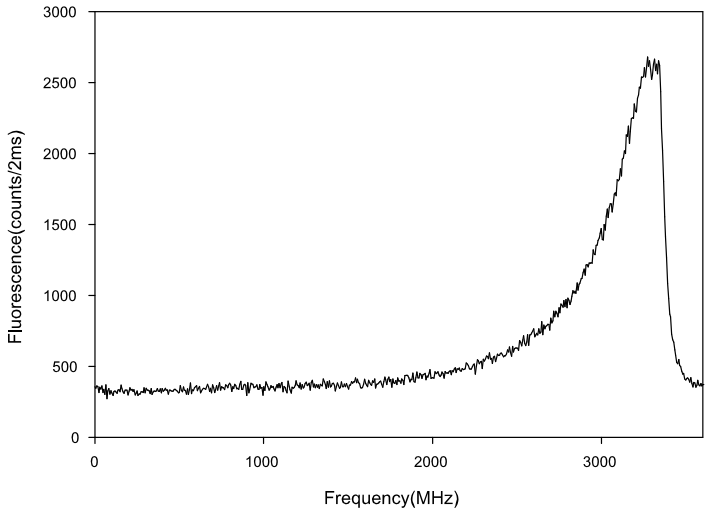

Figure 6.2: Laser cooling trace of ions in a 0.78T combined trap.

Chapter 7

The Penning Trap

In the previous chapter, the method used to perform Doppler cooling in the Penning trap was described. It required the use of two 397nm lasers, four 866nm lasers and a single 854nm laser. The requirement for four 866nm lasers can be reduced to two 866nm lasers by generating sidebands on each of the two remaining lasers. This is described in more detail in Sec. 7.1 of this chapter.

The diode lasers have an inherent frequency drift of the order of hundreds of MHz/hour. To obtain maximum fluorescence from the ions requires the laser frequencies to be constantly adjusted so that they remain on resonance with their relevant transitions. This is workable in the Paul trap as only two lasers, the 397nm and 866nm lasers, require the constant attention (the 854nm laser needs less attention as the fluorescence signal is insensitive to the drift in the 854nm laser). However, when in the Penning trap, the increased number of lasers required means that this method of operation becomes unworkable. Also, we have found that in our particular trap, the typical Doppler width of a cloud of ions is narrower when in the Penning trap than in the Paul trap due to the lack of r.f. heating. This makes the ability to Doppler cool in the Penning trap more sensitive to the drift in laser frequencies. These difficulties were overcome by frequency locking the lasers to optical cavities. The locking techniques used for both the 397nm and 866nm lasers are described in Sec. 7.2.

Another method of addressing the $3^2D_{3/2} \rightarrow 4^2P_{1/2}$ transitions was attempted but proved unsuccessful. It involved the application of microwave radiation to couple the Zeeman split $3^2D_{3/2}$ levels to each other and using just a single 866nm laser tuned to one of the allowed $3^2D_{3/2} \rightarrow 4^2P_{1/2}$ transitions. This in effect couples all the $3^2D_{3/2}$ states to one of the $4^2P_{1/2}$ states. Details of this method will be described in Sec. 7.3.

The motional resonances of ions in a Penning trap were driven to obtain a better calibration of magnetic field vs. current through the magnet coils. This

calibration is an improvement to the one previously obtained by measuring the magnetic field at different currents using a Hall probe placed in between the pole pieces of the magnet. Using motional resonances, the magnetic field measured is that experienced by the ion itself. This allowed the sideband frequency to be set more accurately. Details on the method and results obtained are described in Sec. 7.4.

The final part of this chapter, Sec. 7.5, describes the methods used to trap small clouds of Ca^+ ions in an attempt to trap single Ca^+ ions in a Penning trap. Quantum jumps of probably 2 ions are inferred from data presented in the results section.

7.1 Sidebands on 866nm Lasers

Fig. 6.1 from Sec. 6.1 of Chap. 6 shows the $3^2D_{3/2} \rightarrow 4^2P_{1/2}$ transitions in frequency space. Two 866nm lasers with sidebands are used to address the four σ transitions. Each pair of σ transitions on either side of the broken line is addressed using a single 866nm laser with sidebands. This is done by parking the carrier in between the two σ transitions and setting the sideband frequency to be half their separation.

This method was not employed when operating in the Combined trap as it would mean changing the sideband frequency each time the magnetic field is increased. This is not ideal as the amplitude of the sidebands depends critically on the frequency at which they are generated. Although there is a facility which allows the amplitude to be re-optimised, this means having to adjust another parameter. Also, the relatively small amplitude of the sidebands ($\approx 8\%$ of the carrier) means that the frequency position for maximum fluorescence becomes more sensitive. Obtaining maximum fluorescence in the combined trap using this repumping scheme becomes very time consuming. In any case, operation in the combined trap is only intended as a means to set up the lasers for use in the Penning trap.

Sidebands on the 866nm lasers are produced by directly modulating the current supplied to the laser diode at the sideband frequency. The setup used is shown in Fig. 7.1. A single function generator (Agilent 83650L) is used to drive the two laser diodes. This is done by splitting the output from the function generator using an r.f. splitter (Minicircuits ZFRSC-42). Each output from the splitter is then sent into two identical systems using a high frequency microwave cable (M/A Com Testline 18). The first component after the splitter is a stub-tuner (Microlab FXRS3-05F) which is used to match the impedance of the function generator to that of the components after the stub-tuner. The output of the stub-tuner is then connected onto the bias-tee (Minicircuits ZFBT-6G-

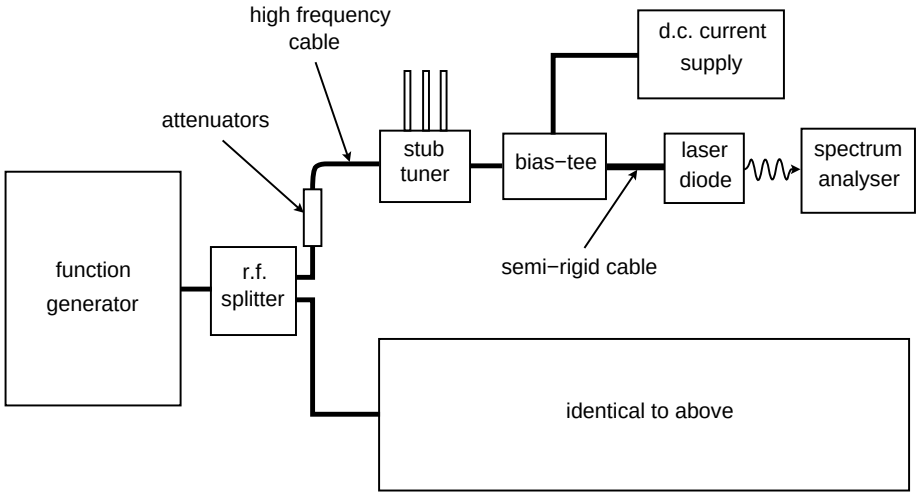

Figure 7.1: Schematic diagram showing setup used for generating sidebands on 866nm laser diodes.

FT) which is used to combine the d.c. current for the diode and the r.f. drive. The output of the bias-tee is connected to a homebuilt semi-rigid cable. The cable (RG402/U, max operating frequency 20GHz) has an inner conductor made out of solid silver-coated copper-clad steel and is insulated with PTFE dielectric. Together, they are housed in a solid seamless copper tube. A length of $\approx$ 10cm was used. An SMA connecter was attached to one end of the cable which allows connection to the bias-tee while the other end is left bare so that it can be soldered onto the appropriate pin of the laser diode. The advantage of using a semi-rigid cable as opposed to a flexible one is that its impedance is less likely to change. This is true because the impedance is affected by the shape of the cable and since a semi-rigid cable is more difficult to deform, the impedance should stay constant. The output of the laser is sent into an optical spectrum analyser so that the presence of sidebands can be verified. For a magnetic field of 0.78T, the sidebands were generated at a frequency of 725MHz.

The amplitude of the sidebands generated greatly depends on the particular diode that is being driven. It was found that the sideband amplitude on the SDL diode is nearly twice that generated on the Laser 2000 diode using the same drive amplitude. It was also found that driving the diode too hard causes the sidebands to become unstable to the point that it becomes impossible to tune the laser frequency without losing the sidebands completely. To overcome this, attenuators are placed after the r.f. splitter along the arm of the more sensitive laser so that the sideband amplitude is roughly the same on the two diodes for the same drive amplitude. Sideband amplitudes of $\approx$ 10% of the carrier are

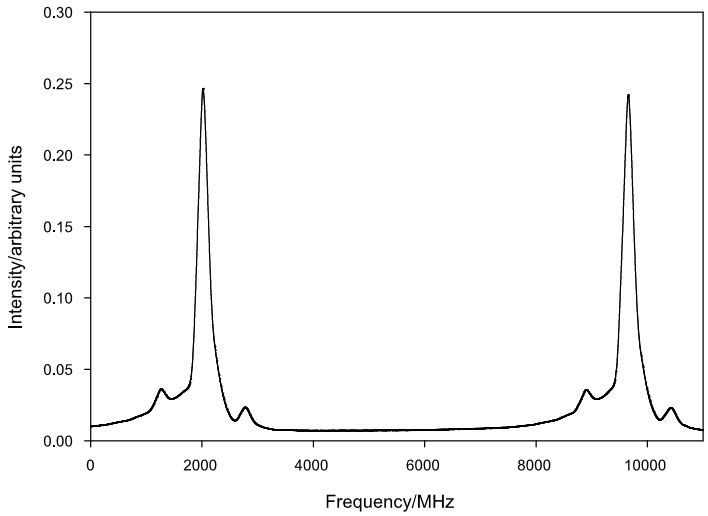

Figure 7.2: Optical spectrum analyser output as seen on an oscilloscope. The two carriers are present as the spectrum analyser is tuned across at least one free spectral range. The asymmetry in the peaks is due to the non-perfect alignment of the laser into the spectrum analyser. It can be seen that the sideband amplitude is $\approx 10\%$ of the carrier amplitude.

obtained on both lasers when the function generator is set to produce an output of 18dBm (the input to the SDL diode is attenuated by 6dBm). An example of the output from the spectrum analyser seen on an oscilloscope is shown in Fig. 7.2.

Once the r.f. drive is turned on, the stub tuners are adjusted to obtain maximum sideband amplitudes. This process of impedance matching also needs to be done each time a different r.f. frequency is chosen as the impedance matching properties are a function of frequency.

7.2 Frequency Locking of 397nm and 866nm Lasers

The 397nm and 866nm lasers are frequency locked using a side-of-fringe lock to one of the transmission fringes of a temperature stabilised optical cavity. Sidebands are applied to the latter and locking is achieved using one of the transmission fringes of the carrier. The setup for locking is shown in Fig. 7.3. Laser light is first sent through an optical isolator (OFR I0-3-397-LP for the 397nm lasers and Linos FR 850 for the 866nm lasers) whose function is to allow light propagation in one only direction. This stops any reflected light from the front face of the cavity from entering the diode as even a small amount of

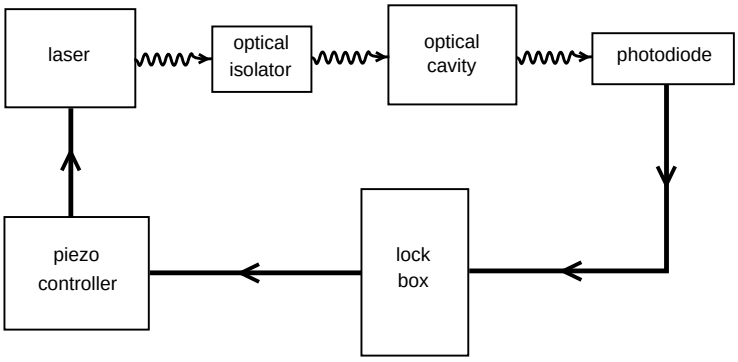

Figure 7.3: Schematic diagram showing the setup used for side-of-fringe locking of the diode lasers.

feedback is enough to affect the frequency stability of the laser [22]. The laser light is then sent into the optical cavity and the output signal is detected using a photodiode. This signal, whose amplitude is a function of the laser frequency, is then fed into the lock box on which a set point is chosen. The function of the lock box is to compare the input signal from the photodiode with the set point and produce an output to the laser piezo so as to minimise the difference in the signals. In this way, each time the laser frequency shifts away from the set point, it is driven back by the action of the piezo and stays locked. The most sensitive lock is achieved by setting the lock point to be at the steepest part of the transmission fringe since a slight change in the frequency will cause the greatest change in the cavity output signal.

7.2.1 Locking Electronics

The locking electronics for the 397nm lasers are commercially bought and have proportional (P), integral (I) and differential (D) adjustments. The ones for the 866nm lasers were homebuilt based on a design taken from [51]. This design only has a proportional adjustment. This is because it was used for locking a diode laser to a saturated absorption feature in rubidium. Since the frequency position of the reference stays constant with time, having just the proportional adjustment is sufficient. In our experiment, the locking set point is the transmission of an optical cavity. Since the frequency position of the reference is not fixed with time, an additional integration circuit in the locking electronics is required for a more stable lock. The modifications to the design based on [51] were done by a PhD. student, R. Hendricks.

The limiting factor in the speed of the lock in this setup is the rate at which the piezo can be driven. In this case, it is of the order of 1kHz. A faster lock

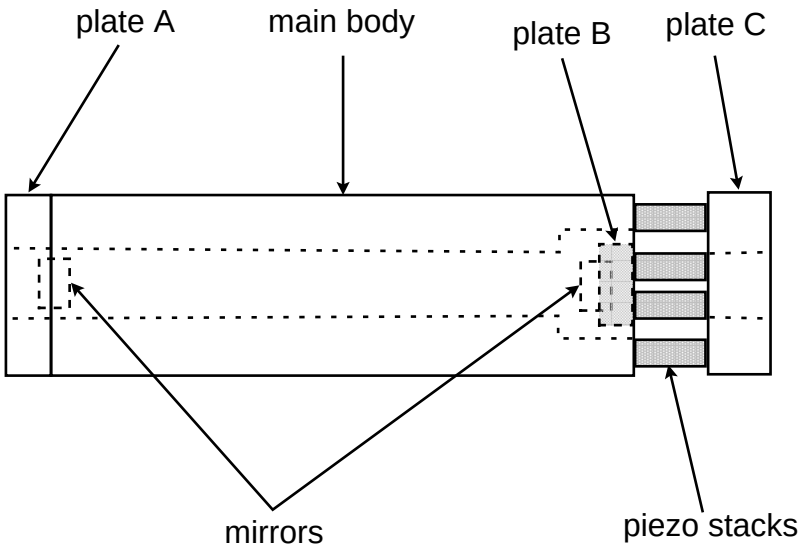

Figure 7.4: Design of the cavity showing how the pieces of Zerodur: main body and plate A, B, C, mirrors and piezo stacks are arranged to form an optical cavity. Only four piezo stacks are shown although there are six as two of them are not visible from this perspective.

can be achieved by feeding back into the laser current controller but was not implemented as the high frequency noise did not seem to be affecting the laser cooling. The aim of locking the lasers however, was to improve the long term frequency stability of the lasers.

7.2.2 Cavity Design

The optical cavities for the 397nm and 866nm lasers are of the same design. A schematic of the cavity is shown in Fig. 7.4. It is a tunable cavity made out of four separate pieces of Zerodur (HV Skan, standard quality Zerodur, nominal coefficient of expansion = 0), six piezo stacks (Lambda Photometrics P-802) and two mirrors. The mirrors for the 397nm cavity are from CVI with centre wavelength = 400nm, reflectivity = 95%, diameter = 1.27cm, thickness = 0.053cm, radius of curvature = 0.3m and are concave. The mirrors for the 866nm cavity are also from CVI and have exactly the same specifications except that the centre wavelength is 866nm. A central hole is drilled into all the pieces of Zerodur such that when arranged in the way shown in Fig. 7.4, a line of sight is created for the laser light to be sent through. Plate A has a recess made into it such that it holds one of the mirrors. Similarly, the other mirror is placed in a recess made into plate B. Plate B is then attached to plate C via three piezo

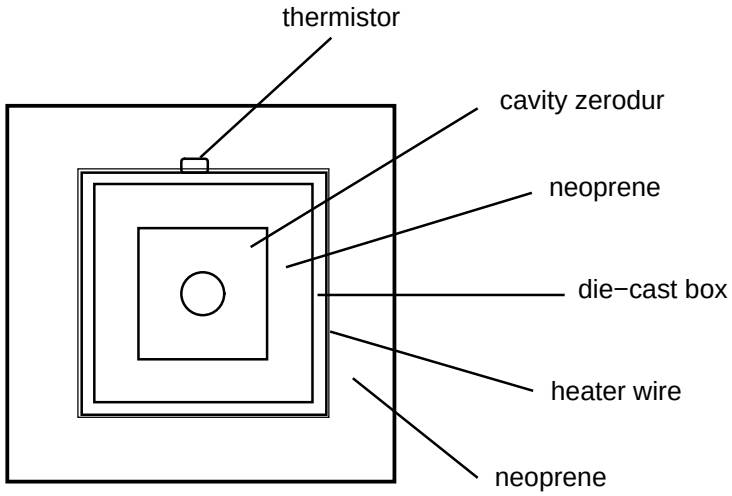

Figure 7.5: Cross section of the temperature controlled die-cast box for use with the optical cavities.

stacks and the latter is attached to the main body of the cavity by another three piezo stacks. This re-entrant design means that the sets of three piezo stacks act against each other as they expand and contract thermally thereby cancelling out their first order drift. A minimal amount of Araldite was used to attach the mirrors to the Zerodur and the plates of Zerodur to one another. For the cavity length to be tunable, three of the piezo stacks which connect plate C to the main body of the cavity are connected to a piezo driver (Physik Instrumente P863). The actual cavity length is $\approx$ 15cm which gives a free spectral range of $\approx$ 1GHz.

Although the cavity is made out of Zerodur which has a nominal coefficient of expansion of zero, the mirror and the Araldite used to glue the parts of the cavity together have a non-zero coefficient of expansion. Also, the re-entrant design assumes the piezo stacks are all identical. To minimise the drift of the cavity due to temperature changes, the cavity is placed inside a die-cast aluminium box that is temperature stabilised to 0.1°C. The spaces between the cavity and the walls of the box are filled with insulating neoprene. The outside of the box is then wrapped around with heater wire. A thermistor is also placed in thermal contact with one of the surfaces of the box. The whole box is wrapped with a layer of neoprene to provide further insulation from the environment. A cross-section of the temperature controlled box is shown in Fig. 7.5.

The heater wires and thermistor are part of a home-built temperature control circuit which provides stabilisation by way of heating the box when the temperature is below a set point. As there is no facility to actively cool the box,

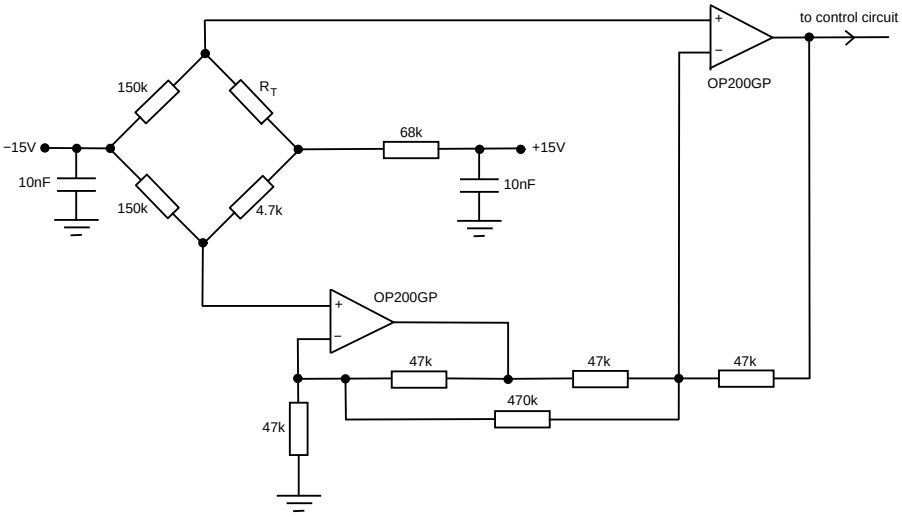

(a)

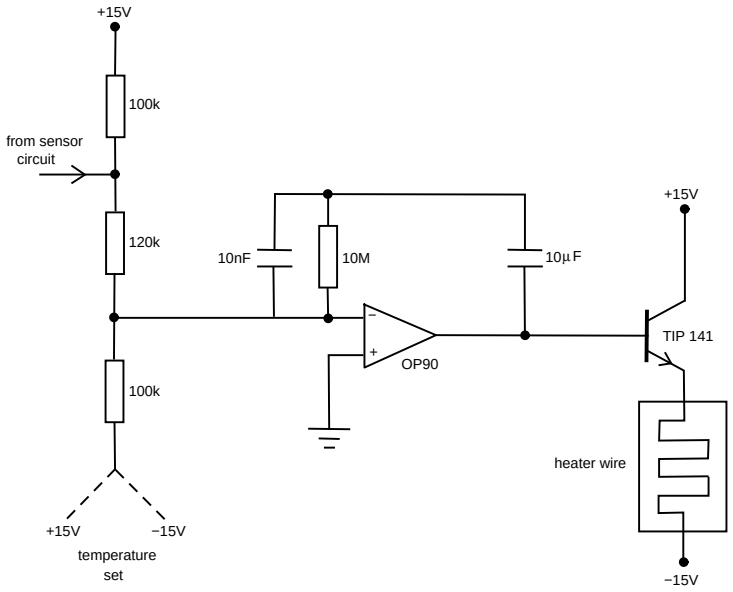

(b)

Figure 7.6: Circuit diagram of the temperature controller for the optical cavity. It consists of (a) the sensor circuit and (b) the control circuit, where the output from (a) is fed into (b).

the set point has to be above the ambient temperature for the stabilisation to work. Typically, this is set to $\approx 25°C$ with the ambient temperature $\approx 20°C$. The circuit diagram of the electronics for the temperature controller is shown in Fig. 7.6.

An estimate of the stability of the cavity against frequency drift was obtained as follows. A small cloud of ions were loaded and trapped in the Penning trap. The laser frequencies were then optimised to obtain maximum fluorescence and their frequencies locked to the cavities. It was found that there was only a 10-20% loss of fluorescence after a period of 30 minutes. We have measured the full-width at half maximum for a similar sized cloud of ions laser cooled in the Penning trap to be $\approx$ 80MHz. This gives an upper limit of the cavity drift rate as $\approx$ 80MHz/hour.

7.2.3 Mode Matching Into Cavities

Perfect mode matching of the lasers into the cavities would eliminate the existence of all other spatial modes of the cavity apart from the TEM 00 mode. A large transmission fringe is then obtained since all the light energy is concentrated onto one mode. This leads to a good signal to noise ratio when locking to the side of this fringe. Mode matching requires the laser beam waist to match that of the cavity mode. This can be accomplished by choosing an appropriate lens or a set of lenses that shape the beam before entering the cavity. In our case, two lenses were used as this arrangement has the added advantage of allowing the lens-to-cavity distance to be chosen. A computer program was written to facilitate this process making it easier to choose the appropriate lenses, especially when the additional constraint of lens-to-cavity distance was included.

Although there was the facility for perfect mode matching into the cavities, this was not done. The lack of perfect mode matching means that several distinct modes of the cavity are present. This is observed as several peaks in the transmission spectrum of the cavity where each peak corresponds to a mode of the cavity. Any one of these peaks can be used for locking as long as there is sufficient amplitude. This means that the cavity length only needs to be changed slightly before a lock point is located. This is advantageous as the change in cavity length should be kept to a minimum since the piezo stacks have a tendency to "creep" after a voltage is applied.

7.3 Mixing of $3^2D_{3/2}$ Levels

Attempts were made at mixing the $3^2D_{3/2}$ levels using microwave radiation which would reduce the number of lasers required to just four ($2 \times$ 397nm, 1

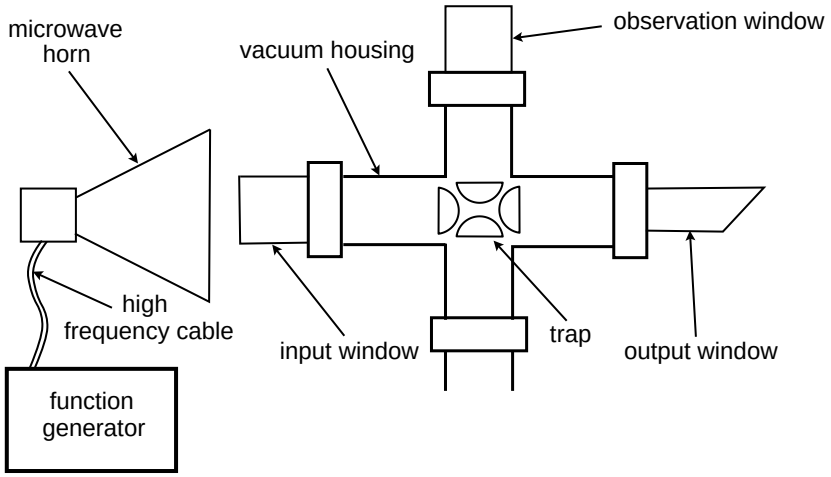

Figure 7.7: Setup used for shining microwave radiation into the trap. Here the horn is placed as close as possible to the input window of the vacuum system.

$\times$ 866nm and 1 $\times$ 854nm) for operation in the Penning trap. The microwave radiation was applied in two ways. The first was done by using a horn to direct the microwave radiation into the trap. The second method involved applying the microwave radiation directly onto one of the trap components. In the latter case, attempts were made by applying radiation onto one of the endcaps, spare oven and filament.

The setup used for applying microwave radiation by shining it into the trap is shown in Fig. 7.7. The microwave radiation was produced by a function generator (Agilent 83650L). It was then sent into the microwave horn using a high frequency cable (Testline 18 from M/A Com). The only possible areas for the radiation to enter the trap are through the input or output windows of the vacuum system. Therefore, the horn was placed as close as possible to either of these windows.

Applying microwaves onto the filament or spare oven was done by directly connecting the output of the function generator to the trap component. This was done using a high frequency cable with one end severed so that it could be soldered directly onto the pins of the high vacuum feedthrough connector. Applying microwaves onto one of the end caps is slightly more complicated as this causes the endcap to lose its connection to earth which is necessary at all times for the operation of the trap. However, a simple circuit was built as shown in Fig. 7.8 which allows the microwaves to be fed onto the end cap whilst still maintaining its connection to earth.

The method used to test the effectiveness of the microwave radiation in mixing the $3^2D_{3/2}$ levels is as follows. Ions are loaded in 0.78T Penning trap

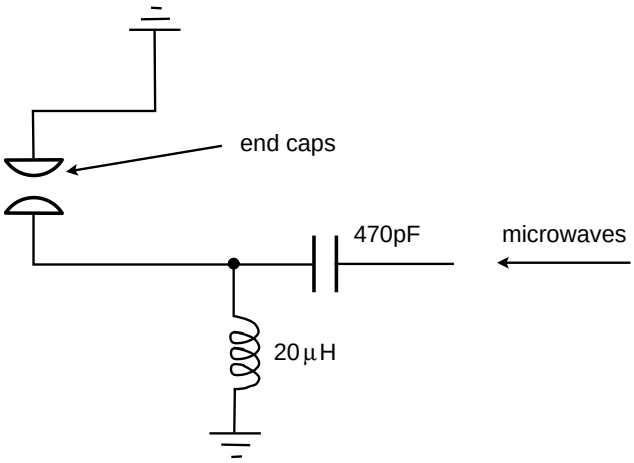

Figure 7.8: Setup used for applying microwaves onto one of the trap components.

and the fluorescence signal optimised. The repumping scheme used here involves the use of 2 × 397nm lasers and 4 × 866nm lasers. The 854nm was not used as it was still possible to obtain a significant amount of fluorescence even without the use of the 854nm laser. The microwave radiation at 8.72GHZ is then applied using either one of the two methods mentioned above. All but one of the 866nm lasers is blocked off from the trap. At this point, no fluorescence was observed for any of the two methods used to apply the microwaves. The microwave frequency was then scanned across ± 10% of the calculated frequency but this did not produce any fluorescence. A possible reason for the failure of the first method (use of the horn) is the lack of accessibility for the microwave radiation to enter the trap as the centre of the trap is "shielded" by apertures placed at the front and back which serve to reduce unwanted scattered laser light. One possible reason for the failure of the second method is that the impedance of the function generator was not matched to that of the trap components. This would require a stub tuner suitable for that operating frequency as well as a device for measuring the degree of impedance matching which were not available to us. Another possible reason for the failure of the two methods used is the instability of the magnetic field. This causes the separation of the Zeeman split states to fluctuate over time which means that the microwave radiation is not constantly in resonance with the transitions.

7.4 Driving of Motional Resonances

As was shown in Sec. 2.1.1 of Chap. 2, the motion of ions in the Penning trap is well defined (the motion is a superposition of the axial, magnetron and modified

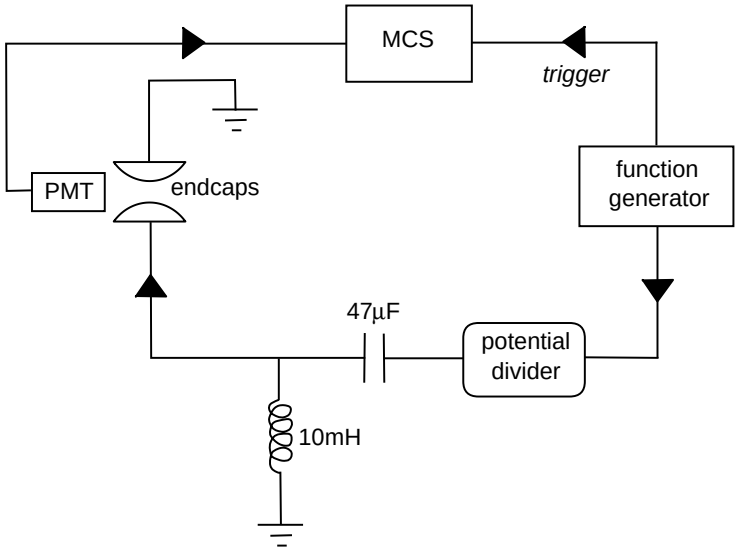

Figure 7.9: Schematic of setup used for driving of motional resonances.

cyclotron motions) with each motion having a defined oscillation frequency. These frequencies can be measured by applying a small oscillating external field applied to one of the endcaps and observing the fluorescence signal. When the frequency of the external drive coincides with one of the motional frequencies, the ions heat up and expand into larger orbits causing the fluorescence level to drop.

The motional frequencies that are of interest for the calibration of the magnetic field are the modified cyclotron and the magnetron frequencies. The sum of the two gives the true cyclotron frequency which is a function of the magnetic field only. Making this measurement at different magnet currents will then give a calibration of magnetic field vs. magnet current.

The setup used for driving the motional resonances is shown in Fig. 7.9. The external drive is provided by a function generator (HP 3325B) which is first fed into a potential divider before going into a simple circuit which allows the drive to be applied onto one of the endcaps while still maintaining its grounding. The other endcap is permanently grounded. The potential divider reduces the drive amplitude to 11% of its original value.

The method used to measure the motional frequencies is as follows. Ions are first loaded in a Penning trap. The lasers are set to operate in constant frequency mode and are optimised for maximum fluorescence. One of the 397nm lasers is then red detuned to the point where the fluorescence drops to half its maximum. The external drive is set to scan across a frequency range that includes one of

the motional frequencies of interest. This scan is also used to trigger the MCS software so that data is only accumulated once the scan is turned on. The results are shown in the next section.

7.4.1 Results

A trace with the magnetron resonance is shown in Fig. 7.10(a). This trace is a sum of 30 scans and obtained with a magnetic field of 0.78T, trap d.c. of 6V and a drive amplitude of 7.5mV (at the function generator). The position in frequency of the dip corresponds to the magnetron frequency. The dip in the fluorescence signal is due to the ions being knocked out into a larger orbit by the drive such that they are no longer in the laser beam. The asymmetry in the dip is very likely due to the laser cooling dynamics present. Once the drive is no longer in resonance, the ions that were knocked out into larger orbits are gradually cooled back into resonance with the laser radiation, hence the more gradual change in the increase in fluorescence. This technique was also used to obtain the axial frequency with one of the scans shown in Fig. 7.10(b). This trace is a sum of 10 scans and obtained with a magnetic field of 0.78T, trap d.c. of 6.7V and drive amplitude of 8.0mV (at the function generator). The dips occur at 52.5kHz and 174kHz for scans (a) and (b) respectively. The calculated values are 62.6kHz and 182kHz respectively. This difference is not surprising as the trap parameter R will differ from its theoretical value due to imperfections in the trap electrodes.

The calibration of the magnetic field vs. the magnet current is shown in Fig. 7.11. The calibration is only available from a magnetic field of 0.78T (trap bias $U_0 = 6V$) upwards as the method of acquiring this information required the operation of the Penning trap. The operation of the Penning trap requires a certain magnitude of magnetic field strength below which radial confinement cannot be achieved. This experiment required the use of four independent 866nm repumper lasers since it was not possible to generate sidebands at $\sim$ 1GHz (which is required at magnetic fields of $\sim$ 1T).

7.5 Trapping of Small Clouds: Towards Single Ca^+ Ions

The procedure for trapping small clouds of Ca^+ ions in an attempt to isolate single ions in the Penning trap is similar to that used for trapping single ions in the Paul trap. To reiterate, this involves loading a large cloud of ions and optimising the fluorescence signal before lowering the oven current in small steps to load progressively smaller clouds of ions. With each load, the fluorescence

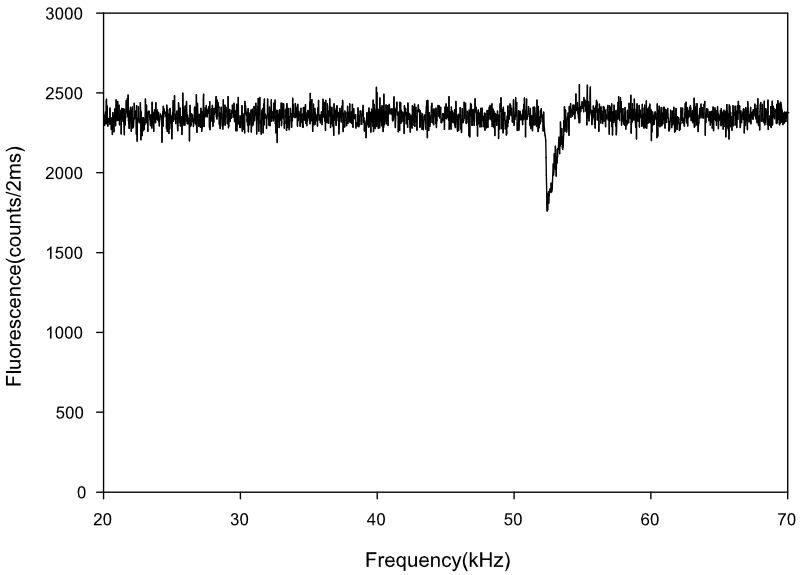

(a)

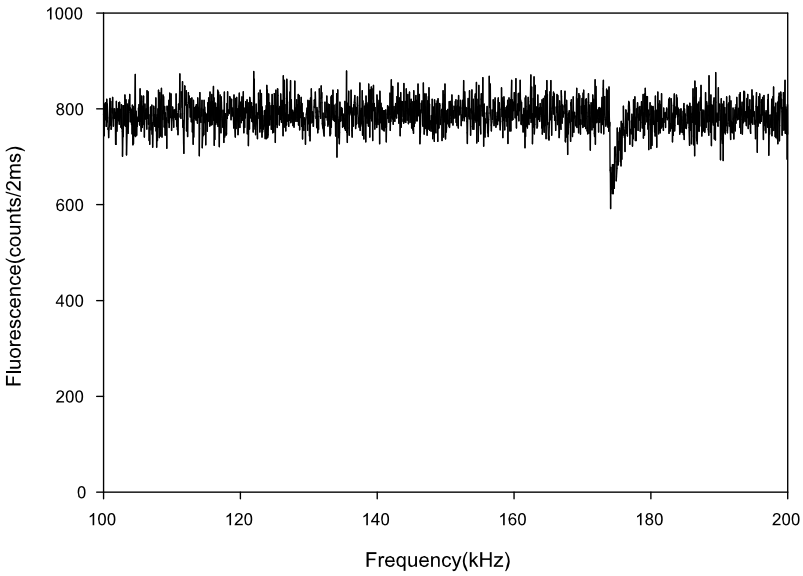

(b)

Figure 7.10: Trace showing resonance of (a) magnetron motion and (b) axial motion when driven with a scanning external field. In both traces the external field is scanned up in frequency.

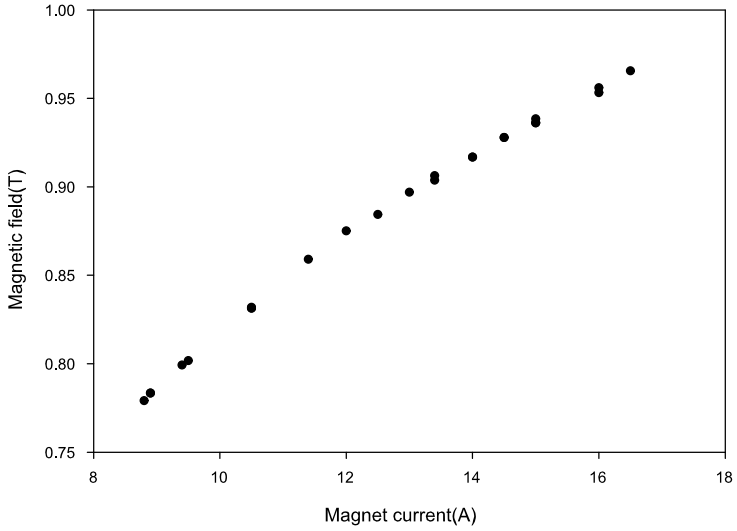

Figure 7.11: Calibration curve of magnetic field against magnet current.

is maximised by tuning the laser frequencies and adjusting the beam position of the lasers iteratively. Doppler cooling in the Penning trap however, requires the cooling beam to be offset away from the centre of the ion cloud in the radial plane (see Sec. 2.4 of Chap. 2). This adjustment is done before the first load in the Penning trap is performed. Once a large cloud is loaded, we found that moving the beams towards the centre of the trap increases the level of fluorescence with the maximum level obtained just slightly above the trap centre. Moving the beams across the centre of the trap so that they are below the trap centre causes the ions to heat out into larger orbits resulting in a sudden drop in fluorescence. The original signal level can be regained, provided none of the ions have escaped the potential well, by placing the beams above the centre of the trap and moving them back towards the centre.

If the trap is emptied and a similar sized cloud is to be loaded, the beam positions need to be displaced away from the trap centre in order to cool the hotter ions. If a smaller cloud is to be loaded we have found that the beams do not need to be displaced any further away from the trap centre. This is true because as the ion cloud gets smaller, the orbit also shrinks thereby negating the need of displacing the beam. On the contrary, we found that the beams need to be brought closer towards the trap centre to obtain maximum fluorescence after cooling has taken place.

The amount of laser power required to obtain maximum fluorescence de-

creases with the size of the ion cloud. This is essentially because the effective spatial extent of the laser beam is a function of the intensity of the beam. Therefore, it is possible to reduce the amount of laser power and still obtain maximum fluorescence if the size of the ion cloud is small. As much of the background on the PMT signal was due to the 397nm laser scatter, reducing their powers using neutral density filters improved the signal to background ratio. For example, we found that for a small cloud of $\sim$ 10-20 ions, the signal to background was best when a 3.2%T filter was used, reducing the laser power to $\approx 30\mu$W. Apart from improving the signal to background ratio, reducing the 397nm laser powers also narrowed the width of the cooling trace. The narrowing of the peak is an indication that with full laser power, the $4^2S_{1/2} \rightarrow 4^2P_{1/2}$ transition was power broadened. The 866nm laser powers were not reduced as they did not contribute to the background on the PMT signal. Also, since they only act as repumpers, there was no danger of heating by power broadening their respective transitions.

As the size of the ion cloud gets smaller and more filters are used, the level of fluorescence signal from the ions becomes more sensitive to laser frequency drifts. This necessitates frequency locking both the 397nm lasers and both the 866nm lasers. To frequency lock to a cavity, a strong transmission fringe from each of the four laser cavities is first located. This is done by tuning the length of the cavities using the piezo drivers. Once a strong fringe is found, it is parked on the correct side of the slope with respect to the set point before the locking is activated.

The test for presence of single ions in the Penning trap is done through the observation of quantum jumps. In the Paul trap, this is done by blocking off the 854nm laser and allowing the ASE from the 397nm laser to shelve the ions into the $3^2D_{5/2}$ state. However, operation in the Penning trap requires the filtering of the 397nm laser which reduces the ASE to the point that the shelving rate into the $3^2D_{5/2}$ state becomes close to zero. In order to observe quantum jumps, an 850nm laser is used to address the $3^2D_{3/2} \rightarrow 4^2P_{3/2}$ transition and the 854nm laser is blocked off. This drives the ions into the $4^2P_{3/2}$ level so that they can decay into the metastable $3^2D_{5/2}$ level.

7.5.1 Results

A typical Doppler cooling trace of a small cloud of ions in the Penning trap is shown in Fig. 7.12(a). Here, Doppler cooling was achieved by using 2 $\times$ 397nm, 4 $\times$ 866nm and 1 $\times$ 854nm laser. The oven current was set to 1.80A. The trace was done as a sum of 25 scans to improve the signal to noise ratio. The FWHM of the peak is 82MHz which gives an upper temperature limit of $\approx$

1K. In comparison, Fig. 7.12(b) shows a typical Doppler cooling trace obtained from a large cloud of ions (oven load at 2.00A). Note that the trace in (b) is a single scan while that in (a) is a summed one. The FWHM of the peak in (b) is 460MHz which corresponds to an upper temperature limit of $\approx$ 29K . The higher temperature in (b) is expected for a larger cloud as each ion will spend less time interacting with the laser resulting in the cloud being less efficiently cooled.

Quantum jumps of a small number of ions in the Penning trap is shown in Fig. 7.13(a). A trace with the full signal level (without quantum jumps) and the background level is shown in Fig. 7.13(b). The background was obtained by blocking off one of the 866nm lasers. The average fluorescence level without any quantum jumps is $\sim$ 16 counts/25ms on top of an average background level of $\sim$ 2counts/25ms. It can be seen that the noise in scan (a) is greater than in scan (b). Furthermore, the signal level in scan (a) drops to the background level and rises to the full signal level on several occasions. This can only be possible if small numbers of ions are present as the likelihood for all the ions to be in the "off" or "on" state at the same time decreases with the number of ions.

In order to determine the number of ions present, the noise in scan (a) was statistically analysed. The details of the analysis is given in Appendix B. The analysis involves finding the values of several parameters in order to determine the number of ions. The parameters for the trace in Fig. 7.13(a) are given in Table 7.1 along with the calculated number of ions, N. The definitions of these parameters are defined in Appendix B. From the analysis we can infer that two ions are present in scan (a). This means that the signal per ion in the Penning trap is $\sim$ 320 counts per second. The maximum scattering rate from a single Ca^+ ion in the presence of a magnetic field is $A/4 \approx 3.7\times10^7$, where A is the Einstein A coefficient for the $4^2S_{1/2} \rightarrow 4^2P_{1/2}$ transition. The reason for the factor of 1/4 was explained earlier in Sec. 5.5.1 of Chap. 5. The expected maximum signal from a single ion in the Penning trap is complicated by the motion of the ion in the trap. As mentioned in Sec. 2.4 of Chap. 2, the presence of the magnetron motion requires the cooling laser beam to be offset from the centre of ion orbit so that energy is only added and not removed from the magnetron motion. This causes a reduction in the maximum fluorescence signal that can be observed since the ion is not constantly in the laser beam. Simulations of laser cooling of single ions in the Penning trap have been performed by D.C. Wilson [78] where it was found that the signal is reduced by a factor of 7 because of the complications associated with cooling the magnetron motion. Taking into account these factors, the maximum fluorescence that can be observed from a single ion in the Penning trap is given by

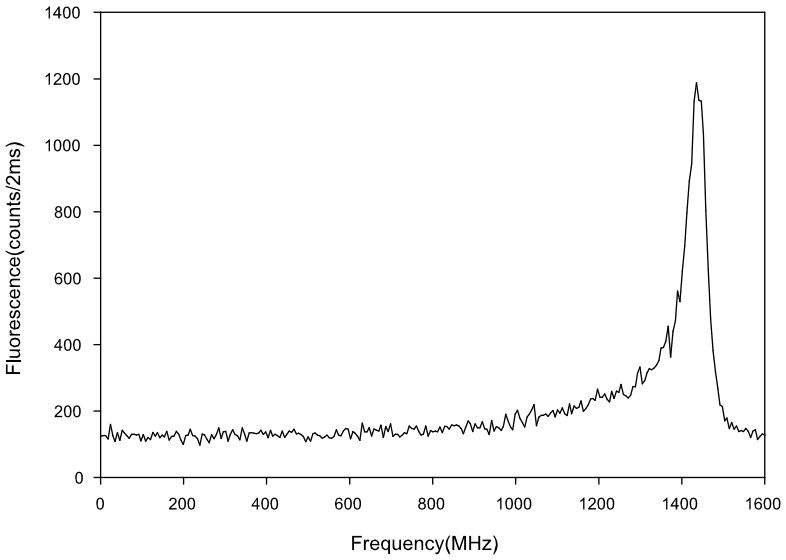

(a)

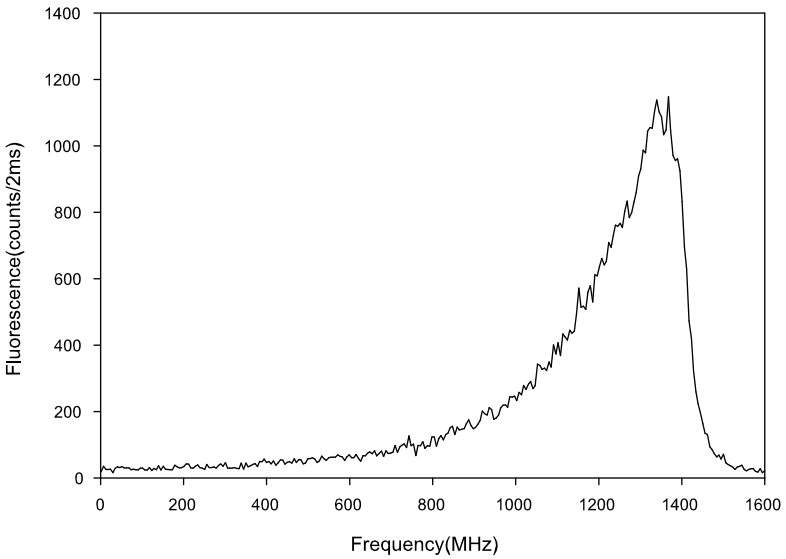

(b)

Figure 7.12: Doppler cooling trace of a (a) small cloud of ions (FWHM = 82MHz) and (b) large cloud of ions (FWHM = 460MHz) in a Penning trap.

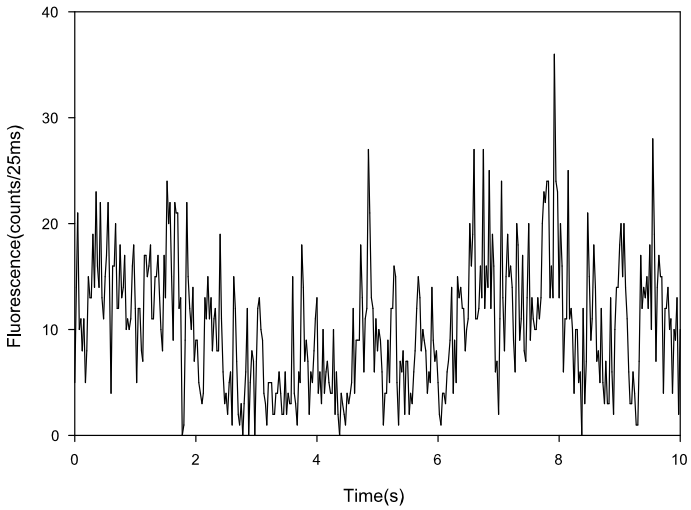

(a)

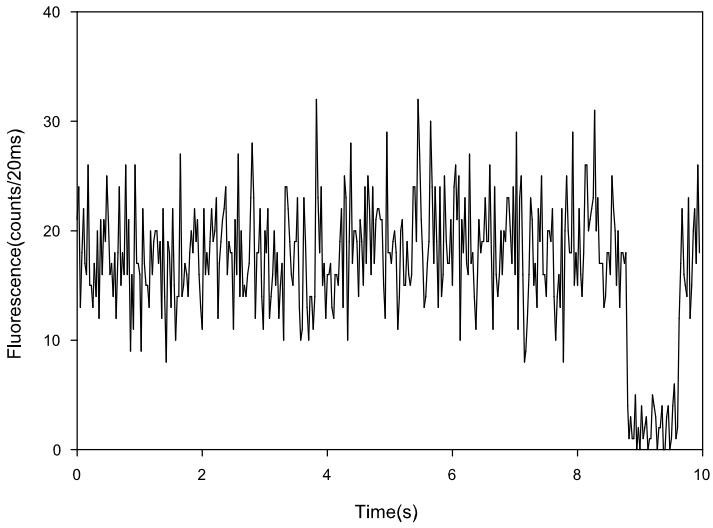

(b)

Figure 7.13: (a) Quantum jumps of probably 2 Ca^+ ions in a Penning trap (b) Fluorescence level without quantum jumps and background level.

X_1	2.000
X_2	10.35
X_3	17.53
Y_1	2.547
Y_2	37.58
Y_3	20.09
p	0.5376
Q	0.3907
N	2.201

Table 7.1: Values of the parameters obtained for the trace shown in Fig. 7.13(a).

$$\begin{aligned} S_{Penmax} &= \xi \times A/4 \times \frac{1}{7} \\ &= 1.7 \times 10^{-4} \times 3.7 \times 10^{7} \times \frac{1}{7} \\ &\approx 900\text{counts/s}, \end{aligned} \tag{7.1}$$

where S_{Penmax} is the maximum signal from a single ion in the Penning trap, ξ is the detection efficiency (see Sec. 4.3.2 of Chap. 4) and A is the Einstein A coefficient.

The actual signal level observed is nearly a factor of three lower than the expected value. This difference is not surprising as some of the values used in the calculation for the expected signal were only estimates. However, the observation of quantum jumps of two ions in the Penning trap is a good indication that there is no fundamental problem with the laser cooling scheme used for Ca^+ in the Penning trap. In other words, the ions are being efficiently laser cooled in a closed cycle with no loss of population into one of the metastable states.

7.6 Future Work

So far, we have been unable to trap single Ca^+ ions in the Penning trap. This is thought to be mainly due to the peculiar properties of the magnetron motion. This motion necessitates offsetting the beam position spatially from the centre of the ion orbit which results in the reduction of signal since the ion is not constantly in the laser beam. Also, this means that the ions are less efficiently cooled. In light of this, the first improvement to be made to the current system will be to implement axialisation of the Ca^+ ions. This technique involves coupling the magnetron motion of the ion to the cyclotron motion by a

weak external electric field oscillating at the true cyclotron frequency [65]. This allows the magnetron motion to be cooled more efficiently and allows lower temperatures to be reached. Axialisation also removes the need of having the laser cooling beam spatially offset from the centre of the ion orbit which should result in an increase in the observed signal.

Another immediate improvement that can be made to the setup is in the trap loading technique. The procedure currently used involves loading progressively smaller clouds of ions into the trap by reducing the oven current in steps. This technique requires a delay of about 5 minutes between each load to allow for the oven to cool down to the ambient temperature. Otherwise, the higher initial temperature of the oven leads to inconsistencies in the cloud size. It would therefore be useful to investigate other loading techniques which would involve less dead time. One possibility would be to leave the oven on constantly but on a very low current setting such that only a small flux of atoms is being emitted. Here, loading the trap would only require the filament to be turned on for the amount of time needed to ionise the atoms. Loading a sinlge ion would require the oven current to be adjusted so that the amount of atomic flux being emitted only results in a single ion loaded.

The longer term goals of this project are to perform sideband cooling of Ca^+ ions in a Penning trap and to quantify decoherence rates. In order to achieve this goal, two important milestones need to be reached first. The first is the frequency stabilisation and bandwidth narrowing of a Titanium:Sapphire laser which will be used to address the qubit ($4^2S_{1/2} \rightarrow 3^2D_{5/2}$) transition. Work on this laser is currently in progress. The second milestone involves the modification of an already existing trap. This trap is unique in that it is built especially for use with a superconducting magnet. A superconducting magnet is used as it provides a higher and much more stable magnetic field which is required for the sideband cooling experiments.

Chapter 8

Conclusions

The work described in this thesis is part of a long term research plan whose aim is to study decoherence effects in the Penning trap. Results from this investigation should provide useful information about the practicality of the Penning trap as a means to implement quantum information processing (QIP). A positive result could lead to a re-direction in the efforts to realise a physical quantum computer as most of the efforts undertaken so far have concentrated on the use of the Paul trap.

To this end, we have successfully demonstrated the trapping and laser cooling of Ca^+ ions in the Penning trap. This represents an important milestone especially since this is the first time Ca^+ ions have been successfully trapped and laser cooled in the Penning trap. Although the trapping and laser cooling of Ca^+ in the Paul trap has been widely demonstrated, trapping and laser cooling in the Penning trap has not yet been demonstrated prior to this due to the non-trivial laser cooling scheme involved as a result of the Zeeman splittings. Our laser cooling scheme involves the use of two 397nm lasers, two 866nm lasers with each of their input currents frequency modulated to produce sidebands and a single 854nm laser. Other important results that were achieved along the way were, the trapping and cooling of Ca^+ ions in the Paul and the combined trap. Operation in the Paul trap allowed the experimental apparatus to be characterised and calibrated before operation in the more demanding environment of the Penning trap was attempted. The combined trap was used as a means to set the laser wavelengths to their correct values for operation in the Penning trap. This method of setting the laser wavelengths essentially involves tuning the laser wavelengths in step with the increase of the magnetic field until the field was strong enough for the operation of the Penning trap. This should not be necessary in the future as a high precision wavemeter is currently being built which should allow the laser wavelengths to be set directly.

We are currently pursuing the goal of routinely trapping and laser cooling single Ca^+ ions in the Penning trap. Initial results show that small numbers of Ca^+ ions (probably two) have been successfully trapped in the Penning trap. These results prove that there is no fundamental problem in the laser cooling scheme used here i.e. no population is lost into a dark state. Although no single ions have been successfully trapped yet, these initial attempts have allowed us to identify areas that need to be improved in order to trap single Ca^+ ions in the Penning trap.

Appendix A

Temperature Measurement of Ions

The temperature of the trapped ions can be inferred from the profile of the fluorescence signal obtained by scanning the 397nm (cooling laser) from below the resonance of the cooling transition up to line centre. An example of this profile is shown in Fig. A.1. This is the fluorescence signal from a small cloud of ions in a Penning trap and was obtained by accumulating the signal over 25 scans. The solid curve is an attempt to fit the fluorescence profile with a Gaussian lineshape. A Gaussian profile is used as the profile is pre-dominantly Doppler broadened. However, the fit is poor because of the presence of laser cooling dynamics. The dynamical process is present due to the method used to cool the ions. Here, the frequency of the 397nm laser is scanned from below resonance up to line centre which results in the ions only being cooled for the fraction of time that the 397nm laser is on resonance. During the time when the 397nm laser is not on resonance, only weak laser cooling is present. This causes the ions heat up slightly which results in a broader Doppler width. Hence the profile of the fluorescence has a wider Doppler width at the wings but quickly becomes narrower as soon as cooling is effected. As the fit is so poor and since this method of measuring the temperature is only intended to give an upper limit, the temperature is measured directly from half-width at half maximum (HWHM) of the fluorescence profile. For a Doppler broadened profile, the relationship between the temperature and FWHM (the FWHM is twice the HWHM) is given as

$$T = \frac{\Delta\omega_{1/2}^2 A}{[\omega_0(7.16 \times 10^{-7})]^2}, \tag{A.1}$$

where T is the temperature, $\Delta\omega_{1/2}$ is the FWHM, A is the atomic mass and ω_0 is the line centre frequency. For Fig. A.1, $\Delta\omega_{1/2}$ measured directly from the fluorescence profile gives 82MHz which corresponds to an upper temperature limit of $\approx$ 1K. Here, the natural linewidth has not been accounted for. This is another factor which contributes to the overestimation of the temperature.

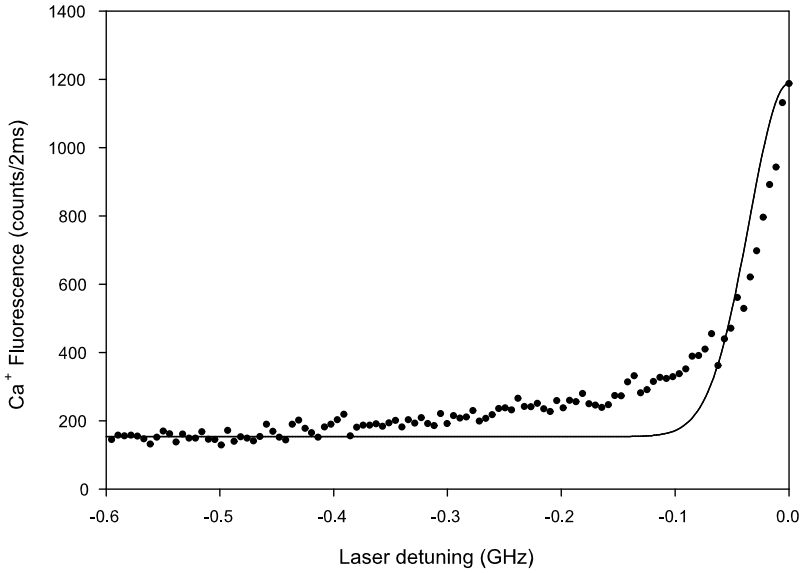

Figure A.1: An example of a fluorescence signal trace fitted to a Gaussian profile for a temperature measurement.

Appendix B

Statistical Analysis of Quantum Jump Fluorescence Trace

If small numbers of ions are present in the trap, the number of ions present can be inferred from the fluorescence signal of ions undergoing quantum jumps. The fluorescence level obtained during the process of quantum jumps will in principle exhibit distinct steps with each step corresponding to an ion being in the "on" state. Therefore the number of steps present indicates the number of ions present. This can usually be inferred from the fluorescence signal by eye but can be inaccurate in situations when the signal to noise ratio is poor. An alternative method of determining the number of ions present is by means of statistical analysis. This method is described in more detail below.

Let us consider the case when only a single ion is present. Let us also assume the absence of a background level and that the signal is noise free. The fluorescence signal from the ions will consist of two distinct levels: a zero level when the ions are in the "off" state and a level which we shall call x_0, corresponding to the "on" state. If the ion is in the "on" state a proportion p of the time then the mean of the signal is

$$\overline{x_1} = x_0 p, \tag{B.1}$$

the mean squared signal is

$$\overline{x_1^2} = x_0^2 p, \tag{B.2}$$

and the variance is

$$\begin{aligned}\sigma_1^2 &= \overline{x_1^2} - (\overline{x_1})^2 \\ &= x_0^2 p - x_0^2 p^2 \qquad \text{(B.3)} \\ &= x_0^2 p(1-p), \qquad \text{(B.4)}\end{aligned}$$

Now consider the case when two ions are present. The mean of the signal is

$$\begin{aligned}\overline{x_2} &= 2x_0 p^2 + 2x_0 p(1-p) \\ &= 2x_0 p, \qquad \text{(B.5)}\end{aligned}$$

and the mean squared signal is

$$\begin{aligned}\overline{x_2^2} &= 4x_0^2 p^2 + 2x_0^2 p(1-p) \\ &= 2x_0^2 p^2 + 2x_0^2 p \\ &= 2x_0^2 p(1+p), \qquad \text{(B.6)}\end{aligned}$$

and the variance is

$$\begin{aligned}\sigma_2^2 &= 2x_0^2 p(1+p) - 4x_0^2 p^2 \\ &= 2x_0^2 p - 2x_0^2 p^2 \\ &= 2x_0^2 p(1-p). \qquad \text{(B.7)}\end{aligned}$$

In general for N ions we find:

$$\begin{aligned}\overline{x_N} &= N x_0 p \\ \overline{x_N^2} &= N x_0^2 p[1 + (N-1)p] \\ \sigma_N^2 &= N x_0^2 p(1-p). \qquad \text{(B.8)}\end{aligned}$$

The expressions above apply assuming the signal is noise free. In the presence of noise, the expression for the mean remains the same. However, the variance of the signal will have a contribution due to the noise. The variance of the noisy signal can be expressed as

$$\sigma_N^2 = N x_0^2 p(1-p) + N x_0 p. \qquad \text{(B.9)}$$

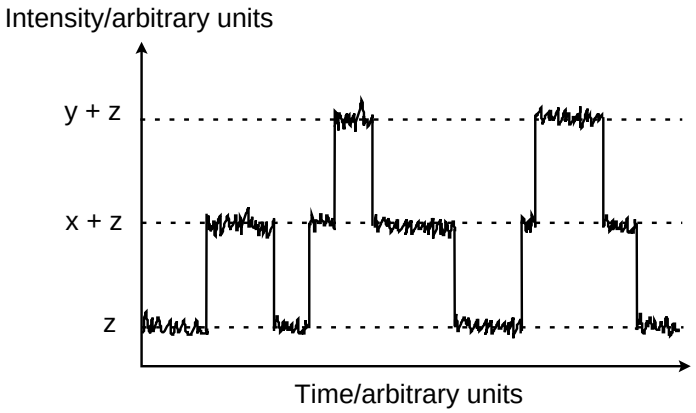

Figure B.1: A hypothetical example of a fluorescence trace of two ions undergoing quantum jumps.

The first term of the right hand side is just the variance of the noise free signal. The second term represents the contribution from the noise which is also the expression derived for the mean of the noise free signal. This is true since the noise is governed by Poissonian statistics, which means that the variance is equal to the mean. Let us define the parameter Q as

$$Q = \frac{\sigma^2 - \overline{x}}{\overline{x}^2}. \tag{B.10}$$

This can be can written as

$$\begin{aligned} Q &= \frac{N x_0^2 p(1-p)}{N^2 x_0^2 p^2} \\ &= \frac{(1-p)}{pN}. \end{aligned} \tag{B.11}$$

We can re-arrange Eq. B.11, so that

$$N = \frac{(1-p)}{pQ}. \tag{B.12}$$

Eq. B.12 allows us to find the value of N given the values of p and Q. The value of p can be easily found as it is the ratio of the average signal with quantum jumps to the average signal without quantum jumps. The value of Q can be calculated from experimental data using Eq. B.10. However, the experimental data contains information about the background level which was not taken into account in the treatment above. In order to use the experimental data in the equations above, the data needs to be corrected for the background.

X_1	18.77
X_2	26.96
X_3	61.42
Y_1	21.08
Y_2	165.4
Y_3	122.5
p	0.1920
Q	2.031
N	2.072

Table B.1: Values of the parameters obtained for the trace shown in Fig. B.2. The value of N is ~ 2 which is expected.

In the presence of background, the fluorescence trace will look something like Fig. B.1. Here, z represents the background, $z+x$ represents the real signal (i.e. signal + background) with quantum jumps and $z+y$ represents the real signal without quantum jumps. Let us also represent the average of the background as X_1, the average of the real signal with quantum jumps as X_2 and the average of the real signal without quantum jumps as X_3. Likewise, we can represent their respective variances as Y_1, Y_2 and Y_3. Since p is ratio of the average signal with quantum jumps to the average signal without quantum jumps, it can be written as

$$p = \frac{X_2 - X_1}{X_3 - X_1}. \tag{B.13}$$

Likewise, from Eq. B.10, Q can be re-written as

$$Q = \frac{(Y_2 - Y_1) - (X_2 - X_1)}{(X_2 - X_1)^2}. \tag{B.14}$$

The values of p and Q can then be used to find the value of N using Eq. B.12.

An example of how the number of ions are statistically inferred from a genuine fluorescence trace is given here. Fig. B.2 shows quantum jumps of ions in a Paul trap. It can be inferred even without the aid of statistical analysis that two ions are present due to the presence of two distinct steps in the fluorescence signal. Analysis of this trace using the treatment described earlier should therefore confirm that the two ions are present.

The parameters, X_1, X_2, X_3, Y_1, Y_2 and Y_3 along with the corresponding values of p, Q and N for the trace in Fig. B.2 are given in the Table B.1. It can be seen that the value of N obtained is ≈ 2.

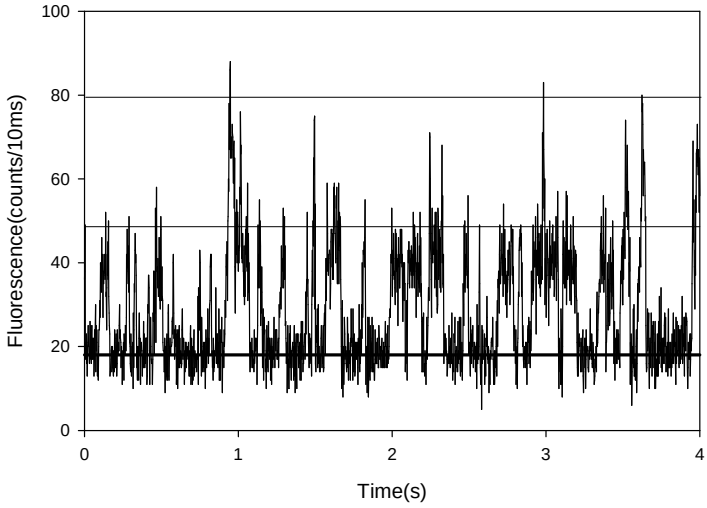

Figure B.2: Fluorescence trace of two ions undergoing quantum jumps in a Paul trap.

Bibliography

[1] W. Alt, M. block, V. Schmidt, t. Nakamura, P. Seibert, X. Chu, and G. Werth. Shifts of the 3D-4P transitions in different isotopes of positive calcium ions. *J. Phys. B.*, 30:L677–L681, 1997.

[2] J. Andre. Buffer gas cooling model. *J. Physique*, 37:719, 1976.

[3] A.S. Arnold, J.S. Wilson, and M.G. Boshier. A simple extended-cavity diode laser. *Rev. Sci. Inst.*, 69:1236–1239, 1998.

[4] C.H.W. Barnes, J.M. Shilton, and A.M. Robinson. Quantum computation using electrons trapped by surface acoustic waves. *Phys. Rev. B.*, 62:8410–8419, 2000.

[5] D.J. Bate. *Studies of Trapped and Laser Cooled Magnesium Ions.* PhD thesis, Imperial College, University of London, 1991.

[6] D.J. Bate, K. Dholakia, R.C. Thompson, and D.C. Wilson. Ion oscillation frequencies in a combined trap. *J. Mod. Opt.*, 39:305–316, 1992.

[7] P. Benioff. *J. Stat. Phys.*, 22:563, 1980.

[8] P. Benioff. Quantum mechanical hamiltonian models of Turing machines. *J. Stat. Phys.*, 29:515–546, 1982.

[9] C.H. Bennett. Logical reversibility of computation. *IBM J. Res. Develop.*, 17:525–532, 1973.

[10] J.C. Bergquist, S.R. Jefferts, and D.J. Wineland. Time measurement at the millennium. *Physics Today*, 54:37–42, 2001.

[11] M. Block, A. Drakoudis, H. Leuthner, P. Seibert, and G. Werth. Crystalline ion structures in a Paul trap. *J. Phys. B*, 33:L375–L382, 2000.

[12] M. Block, O. Rehm, P. Seibert, and G. Werth. $3d^2D_{5/2}$ lifetime in laser cooled Ca^+: Influence of cooling laser power. *Eur. Phys. J. D*, 7:461–465, 1999.

[13] J.J. Bollinger, D.J. Heinzen, and W.M. Itano. Test of the liearity of quantum-mechanics by r.f. spectroscopy of the Be-9^+ ground-state. *Phys. Rev. Lett.*, 63:1031–1034, 1989.

[14] D. Bouwmeester, J.-W. Pan, M. Daniell, H. Weinfurter, and A. Zeilinger. Observation of three-photon Greenberger-Horne-Zeilinger entanglement. *Phys. Rev. Lett.*, 82:1345–1349, 1999.

[15] G. Brassard. Searching a quantum phone book. *Science*, 275:627–628, 1997.

[16] G.K. Brennen, C.M. Caves, P.S. Jessen, and I.H. Deutsch. Quantum logic gates in optical lattices. *Phys. Rev. Lett.*, 82:1060–1063, 1999.

[17] A.R. Calderbank. Good quantum error-correcting codes exist. *Phys. Rev. A.*, 54:1098–1105, 1996.

[18] D.A. Church. Collision measurements and excited-level lifetime measurements on ions strored in Paul, Penning and Kingdon ion traps. *Phys. Rep.*, 228:253–358, 1993.

[19] J. I. Cirac and P. I. Zoller. Quantum computations with cold trapped ions. *Phys. Rev. Lett.*, 74:4091–4094, 1995.

[20] D.G. Cory, A.F. Fahmy, and T.F. Havel. *Proc. of the Fourth Workshop on Physics and Computation*, 1996.

[21] D.G. Cory, A.F. Fahmy, and T.F. Havel. *Proc. Natl. Acad. Sci. USA*, (94):1634, 1997.

[22] B. Dahmani, L. Hollberg, and R. Drullinger. Frequency stabilization of semiconductor-lsaer by resonant optical feedback. *Opt. Lett.*, 12:876–878, 1987.

[23] H.G. Dehmelt. Radiofrequency spectroscopy of stored ions. I: Storage. *Adv. At. Mol. Phys.*, 3:53, 1967.

[24] H.G. Dehmelt. Radiofrequency spectroscopy of stored ions. II: Spectroscopy. *Adv. At. Mol. Phys.*, 5:109, 1969.

[25] D. Deutsch. Quantum-theory, the Church-Turing principle and the universal quantum computer. *P. Roy. Soc. Lond. A*, 400:97–117, 1985.

[26] D. Deutsch. Quantum computational networks. *P. Roy. Soc. Lond. A.*, 425:73–90, 1989.

[27] F. Diedrich, J.C. Berguist, W.M. Itano, and D.J. Wineland. Laser cooling to the zero-point energy of motion. *Phys. Rev. Lett.*, 62:403–406, 1989.

[28] D.P. Divincenzo. Quantum computation. *Science*, 270:255–261, 1995.

[29] P. Domokos, J.M. Raymond, M. Brune, and S. Haroche. Simple cavity-QED 2-bit universal quantum logic gate - the principle and expected performances. *Phys. Rev. A*, 52:3554–3559, 1995.

[30] A. Ekert and R. Jozsa. Quantum computation and Shor's factoring algorithm. *Rev. Mod. Phys.*, 68:733–753, 1996.

[31] D.G. Enzer et. al. Experimental impplementation of quantum computation '01. 2001.

[32] R. P. Feynman. Simulating physics with computers. *Int. J. Theor. Phys.*, 21:467–488, 1982.

[33] R.P. Feynman. Quantum mechanical computers. *Found. Phys.*, 16:507–531, 1986.

[34] N.A. Gershenfeld and I.L. Chuang. Bulk spin-resonance quantum computation. *Science*, 275:350–356, 1997.

[35] P.K. Ghosh. *Ion Traps.* Oxford University Press, 1995.

[36] P. Grangier, G. Reymond, and N. Schlosser. Implementations of quantum computing using cavity quantum electrodynamics schemes. *Forts. Phys.*, 48:859–874, 2000.

[37] L.K. Grover. Quantum mechanics helps in searching for a needle in a haystack. *Phys. Rev. Lett.*, 79:325–328, 1997.

[38] S. Gulde, M. Riebe, G.P.T. Lancaster, C. Becher, J. Eschner, H. Haffner, F. Schmidt-Kaler, I.L. Chuang, and R. Blatt. Implementing the Deutsch-Jozsa algorithm on an ion-trap quantum computer. *Nature*, 421:48–50, 2003.

[39] M.H. Holzscheiter. Cooling of particles stored in electromagnetic traps. *Phyisica Scripta*, T22:73–78, 1988.

[40] G.Z.K. Horvath. *Dynamics and laser cooling of ions stored in a Penning trap.* PhD thesis, Imperial College, University of London, 1995.

[41] R.J. Hughes, D.F.V. James, E.H. Knill, R. Laflamme, and A.G. Petschek. Decoherence bounds on quantum computation with trapped ions. *Phys. Rev. Lett.*, 77:3240–3243, 1996.

[42] W.M. Itano, D.J. Heinzen, J.J. Bollinger, and D.J. Wineland. Quantum Zeno effect. *Phys. Rev. A*, 41:2295–2300, 1990.

[43] W.M. Itano and D.J. Wineland. Laser cooling of ions strored in harmonic and penning traps. *Phys. Rev. A*, 25:35–54, 1982.

[44] D.F.V. James. Quantum dynamics of cold trapped ions with application to quantum computation. *App. Phys. B.*, 66:181–190, 1998.

[45] S.R. Jefferts, C.R. Monroe, A.S. Barton, and D.J. Wineland. A Paul-trap apparatus for optical frequency standards. *IEEE Transactions on Instrumentation and Measurement*, 44:148, 1995.

[46] B.E. Kane. A silicon-based nuclear spin quantum computer. *Nature*, 393:133–137, 1998.

[47] D. Kielpinski, C. Monroe, and D.J. Wineland. Architecture for a large-scale ion-trap quantum computer. *Nature*, 417:709–711, 2002.

[48] M. Kretzschmar. Particle motion in a Penning trap. *Eur. J. Phys.*, 12:240–246, 1991.

[49] D.J. Larson, J.C. Bergquist, J.J. Bollinger, W.M. Itano, and D.J. Wineland. Sympathetic cooling of trapped ions: A laser-cooled two species nonneutral ion plasma. *Phy. Rev. Lett.*, 57:70–73, 1986.

[50] G.-Z. Li, R. Poggiani, G. Testera, G. Torelli, and G. Werth. Antihydrogen production in a combined trap. *Hyperfine Interactions*, 76:343, 1993.

[51] K.B. MacAdam, A. Steinbach, and C. Wieman. A narrow-band tunable diode-laser system with grating feedback, and a saturated absorption spectrometer for Cs and Rb. *Am. J. Phys.*, 60:1098–1111, 1992.

[52] N.W. McLachlan. *Thoery and applications of Matthieu functions*. Clarendon Press, Oxford, 1947.

[53] K. Molmer and A. Sorensen. Multiparticle entanglement of hot trapped ions. *Phys. Rev. Lett.*, 7:1835–1838, 1999.

[54] C. Monroe, D.M. Meekhof, B.E. King, W.M. Itano, and D.J. Wineland. Demonstration of a fundamental quantum logic gate. *Phys. Rev. Lett.*, 75:4714–4717, 1995.

[55] C. Monroe, D.M. Meekhof, B.E. King, S.R. Jefferts, W.M. Itano, D.J. Wineland, and P. Gould. Resolved-sideband Raman cooling of a bound atom to the 3D zero-point energy. *Phys. Rev. Lett.*, 75:4011–4014, 1995.

[56] H.C. Nägerl, D. Leibfried, H. Rohde, G. Thalhammer, J. Eschner, F. Schmidt-Kaler, and R. Blatt. Laser addressing of individual ions in a linear ion trap. *Phys. Rev. A*, 60:145–148, 1999.

[57] W. Neuhauser, M. Hohenstatt, P.E. Toschek, and H. Dehmelt. Optical-sideband cooling of visible atom cloud confined in parabolic well. *Phys. Rev. Lett.*, 41:233–236, 1978.

[58] W. Paul and H. Steinwedel. Quadrupole mass filter. *Z. Naturforforsch*, A8:448, 1953.

[59] H.F. Powell, D.M. Segal, and R.C. Thompson. Axialisation of laser cooled magnesium ions in a penning trap. *Phys. Rev. Lett.*, 89:093003, 2002.

[60] R. Rivest, A. Shamir, and L. Adleman. On digital signatures and public-key cryptosystems. *MIT Laboratory for Computer Science, Technical Report, MIT/LCS/TR-212*, 1979.

[61] C.H. Roos, T.H. Zeiger, H. Rohde, H.C. Nagerl, J. Eschner, D. Liebfried, F. Schmidt-Kaler, and R. Blatt. Quantum state engineering on an optical transition and decoherence in a Paul trap. *Phys. Rev. Lett.*, 83:4713–4716, 1999.

[62] M.A. Rowe, A. Ben-Kish, B. Demarco, D. Liebfried, V. Meyer adn J. Beall, J. Britton, J. Hughes, W.M. Itano, B. Jelenkovic, C. Langer, T. Rosenband, and D.J. Wineland. Transport of quantum states and separation of ions in a dual rf ion trap. *Quan. Info. and Comp.*, 2:257, 2002.

[63] M.A. Rowe, D. Kielpinski, V. Meyer, C.A. Sackett, W.M. Itano, C. Monroe, and D.J. Wineland. Experimental violation of a Bell's inequality with efficient detection. *Nature*, 409:791–794, 2001.

[64] C.A. Sackett, D. Kielpinski, B.E. King, C. Langer, V. Meyer, C.J. Myatt, M. Rowe, Q.A. Turchette, W.M. Itano, D.J. Wineland, and C. Monroe. Entanglement and quantum computation with ions in thermal motion. *Nature*, 404:256–259, 2000.

[65] G. Savard, S. Becker, and G. Bollen. A new cooling technique for heavy-ions in a Penning trap. *Phys. Lett. A*, 158:247–252, 1991.

[66] F. Schmidt-Kaler, H. Haffner, M. Riebe, S. Gulde, G.P.T. Lancaster, T. Deuschle, C. Becher, C.F. Roos, J. Eschner, and R. Blatt. Realisation of the Cirac-Zoller controlled-NOT quantum gate. *Nature*, 422:408–411, 2003.

[67] P.W. Shor. Polynomial-time algorithms for prime factorisation and discrete logarithms on a quantum computer. *Proc. 35th Annual Symp. on Foundations of Computer Science*, 1994.

[68] P.W. Shor. Scheme for reducing decoherence in quantum computer memory. *Phys. Rev. A.*, 52:24932496, 1995.

[69] T. Sleator and H. Weinfurter. Realizable universal quantum logic gates. *Phy. Rev. Lett.*, 74:4087–4090, 1995.

[70] A. Sorensen and K. Molmer. Quantum computation with ions in thermal motion. *Phys. Rev. Lett.*, 82:1971–1974, 1999.

[71] A. Sorensen and K. Molmer. Entanglement and quantum computation with ions in thermal motion. *Phys. Rev. A*, 62:022311, 2000.

[72] A.M. Steane. Multiple-particle interference and quantum error correction. *P. Roy. Soc. Lond. A.*, 452:2551–2557, 1996.

[73] A.M. Steane. The ion trap quantum information processor. *Appl. Phys. B*, 64:623–642, 1997.

[74] J. Sudbery. *Studies of Laser Cooled Calcium Ions in the Penning and Combined Traps.* PhD thesis, Imperial College London, 2003.

[75] Q.A. Turchette, D. Kielpinski, B.E. King, D. Liebfried, D.M. Meekhof, C.J. Myatt, M.A. Rowe, C.A. Sackett, C.S. Wood, W.M. Itano, C. Monrow, and D.J. Wineland. Entanglement and quantum computation with ions in thermal motion. *Phys. Rev. A*, 61:063418, 2000.

[76] L.M.K. Vandersypen, M. Steffen, G. Bretya, C.S. Yannoni, M.H. Sherwood, and I.L. Chuang. Experimental realization of Shor's quantum factoring algorithm using nuclear magnetic resonance. *Nature*, 414:883–887, 2001.

[77] L.M.K. Vandersypen, C.S. Yannoni, M.H. Sherwood, and I.L. Chuang. Realization of logically labeled effective pure states for bulk quantum computation. *Phys. Rev. Lett.*, 83:3085–3088, 1999.

[78] D.C. Wilson. *Quantum Optics and Ion Dynamics in a Quadrupole Ion Trap.* PhD thesis, Imperial College, University of London, 1992.

[79] D.J. Wineland and H.G. Dehmelt. Proposed 10^{14} $\nu/\Delta\nu$ laser fluorescence spectroscopy on Tl^+ monoion oscillator II. *Bull. Am. Phys. Soc.*, 20:637, 1975.

[80] D.J. Wineland, R.E. Drullinger, and F.L. Walls. Radiation pressure cooling of bound resonant absorbers. *Phys. Rev. Lett.*, 40:1639–1642, 1978.

[81] D.J. Wineland and W.M. Itano. Laser cooling of atoms. *Phys. Rev. A*, 20:1521–1540, 1979.

[82] D.J. Wineland, C. Monroe, W.M. Itano, D. Liebfried, B.E. King, and D.M. Meekhof. Experimental issues in coherent quantum-state manupulation of trapped atomic ions. *J. Res. Natl. Inst. Stand. Tech.*, 103:259, 1998.

[83] B.C. Young, F.C. Cruz, W.M. Itano, and J.C. Bergquist. Visible lasers with subhertz linewidths. *Phys. Rev. Lett.*, 82:3799–3802, 1999.

[84] J. Zhang, Z. Lu, L. Shan, and Z. Deng. Experimental implementation of generalized Grover's algorithm of multiple marked states and its application. quant-ph/0208102.

[85] S.-B. Zheng and G.-C. Guo. Efficient scheme for two-atom entanglement and quantum information processing in cavity-QED. *Phys. Rev. Lett.*, 85:2392–2395, 2000.